Digital Compensation Schemes for Signal Distortion in OFDM Receivers

July 2009

Mamiko Inamori

DISSERTATION

Submitted to the School of Integrated Design Engineering, Keio University, in partial fulfillment of the requirements for the degree of Doctor of Philosophy

Abstract

Various wireless standards have been developed for realizing broadband anywhere / anytime access network. Orthogonal division frequency multiplexing (OFDM) is currently a dominant modulation scheme in broadband wireless systems. The receiver is required to satisfy the conditions such as high-performance, low power consumption, small size, and low cost. However, in the receiver for the broadband signal, more accuracy of analog components is necessary and it leads to larger cost and power consumption. To implement a low cost and low power consumption receiver, compensation of the signal distortion in a digital domain is required. The signal distortion compensation in the digital domain brings more scalability and flexibility. In this dissertation, digital signal compensation schemes for the signal distortion due to radio frequency (RF) components, timing jitter, and baseband filter in OFDM receivers are proposed and investigated.

Chapter 1 introduces the background of the OFDM receivers and the motivation of the research.

In Chapter 2, compensation schemes for signal distortion in a direct conversion receiver are investigated. The OFDM direct conversion receiver is superior to a superheterodyne receiver in cost, size, and power consumption. However, this receiver architecture suffers from DC offset, frequency offset, and IQ imbalance. In the proposed scheme, the key idea is to use a differential filter for the reduction of the DC offset. From the outputs of differential filter in the training sequence, the frequency offset is estimated with auto-correlation in the presence of DC offset. The proposed scheme shows better estimation accuracy of the frequency offset than the conventional scheme with a high pass filter. The IQ imbalance is calculated in time domain using a simple equation without the impulse response of a channel in the presence of the frequency offset and the DC offset. However, the accuracy of the IQ imbalance estimation with the proposed scheme in the time domain is deteriorated when the frequency offset is small. To overcome this problem, frequency domain IQ imbalance estimation scheme is also proposed, which uses the pilot subcarriers in the data period. Numerical results obtained through computer

simulation show that estimation accuracy and bit error rate (BER) performance can be improved even if the frequency offset is small. Thus, the combination of two low-complexity IQ imbalance estimation schemes is suitable for low-cost and low-power-consumption direct conversion receivers.

In Chapter 3, signal distortion caused by timing jitter is discussed. As one of new receiver architectures, a RF-sampling receiver has been proposed, which directly processes analog discrete samples. In this architecture, a phase locked loop (PLL) exhibits the phase noise and then causes the timing jitter. In wireless receivers, quadrature sampling is required in order to demodulate I-phase and Q-phase signals. Different from simple charge sampling, timing jitter causes crosstalk between these signals. In Chapter 3, the effect of the timing jitter on quadrature sampling in the RF-sampling receiver is analyzed.

In Chapter 4, compensation schemes for signal distortion in fractional sampling (FS) OFDM receivers are evaluated. The OFDM system with FS can achieve diversity with a single antenna. However, as the number of subcarriers and the oversampling ratio increase, the correlation among the noise components over different subcarriers deteriorates the BER performance. First, a correlated noise cancellation scheme in FS orthogonal frequency and code division multiplexing (OFCDM) system is investigated. To reduce the correlated noise, an alternative spreading code (ASC) is used in the FS OFCDM system. This spreading code has positive and negative components alternatively. Despreading with the ASC cancels most of the correlated noise components. However, this alternative spreading code reduces the number of available spreading codes. For applicability to OFDM systems, the effect of the correlation among the noise components in FS OFDM system is derived. A metric weighting scheme for the coded FS OFDM system is also proposed and investigated.

Chapter 5 summarizes the results of each chapter and concludes this dissertation.

Contents

List of Figures

List of Tables

List of Acronyms

1G first generation
2G second generation
3G third generation
3GPP third generation partnership project
3GPP2 third generation partnership project 2
3.9G 3.9 generation
4G fourth generation
64QAM quadrature amplitude modulation
A/D analog-to-digital
ADC analog-to-digital converter
AGC automatic gain control
AFC automatic frequency control
AWGN additive white Gaussian noise
BER bit error rate
BPF band pass filter
CDMA code division multiple access
CMOS complementary metal oxide semiconductor
DC direct current
DFT discrete Fourier transform
DS/SS direct sequence / spread-spectrum
FCC federal communications commission
FDMA frequency division multiple access
FIR finite impulse response
FS fractional sampling
GI guard interval
HPF high pass filter
HSDPA High Speed Downlink Packet Access
I in-phase
ICI intercarrier interference
IEEE institute of electrical and electronics engineers
IF intermediate frequency

IDFT inverse discrete Fourier transform
IMT-2000 International Mobile Telecommunications-2000
IR-UWB impulse-radio UWB
ISI intersymbol interference
ISM industrial, scientific and medical
ITU international telecommunication union
LNA low noise amplifier
LO local oscillator
LPF low pass filter
LTE long term evolution
LTSP long training sequence preamble
MB-OFDM multiband-OFDM
MBWA mobile broadband wireless access
MIMO multiple-input multiple-output
MRC maximal ratio combing
MSE mean square error
OFCDM orthogonal frequency and code division multiplexing
OFDM orthogonal frequency division multiplexing
OFDMA orthogonal frequency division multiplexing access
PLL phase locked loop
P/S parallel-to-serial
PSD power spectrum density
Q quadrature
QOCRC quadrature overlapped cubed raised cosine
QOSRC Quadrature overlapped squared raised cosine
QoS quality of service
QPSK quadrature phase-shift keying
RF radio frequency
RSSI receive signal strength indicator
SAW surface acoustic wave
SIMO single-input multiple-output
SINR signal-to-interference and noise ratio
SISO single-input single-output channel
SNR signal-to-noise ratio
S/P serial-to-parallel
STSP short training sequence preamble
TCXO temperature-compensated crystal oscillator
TDMA time division multiple access
USB universal serial bus
UWB ultra-wide band

VCO voltage-controlled oscillator
VGA variable gain amplifier
WCDMA Wideband-Code Division Multiple Access
WiMAX Worldwide Interoperability for Microwave Access
WLAN wireless local network
WMAN wireless metropolitan area network
WPAN wireless personal area network
WWAN wireless wide area network

List of Notations

a	roll-off factor of root cosine roll-off filter
A_I	amplitude of I-phase component
A_Q	amplitude of Q-phase component
$A_I[n]$	n-th sampled amplitude of I-phase component
$A_Q[n]$	n-th sampled amplitude of Q-phase component
$c(t)$	impulse response of the physical channel
C_{add}	numbers of complex additions
C_{mult}	numbers of complex multiplications
C_{div}	numbers of complex divisions
C_{ε}	numbers of calculations to estimate ε
$d_{SP}[n]$	n-th STSP output signal after differential filtering
$\hat{d}_{SP}[n]$	n-th STSP output with IQ imbalance after the differential filter
$D[k]$	output after the differential filter in the frequency domain
f_B	cutoff frequency of filter
f_c	RF carrier frequency
f_s	symbol rate
g	oversampling index
G	oversampling ratio
$h(t)$	impulse response of the composite channel
$h_g[n]$	sampled $h(t)$ at $(nT_s + gT_s/G)$
$H_{\mathrm{DF}}[k]$	channel response of the differential filter
$H[k]$	channel response of the k-th subcarrier
$H'[k]$	$H[k]$ after noise whitening
$H_g[k]$	frequency response of $h_g[n]$
$\mathbf{H}[k]$	$G \times 1$ matrix consists of the elements $H_g[k]$
$\mathbf{H}'[k]$	$\mathbf{H}[k]$ after noise whitening
k	subcarrier index
L	number of multipath
m	number of OFDM symbol
m_I	information signals of the I-phase component
m_Q	information signals of the Q-phase component
n	time index
N	number of DFT points

N_g	PSD of white spectrum shape
N_n	PSD of nonwhite spectrum shape
N_{sp}	number of samples in the STSP
$\mathbf{N_D}$	set of indices for the data subcarriers
$\mathbf{N_P}$	set of indices for the pilot subcarriers
$p(t)$	impulse response of the pulse shaping filter
$p_2(t)$	composite response of the filters
P	sum of the IDFT length and the length of GI
$P[k]$	k-th pilot subcarrier
$\hat{P}_m[k]$	k-th pilot subcarrier with IQ imbalance on m-th OFDM symbol
q_i	i-th spreading code
$r[n]$	n-th sample of the received OFDM symbol in the time domain
$r(t)$	the received OFDM signal in the time domain
$\hat{r}[n]$	$r[n]$ with IQ imbalance
$\hat{r}^{'}[n]$	n-th received signal after frequency offset compensation in the time domain
$r_{LP}[n]$	n-th received signal in LTSP
$r_{SP}[n]$	n-th received signal in STSP
$\hat{r}_{SP}[n]$	n-th received signal in STSP with IQ imbalance
$r_I[n]$	I-phase component of $r[n]$
$r_Q[n]$	Q-phase component of $r[n]$
$\hat{r}_I[n]$	$r_I[n]$ with IQ imbalance
$\hat{r}_Q[n]$	$r_Q[n]$ with IQ imbalance
$R[k]$	received signal on k-th subcarrier
$\hat{R}[k]$	received signal with IQ imbalance on k-th subcarrier
$\hat{R}'[k]$	received signal with frequency offset on k-th subcarrier
$\tilde{R}[k]$	received symbol after IQ imbalance compensation on k-th subcarrier
$\mathbf{R}_n[k_1, k_2]$	$G \times G$ matrix (k_1, k_2)-th subblock of the $NG \times NG$ matrix, $\mathbf{R}_{ww}\mathbf{R}_w^{\frac{1}{2}}$
$[\mathbf{R}_n[k_1, k_2]]_{g_1,g_2}$	(g_1, g_2)-th element of $\mathbf{R}_n[k_1, k_2]$
$\mathbf{R}_w[k]$	covariance matrix of noise on k-th subcarrier
s_{pI}	I-phase local signal
s_{pQ}	Q-phase local signal
$s[n]$	n-th sample of the transmitted OFDM symbol in the time domain
$s[k]$	transmitted symbol on the k-th subcarrier
$s'[k]$	estimate of $\hat{s}[k]$
S_f	spreading factor in the frequency domain
$t_1 \cdots t_{10}$	STSP period
T_1, T_2	LTSP period
T_{DFT}	IDFT/DFT period
T_s	1/symbol rate
$u[l]$	transmitted signal with the GI
$v(t)$	narrow band AWGN
$v[n]$	n-th AWGN sample
$v_I[n]$	n-th AWGN sample of I-phase component

$v_Q[n]$	n-th AWGN sample of Q-phase component
$v_g[n]$	sampled $v(t)$ at $(nT_s + gT_s/G)$
$w_g[k]$	frequency response of $v_g[n]$
$\mathbf{w}[k]$	$G \times 1$ matrix consists of the elements $w_g[k]$
$\mathbf{w'}[k]$	$\mathbf{w}[k]$ after noise whitening
$y(t)$	received signal
$y_g[n]$	sampled $y(t)$ at $(nT_s + gT_s/G)$
$z[k]$	k-th demodulated signal
$z_g[k]$	frequency response of $y_g[n]$
$\mathbf{z}[k]$	$G \times 1$ matrix consists of the elements $z_g[k]$
$\mathbf{z'}[k]$	$\mathbf{z}[k]$ after noise whitening
α	normalized frequency offset
$\hat{\alpha}$	estimated frequency offset
$\hat{\alpha}'$	estimated frequency offset in STSP
$\hat{\alpha}''$	estimated frequency offset in LTSP
$\hat{\alpha}_{co}$	estimated frequency offset in STSP and LTSP with conventional scheme
$\alpha_{co}^{'}$	estimated frequency offset in STSP with conventional scheme
$\alpha_{co}^{''}$	estimated frequency offset in LTSP with conventional scheme
$\hat{\alpha}_{pr}$	estimated frequency offset in STSP and LTSP with proposed scheme
$\alpha_{pr}^{'}$	estimated frequency offset in STSP with proposed scheme
$\alpha_{pr}^{''}$	estimated frequency offset in LTSP with proposed scheme
β	gain mismatch of IQ imbalance
γ	exponential expression of α
γ_0	impulse response of physical channel at the sampling point of $G = 1$
γ_1	impulse response of physical channel at the sampling point of $G = 2$
$\gamma_{\mathbf{alt}}$	correlated noise after despreading with the alternative spreading code
$\gamma_{\mathbf{non}}$	correlated noise after despreading with the non-alternative spreading code
ε	solution of simultaneous equations for IQ imbalance estimation
θ	phase mismatch of IQ imbalance
$\lambda_g[k_1]$	g-th eigenvalue of $\mathbf{R}_{\tilde{w}}^{\frac{1}{2}}[k_1]$
ξ	scaling effect of the pulse shaping filter at the offset sampling instants of $\pm T_s/2$
$\rho_1[n] \cdots \rho_5[n]$	elements of the auto-correlation value
$\rho'[n] \cdots \rho''''[n]$	elements of the variance of $\rho_5[n]$
$\sigma^2{}_v$	variance of $v[n]$
$\tau[n]$	sampling jitter on the I-phase or Q-phase signals
ϕ	effect of IQ imbalance
ψ	effect of IQ imbalance on the symmetric subcarrier
$\boldsymbol{\omega}$	the white noise in the vector form
$\omega_g[k]$	white noise of the g-th sample component on the k-th subcarrier
ω_c	angular frequency of the RF carrier signal
$\delta[n]$	n-th residual DC offset
Δ	integration period
$\Delta\delta[n, n-1]$	the difference of the n-th and $[n-1]$-th residual DC offset samples

E[ ]	expectation
$\mathbf{A}^H$	Hermitian transpose of $\mathbf{A}$
$O(A, B)$	products of A and B
$\approx$	approximately equal to
$\star$	convolution operator
$*$	complex conjugate
$\|\|\mathbf{A}\|\|_F$	Frobenius norm of $\mathbf{A}$

Chapter 1

General Introduction

In this chapter, an orthogonal frequency division multiplexing (OFDM) modulation scheme is described, which is standardized in many wireless communication systems to achieve high data rate transmission. Several types of a receiver architecture are also introduced. At the receiving end, each receiver architecture suffers from signal distortion due to radio frequency (RF) components, timing jitter and baseband filters. The causes of the distortion and the effects on the received signal are explained. This introduction also presents the overall relationship among chapters in this dissertation.

1.1 Broadband Wireless System

1.1.1 Broadband Cellular System

From 1990's, the demands of wireless communications have been tremendously rising for voice and data communications. With the expansion of the wireless voice subscribers, the Internet users, and the portable computing devices, various wireless standards have been developed for realizing an anywhere/anytime access network as shown in Fig. 1.1 [1.1][1.2]. Transmission rates in the mobile wireless access network are rapidly growing recently. At the beginning of the mobile wireless access network, the first generation (1G) system was developed in the 1980s until the second generation (2G) was started. The 1G system implemented analog modulation using around 900 MHz frequency range with frequency division multiple access (FDMA). It was designed to transmit voice and low rate data. Following the 1G, the 2G was launched in 1993. The 2G was a digital network system, which introduced data services for mobiles using the time division multiple access (TDMA). It supported data rates of up to 20 kbps [1.3][1.4]. The number

of mobile subscribers increased drastically with the introduction of 2G.

For the further expansion of the requisition of service quality, the high speed communication links have been developed. The third generation (3G) is designed to provide higher data rate. The international telecommunication union (ITU) named the international standard for the 3G mobile network as the International Mobile Telecommunications-2000 (IMT-2000). The IMT-2000 standard was developed with the intention of unifying the various wireless cellular systems and providing a global wireless standard. Two projects under IMT-2000 were established for defining the specification. The third generation partnership project (3GPP) specifies standards for the 3G technology called Wideband-Code Division Multiple Access (W-CDMA). In 2001 and 2002, NTT DoCoMo, Inc. and SoftBank Corporation launched respectively the 3G service using W-CDMA. NTT DoCoMo, Inc. provides High Speed Downlink Packet Access (HSDPA), which extends and improves the performance of existing W-CDMA protocols. On the other hand, the third generation partnership project 2 (3GPP2) was working on CDMA2000. In Japan, KDDI Corporation has started the 3G service based on CDMA2000 in 2002. Both W-CDMA and CDMA2000 use spread-spectrum direct-sequence (DS/SS) techniques and can provide the transmission rates of up to 2Mbps for stationary users in macro-cellular environments with occupying the bandwidth of about 5MHz.

The expected demands for broadband Internet access are motivating the investigation of a next generation wireless system. Following IMT-2000, the standardization of the 3.9th generation (3.9G) and the forth generation (4G) systems has been progressing. The 3GPP has introduced long term evolution (LTE) as the 3.9G. LTE also supports seamless connection to existing networks such as GSM, CDMA, and W-CDMA, which means LTE enables a smooth transition from the 3G to the 4G. LTE targets the requirements of the next generation wireless networks including downlink peak rates of at least 100 Mbps. To improve the transmission rate, bandwidth and spectrum efficiency are essential factors. The system of LTE employs OFDM or OFDM-based modulation scheme with the bandwidth of about 20MHz to achieve such high data transmission. Following LTE, IMT-Advanced will be capable of providing communication links of between 100 Mbps and 1 Gbps both indoors and outdoors with high quality and high security. The 4G system will be a complete replacement for the current networks. Although the specification of the IMT-Advanced standard has been under discussion, the OFDM-based modulation scheme is recognized as a promising candidate to satisfy those requirements. The specification of digital cellular networks is shown in Table

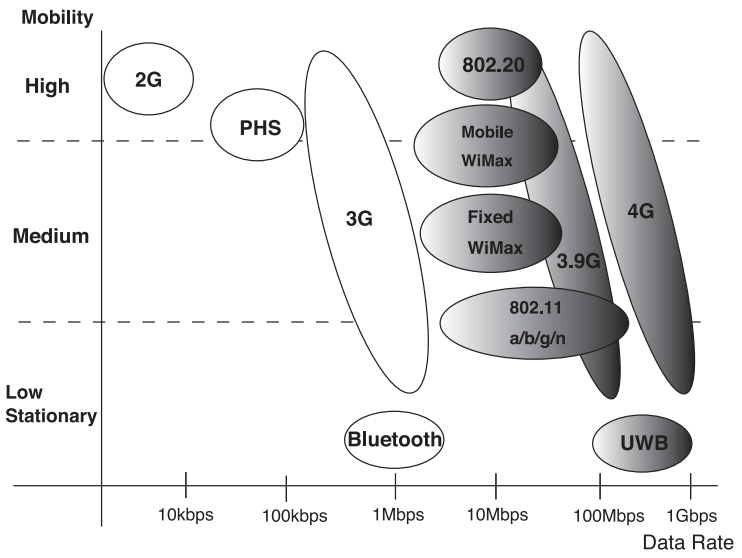

Figure 1.1: Wireless standard.

1.1.

1.1.2 Broadband Wireless Access Network

Wireless Internet access has been spreading all over the world with the emergence of portable laptop computers and the Internet technology. Recently, public areas such as coffee shops or shopping malls have begun to offer wireless access to their customers. With good quality of service (QoS), many end users desire the same services and functions as those with the wired networks. It is shown in Fig. 1.1, broadband wireless access systems have been improved to achieve high data transmission irrespective of users' mobility. The institute of electrical and electronics engineers (IEEE) historically has standardized the local broadband wireless access, which is clearly seen from the development of wireless personal area network (WPAN), wireless local network (WLAN), wireless metropolitan area network (WMAN), and wireless wide area network (WWAN) as shown in Fig. 1.2. The IEEE 802.15 WPAN technology has been developed for short-range wireless communications, which enables the exchange of data between close devices. The IEEE 802.11 WLAN technology, also known as WiFi, has been widely deployed in the range of 100m. The IEEE 802.16 WMAN technology, is commercialized as 'WiMAX' (Worldwide Interoperability for Microwave Access), supports broadband wireless access system for large number of users in a large area. However,

Table 1.1: Cellular systems.

Standard	2G	3G	3.9G	4G
Name	GSM	IMT-2000	LTE	IMT-Advanced
Name in Japan	PDC	W-CDMA CDMA2000	Super 3G Ultra 3G	
Frequency band in Japan	800MHz 1.5GHz	2GHz	1.5GHz	3.4-3.6GH
Frequency bandwidth	25kHz	5MHz	20MHz	100MHz
Data rate	20kbps	2Mbps	100Mbps	1Gbps
Modulation	TDMA	WCDMA	OFDMA	OFDM,OFCDM [Under discussion]

WiMAX is limited with the rage of coverage area up to 50km. IEEE 802.20 may revolutionize the concept of wireless access services and replace the existing cellular network with the same coverage area as the cellular system. The transmission rate of 20Mbps is possible. It will provide the seamless integration between indoor and outdoor environment, and lead to ubiquitous access network for users.

1.1.2.1 WPAN

The WPAN can be used in the small area to connect devices with low-data-rate, low-power-consumption and low-cost applications with network technologies such as Bluetooth and ZigBee. IEEE 802.15.3a attempts to provide a higher speed for WPAN with ultra-wide band (UWB). In 2002, the federal communications commission (FCC) in the U.S. authorized the commercialization of UWB for communication applications. The UWB is a radio technology that can be used as short-range high-data rate communications by occupying a large portion of radio spectrum. The UWB achieves the transmission rate of up to 480Mbps, which is higher than Bluetooth and WLAN. The modulation technique for UWB in 802.15.3a was discussed between the two candidates, the multiband-OFDM (MB-OFDM) or impulse-radio UWB (IR-UWB). However, IEEE 802.15.3a task group has dissolved in 2006 because it could not select one of them. Currently, ECMA-368, which is a standard under Ecma International, has adopted UWB in the physical layer [1.5]. ECMA-368 specifies OFDM as a modulation scheme. It is the standard for wireless universal serial bus (USB).

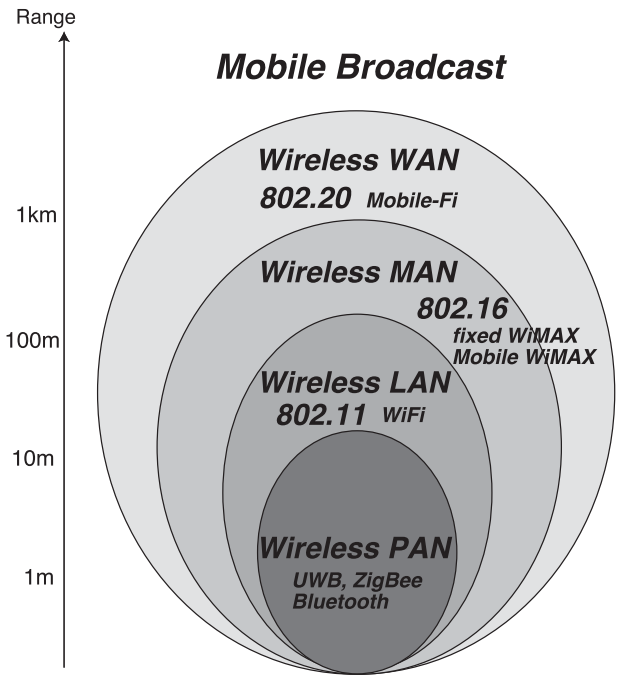

Figure 1.2: IEEE 802 standard.

1.1.2.2 WLAN

IEEE has developed the international WLAN standards in 802.11. This project launched in 1997 and the WLANs has been studied as alternative networks to fixed wired infrastructures. For example, as the replacement of Ethernet, the IEEE 802.11b is widely used.Through the use of DS/SS, IEEE 802.11b provides the data rate of up to 11 Mbps with using the 2.4 GHz industrial, scientific, and medical (ISM) band [1.6]. However, IEEE 802.11b suffers from interference due to the other devices such as microwave ovens, Bluetooth devices, and cordless telephones which share the same ISM band. IEEE has developed 802.11a as another extension to the WLAN. Its physical layer employs OFDM modulation in the 5 GHz band. The overall effective range of 802.11a is smaller than that of 802.11b because of the higher carrier frequency, but it achieves the transmission data rate of up to 54 Mbps [1.7]. In 2003, IEEE 802.11g standard was released, which operates in the same 2.4 GHz band and enables the compatibility with 802.11b. The transmission rate achieves 54MHz with the same OFDM based modulation scheme as 802.11a [1.8]. The IEEE 802.11g also supports DS/SS. In 2009, new WLAN standard is going to be released as IEEE 802.11n. IEEE 802.11n provides the

data rate of more than 100 Mbps with a multiple-input multiple-output (MIMO) OFDM scheme [1.9]. The MIMO can increase the transmission rate with employing multiple antenna elements for both the transmitter and the receiver. Based on the draft of the IEEE 802.11n standard draft, the same frequency bands as the other 802.11 standards, 2.4GHz and 5GHz, are specified as the operating frequency band. Currently, 802.11n products based on the draft has been sold on the market.

1.1.2.3 WMAN

In 1998, IEEE 802.16 started to define the specification for WWAN, which had intention to provide high date rate fixed access [1.10]. In the IEEE 802.16 group, the IEEE 802.16a has been approved with the frequency band from 2 to 11 GHz and was renamed as IEEE 802.16-2004 in 2004. This is also called fixed WiMAX and provides the communication links of up to 75Mbps. The 802.16e standard enhances the original IEEE 802.16 with mobility, which promises to the speed of 120km/h. The frequency band is under 6GHz and the transmission rate is up to 75Mbps. The mobile WiMAX will enable longer range broadband service. The 802.16 standard defines three different physical layer specifications, which are single carrier modulation, OFDM, and orthogonal frequency division multiplexing access (OFDMA). In Japan, UQ Communications Inc. has started trial services of WiMAX in February 2009 and will start the commercial services in July 2009.

1.1.2.4 WWAN

In 2006, a draft of IEEE 802.20 specification for WWAN was approved. The aim of the IEEE 802.20, so called Mobile-Fi, is to define the specifications for employing the efficient, always-on, and worldwide mobile broadband wireless access, which has higher data rate than current mobile network systems. The IEEE 802.20 mobile broadband wireless access (MBWA) will increase the coverage and mobility compared to WLAN and WiMAX. The air interface will operate in the frequency band below 3.5GHz and the data rate larger than 1Mbps. The vehicular speeds of up to 250km/h is expected [1.11]. The IEEE 802.20 also fills the gap between the cellular networks and the other wireless networks currently in use, such as WLAN or WMAN. As the system architecture, OFDM is employed in the physical layer.

1.2 OFDM Receiver

OFDM has become the leading modulation scheme of various broadband wireless access standards, which has the historical background. In the early 1960's, OFDM

Table 1.2: IEEE 802.11 protocols.

	WPAN	WLAN		WMAN		WWAN
Protocol	802.15.3a	802.11a/g	802.11n	802.16-2004	802.16e	802.20
Release year	2006 [withdrawn]	1999(a) 2003(g)	2009 [speculated]	2004	2005	2006
Frequency band	3.1GHz -10.6GHz	5MHz(a) 2.4MHz(g)	2.4MHz 5MHz	-11GHz	-6GHz	-3.5GHz
Data rate	480Mbps	54Mbps	600Mbps	75Mpbs	75Mbps	260MHz
Modulation	IR-UWB MB-OFDM	OFDM CCK	OFDM	SC, OFDM OFDMA	OFDM OFDMA	OFDM

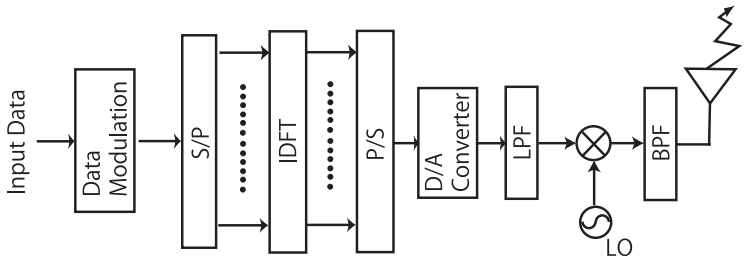

Figure 1.3: OFDM transmitter architecture.

was proposed and analyzed theoretically [1.12]. The complexity of OFDM was greatly reduced by using discrete Fourie transform (DFT) [1.13]. OFDM has been developed in the middle of 1980's [1.14]. OFDM system achieves the broadband communication by multiplexing a large number of narrow band data streams over orthogonal subcarriers. The advantage of OFDM is robustness against multipath fading. OFDM can largely eliminate the effects of intersymbol interference (ISI) for high-speed transmission in very dispersive multipath environments. The transmitter and receiver architectures of OFDM system are shown in Figs. 3.28 and 1.4 [1.15]. The available frequency spectrum is divided into several sub-channels, and each low-rate bit stream is transmitted over one sub-channel by modulating a sub-carrier using a standard modulation scheme. The sub-carrier frequencies are chosen so that the modulated data streams are orthogonal to one another, meaning that cross-talk between the sub-channels is eliminated. The orthogonality allows for efficient modulator and demodulator implementation using the DFT algorithm.

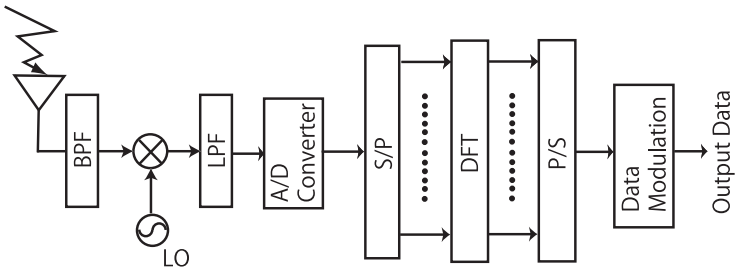

Figure 1.4: OFDM receiver architecture.

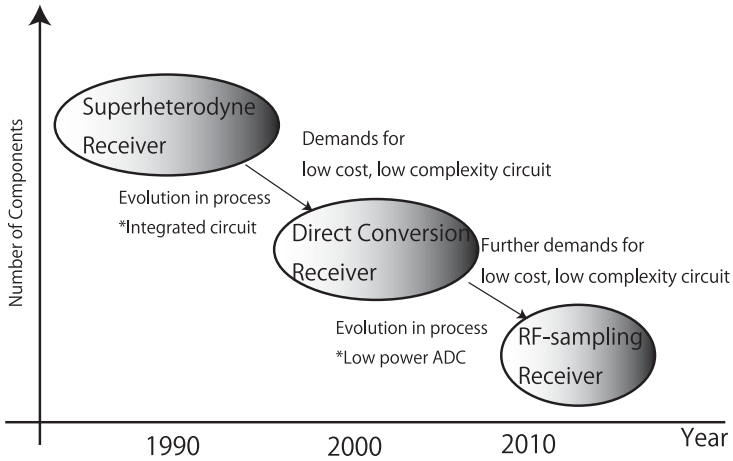

Figure 1.5: Evolution of receiver architectures.

1.3 OFDM Receiver Architecture

At the receiving end, the complexity, cost, power consumption, and number of external components are very important factors. Because of the development of complementary metal-oxide semiconductor (CMOS) processes, the architecture of the receiver has drastically changed [1.16]. The growing use of the integrated circuits in receivers and the evolution of analog-digital conversion (ADC) have resulted in significant improvement in the reliability and performance as shown in Fig. 1.5 [1.17]. As the evolution of the receiver architecture, superheterodyne receiver, direct conversion receiver, and RF-sampling receiver are introduced.

1.3.1 Superheterodyne Receiver

The key requirements for a receiver is that its front-end structure must accurately translate the desired signal to a baseband. To achieve this requirement, super-

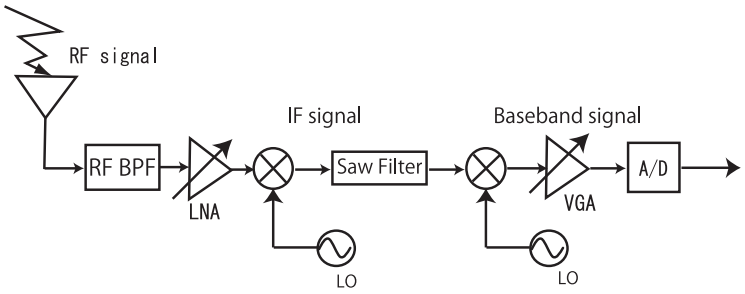

Figure 1.6: Superheterodyne receiver architecture.

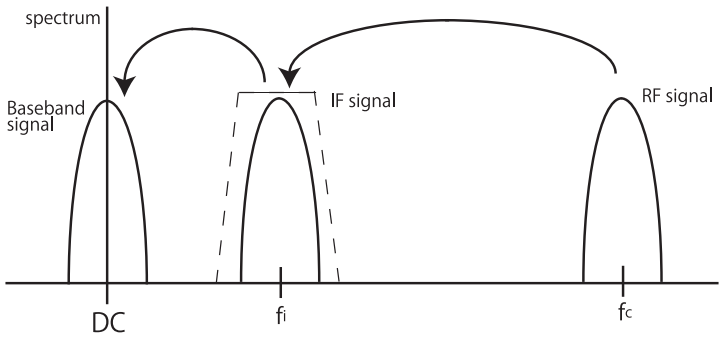

Figure 1.7: Downconversion in superheterodyne receiver.

heterodyne receiver architecture as shown in Fig. 1.6 was developed [1.18]. In this architecture, the received RF signal is down-converted to an intermediate frequency (IF) by being mixed with the output of a local oscillator (LO) as shown in Fig. 1.7. The resulting IF signal is then shifted to the baseband and it is quantized and demodulated. However, this architecture requires highly selective and expensive analog IF filters to remove an image signal. These filters are usually realized with a surface acoustic wave (SAW) filter, which needs to be placed in an off-chip circuit. The superheterodyne architecture then requires the additional cost and size of the receiver.

1.3.2 Direct Conversion Receiver

The direct conversion receiver structure is shown in Fig. 1.8. The received RF signal is filtered and passed through the low noise amplifier (LNA). After bandbass filtering, the signal is divided and put into the quadrature mixer. The LO signal and the $\pi/2$ phase shifted LO are also input to the mixer, which have RF carrier frequency. Thus, the received RF signal is translated to baseband as shown in Fig.

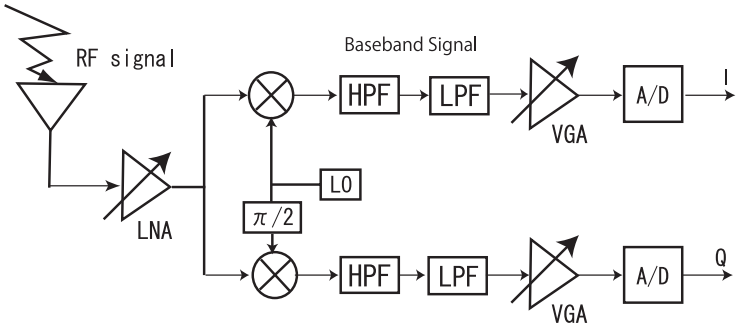

Figure 1.8: Direct conversion receiver architecture.

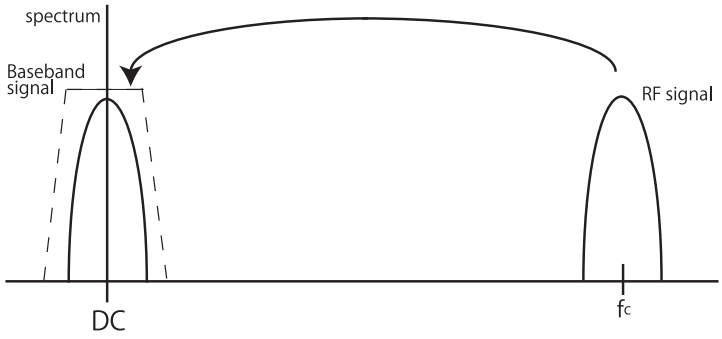

Figure 1.9: Downconversion in direct conversion receiver.

1.9. The advantage of this architecture is low complexity because it eliminates all the IF analog components. Therefore, the direct conversion architecture is suitable for mobile terminals since it avoids costly IF filters and allows easier integration on a chip than the superheterodyne structure. However, direct conversion receivers may suffer from the problem such as direct current (DC) offset and frequency offset. An example of these distortions with a OFDM signal is shown in Fig. 1.10. The main sources of the DC offset is the LO. The LO signal can be mixed with itself down to zero IF, resulting the generation of the DC offset. This is known as self-mixing, which is due to finite isolation between the LO and the RF ports of the LNA or the mixer. Moreover, the DC offset is attributed to the mismatch between the mixer components [1.19][1.20]. The frequency offset is caused by oscillators' mismatch of between the transmitter and receiver [1.21]. The frequency offset may deteriorate the orthogonality between the subcarriers. As well as the frequency offset and the DC offset, IQ imbalance cannot be neglected in this architecture [1.22]. This IQ imbalance is mainly attributed to the mismatched components in

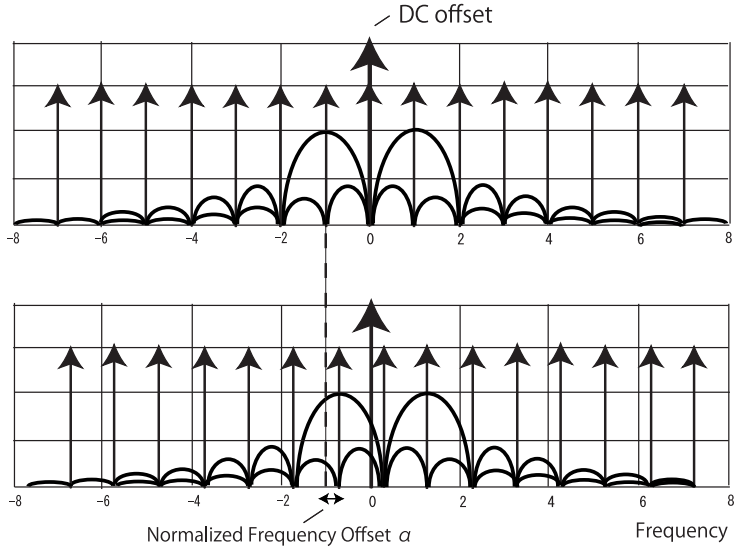

Figure 1.10: DC offset and frequency offset.

the in-phase (I) and the quadrature (Q) paths. Specifically, phase mismatch occurs when the phase difference between the local oscillator's signals for I and Q channels it not exactly 90 degrees. Gain imbalance refers to gain mismatch in the path of the I and Q signals [1.23]. The transmitted signal is shifted by the phase mismatch β and the gain mismatch θ due to the effect of IQ imbalance. For a quadrature phase-shift keying (QPSK) signal, the distortion due to the IQ imbalance and the DC offset is illustrated in Fig. 1.11.

1.3.3 RF-sampling Receiver

In the receiver architecture, RF front-end and ADCs are the key components. If it is possible to convert an RF signal directly to the digital samples, the analog components of the receiver can be simplified. However, as there is no ADCs that can be operated at RF, existing receivers can not convert the received signal from the analog domain to the digital domain directly [1.24]. One of new receiver architectures is RF-sampling, which directly processes analog discrete samples [1.25]. In the RF-sampling architecture, the received signal is sampled at a RF. Channel selection and demodulation are carried out in the digital domain. This architecture achieves reduction of off-chip components and enables the realization of one-chip receiver. The simplified receiver architecture is shown in Fig. 1.12. In the RF-sampling receiver architecture, the desired signal is extracted from the received RF

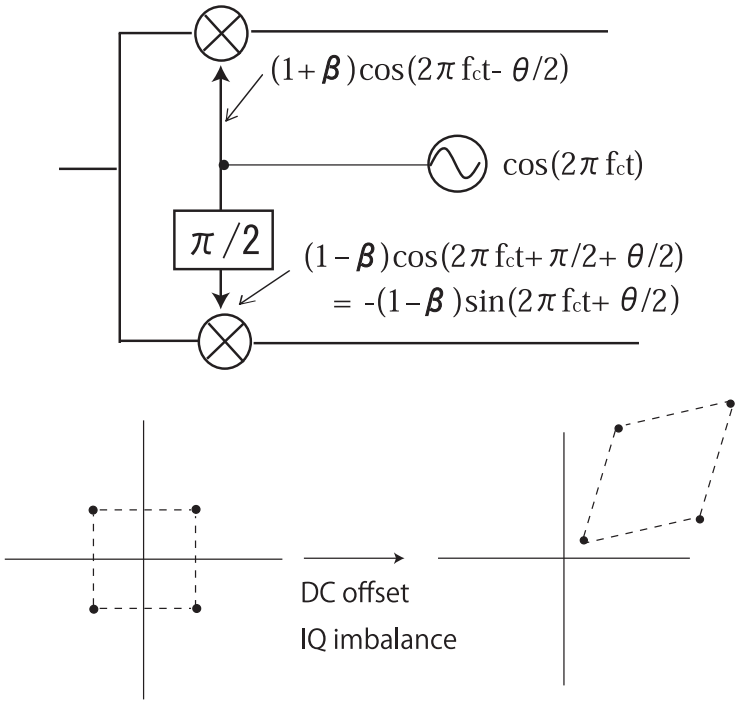

Figure 1.11: IQ imbalance model.

signal through the band pass filter (BPF). It is then amplified and sampled at RF. The sampled analog signal has baseband components as shown in Fig. 1.13. It is then filtered by the low pass filter (LPF) and demodulated. The signal is driven by the clock signal output from the comparator. This clock signal is created by the cosine wave in the RF from the phase locked loop (PLL). This architecture requires the accurate clock signal to perform actual sampling operation. However, the PLLs exhibit phase noise and then causes the timing jitter. The actual sampling point will be different from the ideal one as shown in Fig. 1.14. In the RF-sampling receiver, the timing jitter may cause the signal distortion and the effect decreases the signal-to-noise ratio (SNR).

1.3.4 Fractional Sampling

The performance improvement and realtime response are also important issues as the requirements of a receiver architecture. In wireless communication, the signal passes through many paths because of the reflection on objects such as mountains and buildings. Thus, the multipath causes distortion when the received signal reaches the received antenna, and deteriorates the performance of the system. To

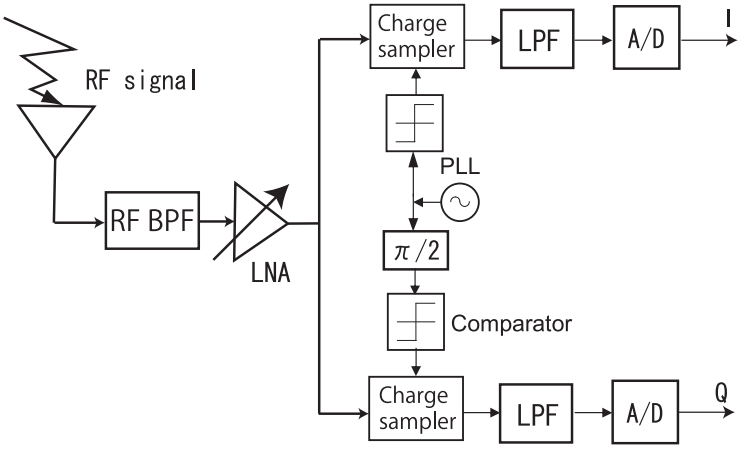

Figure 1.12: RF sampling receiver architecture.

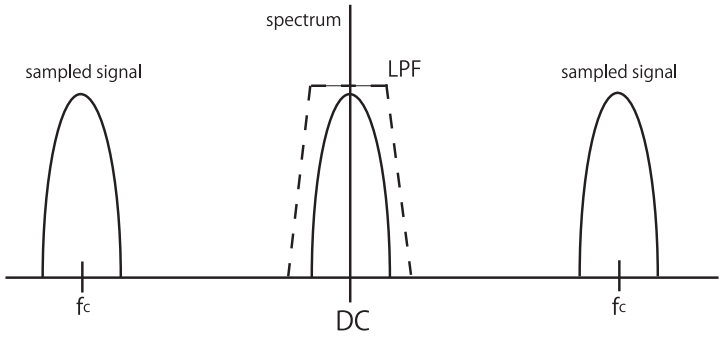

Figure 1.13: Downconversion in RF sampling receiver.

overcome this problem, various diversity techniques have been investigated [1.26]-[1.28].The spatial diversity is an effective way to improve the error performance of wireless systems. Simplified transmitter diversity can be achieved by transmitting the same OFDM symbols from multiple antennas with a delayed time, but this scheme is not suitable for achieving the realtime response. As a diversity scheme at the receiver side, spatial diversity, has been developed. The spatial diversity uses the multiple antennas at the receiver side. However, it is very difficult to put multiple antennas inside the small devises to receive the uncorrelated signal. Thus, the diversity scheme which obtains the diversity gain only with one antenna has been investigated. This is called fractional sampling (FS) [1.29]. By employing oversampling in the time domain and linear signal processing in the frequency domain, the FS OFDM system can be equivalently represented as the MIMO

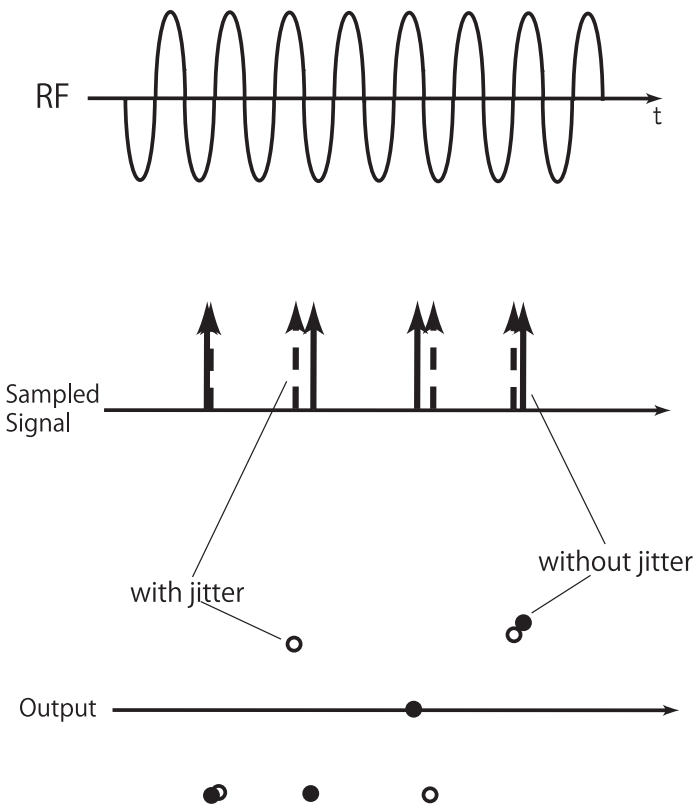

Figure 1.14: Influence of timing jitter.

system.

The block diagram of an OFDM receiver with FS is shown in Fig. 1.16. Though the front-end is the same as the direct conversion receiver architecture, the signal processing after analog-to-digital (A/D) conversion has the key technology in FS OFDM system. In FS, the received signal is sampled at a rate of G/T_s, which is faster than the Nyquist rate. (G represents oversampling ratio and $1/T_s$ is the baud rate)

An example of the impulse response of the channel is illustrated in Fig. 1.17. In this figure, G is set to 2 and γ_0 and γ_1 are the impulse responses of the physical channel. After filtering, the response of the channel is expressed with the dotted line. These responses are combined and expressed in the black line and it is then fractionally sampled. When the correlation between the sampling point $G = 1$ and the sampling point $G = 2$ becomes low, path diversity can be achieved.

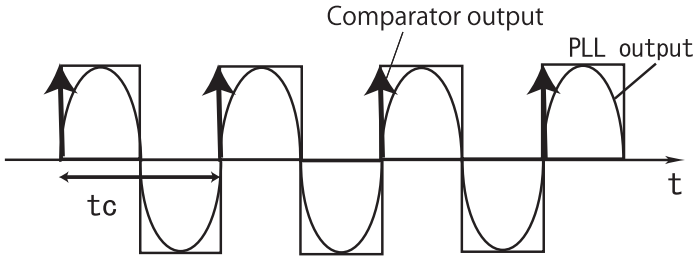

Figure 1.15: Influence of timing jitter.

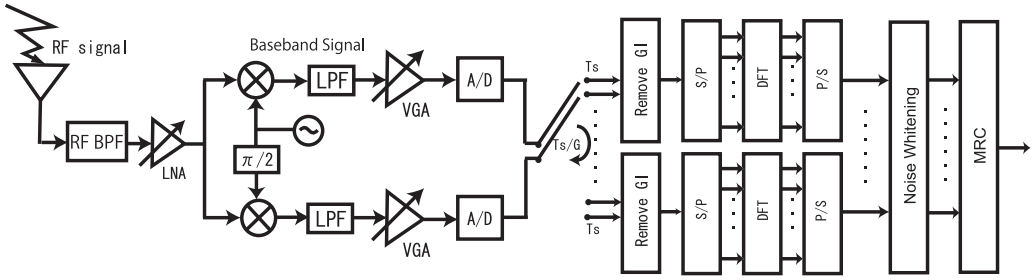

Figure 1.16: Fractional sampling receiver.

1.4 Signal Distortion in OFDM Receivers

1.4.1 Distortion due to RF Components

Both cost and complexity are very important factors for receivers in future wireless communications. The direct conversion receiver translates the desired signal directly to zero frequency. This architecture eliminates all IF components and allows low-cost and low-power realization. However, the direct conversion receiver for OFDM systems is sensitive to non-idealities in the RF front-end, which are not serious issues in superheterodyne receivers. As explained in Section 1.3.2, OFDM direct conversion receiver suffers from signal distortions due to RF components such as DC offset, frequency offset, and IQ imbalance [1.19][1.21][1.23]. The effect of degradation due to those problems is analyzed as follows.

Assuming that the n^{th} sample of the OFDM preamble in the time domain is $s[n]$, a received signal only with frequency offset, $r[n]$, is expressed as

$$r[n] = s[n] \exp(j\frac{2\pi\alpha}{N}n) + v[n], \tag{1.1}$$

where α is the frequency offset normalized by subcarrier separation, N is the number of samples for DFT, and $v[n]$ is the n-th additive white gaussian noise

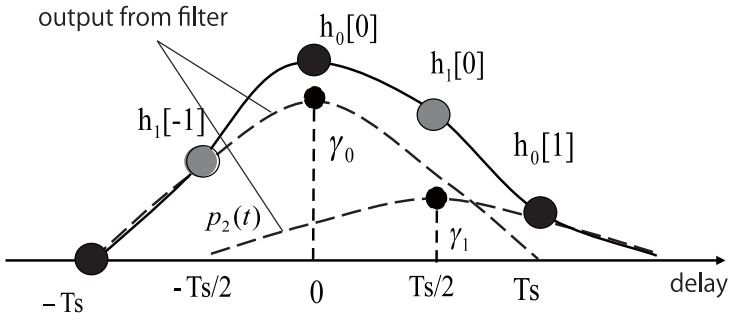

Figure 1.17: Fractional sampling in delay domain.

(AWGN) sample with zero mean and variance ${\sigma^2}_v$. When the IQ imbalance has occurred, due to the symmetry of the upper and lower paths, the I-phase local signal, s_{pI}, and the Q-phase local signal, s_{pQ}, are assumed to be as follows:

I component : $s_{pI}(t) = (1+\beta)\cos(2\pi f_c t - \theta/2)$,

Q component : $s_{pQ}(t) = -(1-\beta)\sin(2\pi f_c t + \theta/2)$,

where f_c is the carrier frequency. These local signals are multiplied by the received signal. By applying the LPF, the baseband signals, $\hat{r}_I[n]$ and $\hat{r}_Q[n]$, with IQ imbalance are obtained. The n^{th} digitized signal with a sampling interval of T_s is given by

$$\hat{r}[n] \;=\; \hat{r}_I[n] + j\hat{r}_Q[n], \tag{1.2}$$

where

$$\hat{r}_I[n] \;=\; (1+\beta)\{r_I[n]\cos(\frac{\theta}{2}) - r_Q[n]\sin(\frac{\theta}{2})\}, \tag{1.3}$$

$$\hat{r}_Q[n] \;=\; (1-\beta)\{r_Q[n]\cos(\frac{\theta}{2}) - r_I[n]\sin(\frac{\theta}{2})\}, \tag{1.4}$$

where $r_I[n]$ and $r_Q[n]$ are the I-phase component and the Q-phase component of $r[n]$, respectively. Hence, the complex baseband signal $\hat{r}[n]$ is

$$\begin{aligned}
\hat{r}[n] &= \hat{r}_I[n] + j\hat{r}_Q[n] \\
&= \{\cos(\frac{\theta}{2}) + j\beta\sin(\frac{\theta}{2})\}\{r_I[n] + jr_Q[n]\} \\
&\quad + \{\beta\cos(\frac{\theta}{2}) - j\sin(\frac{\theta}{2})\}\{r_I[n] - jr_Q[n]\} \\
&= \{\cos(\frac{\theta}{2}) + j\beta\sin(\frac{\theta}{2})\}r[n] + \{\beta\cos(\frac{\theta}{2}) - j\sin(\frac{\theta}{2})\}r^*[n]
\end{aligned} \tag{1.5}$$

where * denotes complex conjugate. From Eq. (1.5), the received signal with the IQ imbalance is given as

$$\hat{r}[n] = \phi r[n] + \psi^* r^*[n] + \delta[n], \tag{1.6}$$

where

$$\phi = \cos(\frac{\theta}{2}) + j\beta \sin(\frac{\theta}{2}), \tag{1.7}$$

$$\psi = \beta \cos(\frac{\theta}{2}) + j \sin(\frac{\theta}{2}), \tag{1.8}$$

and $\delta[n]$ is the DC offset that occurs at the mixer.

The output of the DFT in the frequency domain, $\hat{R}'[k]$, is then given as

$$\begin{aligned}
& \hat{R}'[k] \\
= & \sum_{n=0}^{N-1} \hat{r}'[n] \exp(-j\frac{2\pi k}{N} n) \\
= & \frac{\phi}{N}\Big(\sum_{n=0}^{N-1} R[k] \exp(j\frac{2\pi\alpha}{N} n) + \sum_{n=0}^{N-1} \sum_{\substack{k'=-\frac{N}{2} \\ k' \neq k}}^{\frac{N}{2}-1} R^*[k'] \exp(j\frac{2\pi(k'-k)}{N} n) \exp(j\frac{2\pi\alpha}{N} n)\Big) \\
+ & \frac{\psi^*}{N}\Big(\sum_{n=0}^{N-1} R^*[-k] \exp(-j\frac{2\pi\alpha}{N} n) \\
+ & \sum_{n=0}^{N-1} \sum_{\substack{k'=-\frac{N}{2} \\ k' \neq -k}}^{\frac{N}{2}-1} R^*[k'] \exp(-j\frac{2\pi(k'+k)}{N} n) \exp(-j\frac{2\pi\alpha}{N} n)\Big),
\end{aligned} \tag{1.9}$$

where

$$R[k] = \begin{cases} S[k] & k \neq 0 \\ \delta & k = 0 \end{cases} \tag{1.10}$$

From Eq. (1.9), it is shown that all the subcarriers cause intercarrier interference (ICI) to the k-th subcarrier due to the frequency offset is the second term of the right side of the equation. The IQ imbalance results in the additional ICI given in the third and forth terms. Those ICI includes the DC offset as given in Eq. (1.10).

1.4.2 Distortion due to PLL

In contrast to the direct conversion receiver, the RF-sampling receiver greatly simplifies the RF front-end with digital RF processing. However, the RF-sampling

receiver suffers from the timing jitter generated from phase noise in PLL. The influence of the phase noise of the PLL on the clock signal is described in this section. The output signal from the PLL is given as

$$s_p(t) = \sin(\omega_c t) + v_p(t), \tag{1.11}$$

where $v_p(t)$ is the PLL phase noise and ω_c is the angular frequency of the RF signal. This signal is input into the comparator and the clock signal is created as shown in Fig.1.15. Thus, the phase noise causes the clock jitter. Assuming that $\omega_c t = 2n\pi$ (where n is an integer),

$$s_p(t) \approx \sin(\omega_c \frac{v_p(t)}{\omega_c}). \tag{1.12}$$

The clock jitter is then calculated as

$$\begin{aligned} \tau[n] &= \frac{v_p(\frac{2n\pi}{\omega_c})}{\omega_c} \\ &= \frac{v_p(\frac{n}{f_c})}{\omega_c} \\ &= \frac{v_p(nt_c)}{\omega_c}, \end{aligned} \tag{1.13}$$

where t_c is a clock period of the PLL. The clock jitter directly causes the timing jitter, which deteriorates the SNR of the received signal.

1.4.3 Distortion due to Baseband Filter

The FS OFDM system can achieve the diversity with the single antenna [1.29]. However, it suffers from the correlation of the noise components as the sampling rate of the FS is higher than the baud rate. Suppose that the transmitted signal with the guard interval (GI), $u[l]$, is given as

$$u[l] = \frac{1}{\sqrt{N}} \sum_{k=0}^{N-1} s[k] e^{-j2\pi kl/N}, \quad l = 0, ..., P-1, \tag{1.14}$$

where N is the inverse discrete Fourier transform (IDFT) length, $s[k]$ is the symbol transmitted on the k-th subcarrier, P is the sum of the IDFT length and the length of GI. The received signal, $y(t)$, is expressed as follows,

$$y(t) = \sum_{l=0}^{P-1} u[l] h(t - lT_s) + v(t), \tag{1.15}$$

where $1/T_s$ is the baud rate, $h(t)$ is the impulse response of the composite channel and is given by $h(t) = (p \star c \star p')(t)$, $\star$ denotes convolution, $p(t)$ is the impulse

response of the pulse shaping filter (=Tx or Rx baseband filter), $p'(t) = p(-t)$, $c(t)$ is the impulse response of the physical channel, and $v(t)$ is the additive white Gaussian noise [1.29]. The received signal which is sampled at a rate of G/T_s is expressed as follows,

$$y_g[n] = \sum_{l=0}^{P-1} u[l]h_g[n-l] \quad + \quad v_g[n], \qquad g = 0, \cdots, G-1, \tag{1.16}$$

where n is the time index, $y_g[n] = y(nT_s + gT_s/G)$, $h_g[n] = h(nT_s + gT_s/G)$, and $v_g[n] = v(nT_s + gT_s/G)$. The demodulated signal received on the k-th subcarrier, $z[k]$, is derived after removal of the GI and demodulation by the DFT at the receiver for each g. $z[k]$ is expressed as

$$\mathbf{z}[k] = \mathbf{H}[k]s[k] + \mathbf{w}[k], \quad k = 0, \cdots, N-1, \tag{1.17}$$

where

$$\begin{aligned}
\mathbf{z}[k] &= [z_0[k], \cdots, z_{G-1}[k]]^T, && (1.18)\\
z_g[k] &= \frac{1}{\sqrt{N}} \sum_{n=0}^{N-1} y_g[n] e^{-j2\pi kn/N}, && (1.19)\\
\mathbf{H}[k] &= [H_0[k], \cdots, H_{G-1}[k]]^T, && (1.20)\\
H_g[k] &= \sum_{n=0}^{L-1} h_g[n] e^{-j2\pi kn/N}, && (1.21)\\
\mathbf{w}[k] &= [w_0[k], \cdots, w_{G-1}[k]]^T, && (1.22)\\
w_g[k] &= \sum_{n=0}^{N-1} v_g[n] e^{-j2\pi kn/N}, && (1.23)
\end{aligned}$$

and L is the number of multipath.

When sampling at the receiver is carried out at the baud rate of $1/T_s$, we have a usual OFDM input/output relationship with white noise. However, when sampling is performed at the multiple of the baud rate, the noise is colored. Noise whitening is necessary if maximal ratio combing (MRC) is employed since it maximizes the SNR when the noise is white. In order to take subcarrier-based MRC combining approach, subcarrier-by-subcarrier noise whitening is carried out. The covariance matrix of the noise on the k-th subcarrier is given as

$$\mathbf{R}_w[k] = \mathrm{E}[\mathbf{w}[k]\mathbf{w}^H[k]], \tag{1.24}$$

where E[ ] denotes expectation and H represents Hermitian transpose. After noise

whitening, Eq. (1.17) is converted as

$$\mathbf{R}_w^{-\frac{1}{2}}[k]\mathbf{z}[k] = \mathbf{R}_w^{-\frac{1}{2}}[k]\mathbf{H}[k]s[k] + \mathbf{R}_w^{-\frac{1}{2}}[k]\mathbf{w}[k]. \tag{1.25}$$

This equation turns to the following expression.

$$\mathbf{z}'[k] = \mathbf{H}'[k]s[k] + \mathbf{w}'[k], \tag{1.26}$$

where $\mathbf{R}_w^{-\frac{1}{2}}[k]\mathbf{z}[k] = \mathbf{z}'[k]$, $\mathbf{R}_w^{-\frac{1}{2}}[k]\mathbf{H}[k] = \mathbf{H}'[k]$, and $\mathbf{R}_w^{-\frac{1}{2}}[k]\mathbf{w}[k] = \mathbf{w}'[k]$. The estimate of $s[k]$, $\hat{s}[k]$, through MRC is then given as

$$\begin{aligned} \hat{s}[k] &= \frac{\mathbf{H}'^H[k]\mathbf{z}'[k]}{\mathbf{H}'^H[k]\mathbf{H}'[k]} \\ &= \frac{(\mathbf{R}_w^{-\frac{1}{2}}[k]\mathbf{H}[k])^H\mathbf{R}_w^{-\frac{1}{2}}[k]\mathbf{z}[k]}{(\mathbf{R}_w^{-\frac{1}{2}}[k]\mathbf{H}[k])^H\mathbf{R}_w^{-\frac{1}{2}}[k]\mathbf{H}[k]}. \end{aligned} \tag{1.27}$$

In terms of noise components, when sampling at the receiver is carried out at the baud rate of $1/T_s$, an usual OFDM input/output relationship with white noise can be obtained as shown in Fig. 1.18 (a). However, when sampling is performed at the multiple of the baud rate, the noise is colored as shown in Fig. 1.18 (b).

In order to derive the effect of the noise whitening, the received signal is expressed in the vector form. From Eq. (1.17), the received signal for all N subcarriers is expressed as

$$\mathbf{z} = \mathbf{H}\mathbf{s} + \mathbf{w}, \tag{1.28}$$

where

$$\mathbf{z} = [\mathbf{z}^T[0], \cdots, \mathbf{z}^T[N-1]]^T, \tag{1.29}$$

$$\mathbf{H} = \mathrm{diag}[\mathbf{H}[0], \cdots, \mathbf{H}[N-1]], \tag{1.30}$$

$$\mathbf{s} = [s[0], \cdots, s[N-1]]^T, \tag{1.31}$$

$$\mathbf{w} = [\mathbf{w}^T[0], \cdots, \mathbf{w}^T[N-1]]^T. \tag{1.32}$$

The noise vector $\mathbf{w}$ is colored and can be expressed as

$$\mathbf{w} = \mathbf{R}_w^{\frac{1}{2}}\boldsymbol{\omega}, \tag{1.33}$$

where $\mathbf{R}_w$ is the correlation matrix of the noise, $\boldsymbol{\omega}$ is the white noise in the vector form and it is given as

$$\boldsymbol{\omega} = [\boldsymbol{\omega}^T[0], \cdots, \boldsymbol{\omega}^T[N-1]]^T, \tag{1.34}$$

$$\boldsymbol{\omega}[k] = [\omega_0[k], \cdots, \omega_{G-1}[k]]^T, \tag{1.35}$$

and $\omega_g[k]$ is the white noise of the g-th sample component on the k-th subcarrier. The noise covariance matrix is $\mathbf{R}_w := \mathrm{E}[\mathbf{w}\mathbf{w}^H]$ whose $(k_1G + g_1, k_2G + g_2)$-th element is given by

$$\begin{aligned} & \mathrm{E}[w_{g1}[k_1]w^*_{g2}[k_2]] \\ = \; & {\sigma^2}_v \frac{1}{N} \sum_{n_1=0}^{N-1} \sum_{n_2=0}^{N-1} p_2((n_2 - n_1 + (g_2 - g_1)/G)T_s) \\ \times \; & e^{j\frac{2\pi}{N}(k_2 n_2 - k_1 n_1)} \end{aligned} \tag{1.36}$$

where $p_2(t)$ is the composite response of the filters given as $p_2(t) = (p \star p)(t)$, ${\sigma^2}_v$ is the variance of $v(t)$, $\{k_1, k_2\} = 0, \cdots, N-1$, and $\{g_1, g_2\} = 0, \cdots, G-1$. After subcarrier-based noise whitening, Eq. (1.28) is converted as

$$\mathbf{R}_{ww}\mathbf{z} = \mathbf{R}_{ww}\mathbf{H}\mathbf{s} + \mathbf{R}_{ww}\mathbf{w}, \tag{1.37}$$

where $\mathbf{R}_{ww} = \mathrm{diag}[\mathbf{R}_w^{-\frac{1}{2}}[0], \cdots, \mathbf{R}_w^{-\frac{1}{2}}[N-1]]$. Equation (1.37) results in the following equation.

$$\mathbf{z}' = \mathbf{H}'\mathbf{s} + \mathbf{w}', \tag{1.38}$$

where

$$\begin{aligned} \mathbf{z}' &= \mathbf{R}_{ww}\mathbf{z} \\ &= [\mathbf{z}'^T[0], \cdots, \mathbf{z}'^T[N-1]]^T, \end{aligned} \tag{1.39}$$

$$\begin{aligned} \mathbf{H}' &= \mathbf{R}_{ww}\mathbf{H} \\ &= \mathrm{diag}[\mathbf{H}'[0], \cdots, \mathbf{H}'[N-1]], \end{aligned} \tag{1.40}$$

and

$$\begin{aligned} \mathbf{w}' &= [\mathbf{w}'^T[0], \cdots, \mathbf{w}'^T[N-1]]^T \\ &= \mathbf{R}_{ww}\mathbf{w} \\ &= \mathbf{R}_{ww}\mathbf{R}_w^{\frac{1}{2}}\boldsymbol{\omega} \\ &= \begin{bmatrix} \mathbf{I_G} & \mathbf{R}_n[0,1] & \cdots & \mathbf{R}_n[0,N-1] \\ \mathbf{R}_n[1,0] & \mathbf{I_G} & \ddots & \vdots \\ \vdots & \ddots & \ddots & \vdots \\ \mathbf{R}_n[N-1,0] & \cdots & \cdots & \mathbf{I_G} \end{bmatrix} \\ &\times \begin{bmatrix} \boldsymbol{\omega}[0] \\ \boldsymbol{\omega}[1] \\ \vdots \\ \boldsymbol{\omega}[N-1] \end{bmatrix}, \end{aligned} \tag{1.41}$$

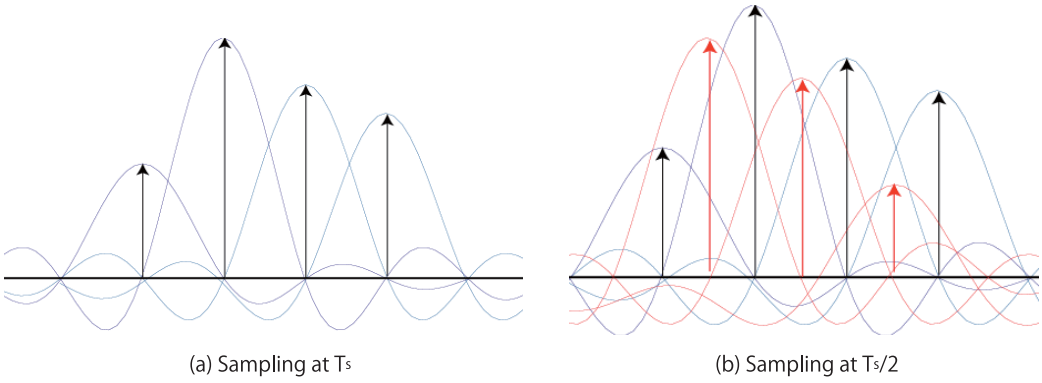

Figure 1.18: Correlation between noise components.

where $\mathbf{R}_n[k_1, k_2]$ is the $G \times G$ matrix, which corresponds to the (k_1, k_2)-th subblock of the $NG \times NG$ matrix, $\mathbf{R}_{ww}\mathbf{R}_w^{\frac{1}{2}}$. The g_1-th element of $\mathbf{w}'[k_1]$ is expressed as

$$\begin{aligned} {w'}_{g_1}[k_1] &= \sum_{k_2=0}^{N-1}\sum_{g_2=0}^{G-1}[\mathbf{R}_n[k_1,k_2]]_{g_1,g_2}\omega_{g_2}[k_2] \\ &= \omega_{g_1}[k_1] + \sum_{\substack{k_2=0 \\ k_2\neq k_1}}^{N-1}\sum_{g_2=0}^{G-1}[\mathbf{R}_n[k_1,k_2]]_{g_1,g_2}\omega_{g_2}[k_2], \end{aligned} \tag{1.42}$$

where $[\mathbf{R}_n[k_1, k_2]]_{g_1,g_2}$ is the (g_1, g_2)-th element of $\mathbf{R}_n[k_1, k_2]$. The second term of the right side of this equation gives the correlation between the noise components after subcarrier based noise whitening. These components may deteriorate the BER performance of the receiver. The correlation among the noise components is determined by the impulse response of the filter because the noise passes through the pulse shaping filter.

The cancellation scheme of the correlation among the noise components depending on the impulse response of the pulse shaping filter in OFDM system is discussed in Chapters 7 and 8.

1.5 Motivation of this Research

Future wireless systems are required to provide high data rate communications in the order of more than 100Mbps. Mobile terminals need to enable the users to access networks anywhere anytime. The receiver architecture is required to satisfy the conditions such as high-performance, low power consumption, small size, low

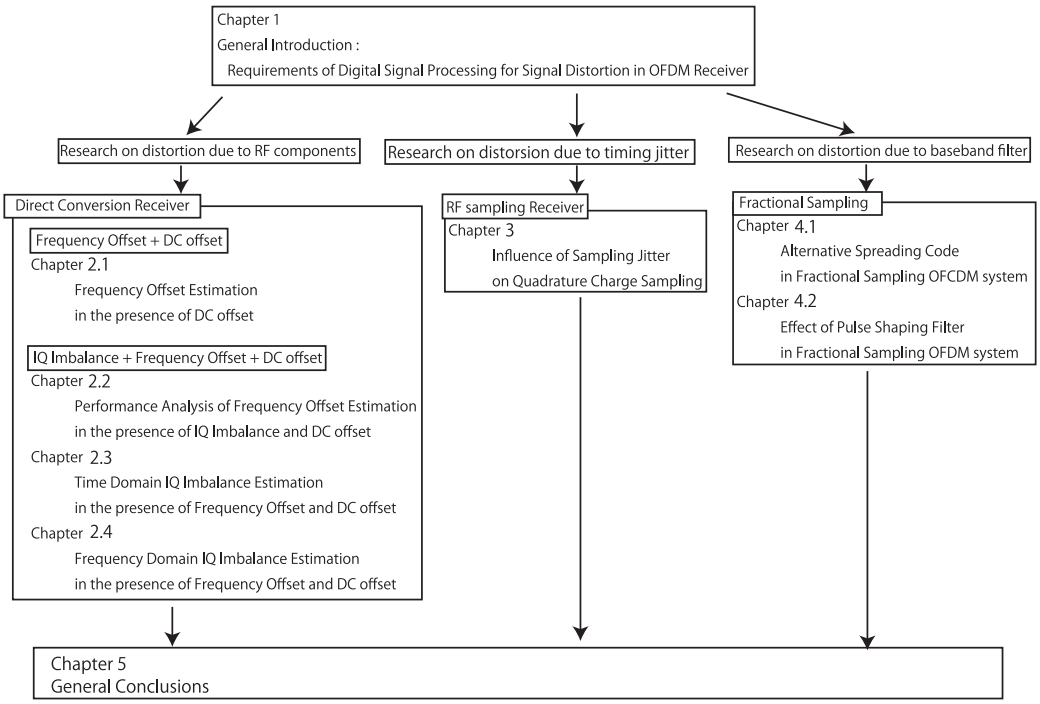

Figure 1.19: Overall structure of this research.

cost, and high efficiency components. However, in the receivers that deal with the bandwidth of from 10MHz to 100MHz, more accuracy of analog components is necessary while it demands cost and higher power consumption. To realize a low cost and low power consumption, digital compensation schemes for signal distortion have been investigated in this dissertation. The signal distortion compensation in the digital domain brings more scalability and flexibility.

This dissertation discusses the digital compensation schemes in OFDM receivers. The contents of this dissertation are mainly divided into three parts as shown in Fig. 1.19.
(1) Signal distortion due to RF components (Chapter 2)
(2) Signal distortion due to PLL (Chapter 3)
(3) Signal distortion due to baseband filters (Chapter 4)
Finally, this dissertation is concluded in Chapter 5. The relationship between research topics and the overall receiver architecture is illustrated in Fig. 1.20.

In Chapter 2, compensation schemes for signal distortion due to RF components in a direct conversion receiver are investigated. In terms of the signal distortion due to RF components, as studied in Section 1.3.2, frequency offset, DC offset,

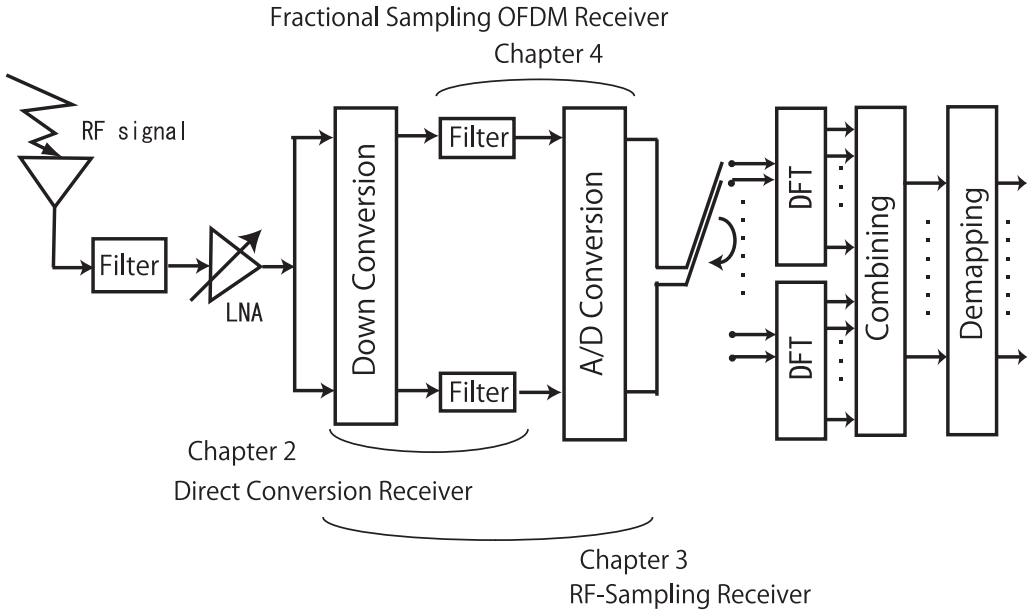

Figure 1.20: Relationship of this research.

and IQ imbalance are the main causes of the signal distortion. In the OFDM direct conversion receiver, the DC offset may be eliminated by a high pass filter (HPF) as shown in Fig. 1.8 [1.19]. However, as the gain of the LNA changes, the DC offset level varies [1.30]. The higher frequency components of the time-varying DC offset pass through the HPFs. These components deteriorate the accuracy of frequency offset estimation. Several joint compensation schemes have been presented [1.31][1.32]. In [1.32], the DC offset is estimated with the presence of controlled frequency offset and specific training sequence. If the amount of the frequency offset is unknown, this scheme is not applicable. In [1.31], the frequency offset is estimated in the presence of the DC offset. In this scheme, the DC offset estimation is carried out first and the residual DC offset and the frequency offset are then estimated concurrently. This scheme requires the condition that the mean of the preamble is zero. However, none of the proposed schemes have accounted for the time-variant DC offset and the frequency offset at the same time. For instance, in the IEEE 802.11 a/g receivers with the HPF, the residual DC offset through the HPF should converge rapidly because the preamble period is considerably short. Therefore, in order to minimize the convergence time, the cut off frequency of the HPF has to be significantly large [1.33]. However, it is not desirable to use the HPF with a large cutoff frequency as it may eliminate the energy of the received

signal. In Section 2.1, the frequency offset estimation scheme in the presence of time-varying DC offset for OFDM direct conversion receivers is discussed. The key idea of the proposed schemes is the use of a differential filter, which detects the level shift of the DC offset. The frequency offset can be estimated by simple calculation with using training sequence.

In addition to the DC offset, this architecture may suffer from the IQ imbalance in the mixers [1.23]. The IQ imbalance also deteriorates the performance of the frequency offset estimation scheme with the differential filter. Section 2.2 analyzes the performance of the frequency offset estimation scheme with the differential filter in the presence of the IQ imbalance and the time-varying DC offset. The IQ imbalance estimation as well as frequency offset estimation is essential to improve the performance in the receiver.

Many publications have focused on IQ imbalance estimation [1.34]-[1.38]. In [1.34], the frequency offset and the IQ imbalance are estimated using a nonlinear least-squares scheme. This scheme requires the covariance matrix of the received samples. In [1.35], the IQ imbalance as well as the frequency offset and the DC offset is estimated using the maximum likelihood criterion. Although this scheme achieves a performance close to the Cramer-Rao bound, it requires a large amount of computation and channel response. In [1.36], a frequency offset and IQ imbalance estimation scheme is proposed on the basis of simple calculation. The scheme in [1.23] carries out frequency offset and IQ imbalance estimation in the time domain. The IQ imbalance estimation schemes presented in [1.37][1.38] are conducted in the frequency domain. However, these schemes assume the absence of the DC offset. In Section 2.3, the time domain IQ imbalance estimation in the presence of the frequency offset and the time-varying DC offset for the OFDM direct conversion receivers are introduced. From the output of the differential filter, the IQ imbalance as well as the frequency offset is estimated from a simple equation.

However, the accuracy of the proposed time domain IQ imbalance estimation in Section 2.3 is deteriorated when the frequency offset is small. To overcome this problem, a new IQ imbalance estimation scheme in the frequency domain has been proposed in Section 2.4. The proposed scheme uses a specific combination of symbols on symmetric pilot subcarriers. It works well if the frequency offset is relatively small. The relationship of the researches about signal distribution due to RF components (Chapter 2) is shown in Fig. 1.21.

RF sampling receiver allows the reduction of design complexity in the RF front-end. Charge sampling is carried out at the front-end of the receiver. In contract to

voltage sampling, the charge sampling mixer integrates the signal current instead of tracking the signal voltage. However, the timing jitter in clock signal due to the phase noise in the PLL may cause the SNR reduction in the sampled signal. The effect of the timing jitter on the charge sampling has been analyzed [1.39][1.40].

However, none of these literatures have assumed the application of the charge sampling mixer to wireless receivers. In the wireless receiver, the received signal consists of the I-phase and Q-phase components, which are sampled by quadrature sampling [1.25][1.41]. The receiver may lose the orthogonality between the I-phase and Q-phase components due to timing jitter and suffer from crosstalk between them. In Chapter 3, the effect of the timing jitter on quadrature charge sampling is discussed. The distributions of the timing jitter based on the phase noise in the PLL is investigated. The relationship of the research about signal distribution due to the timing jitter (Chapter 3) is shown in Fig. 1.22.

In wireless communication systems, better communication quality can be obtained through diversity, interleaving, and coding [1.42]. One of the typical diversity schemes is antenna diversity in which multiple antenna elements are implemented in a receiver [1.26][1.28].However, it may be difficult to implement multiple antenna elements in a small mobile terminal. An OFDM receiver with FS achieves path diversity through oversampling and parallel signal demodulation with a single antenna [1.29]. FS can be used for the OFDM-based systems such as orthogonal frequency and code division multiplexing (OFCDM), which is recognized as a promising candidate for the modulation scheme of IMT-advanced . The OFCDM system transmits a signal using more than 1000 subcarriers that are orthogonally overlapped in a frequency domain. However, as the number of subcarriers and the oversampling ratio increase, the correlation among the noise components over different subcarriers deteriorates the bit error rate (BER) performance. The correlation among the noise components is determined by the impulse response of the filter since the noise passes through the pulse shaping filter (baseband filter) in the receiver.

In Section 4.1, a correlated noise cancellation scheme in FS OFCDM is investigated. To reduce the correlated noise, an alternative spreading code is used in the FS OFCDM system. This spreading code has positive and negative components alternatively. Despreading with the alternative spreading code cancels most of the correlated noise components. Section 4.2 discusses the effect of the correlation among the noise components in FS OFDM system. A metric weighting scheme for the coded FS OFDM is also proposed and investigated. The relationship of the research about the signal distortion due to baseband filters (Chapter 4) is shown

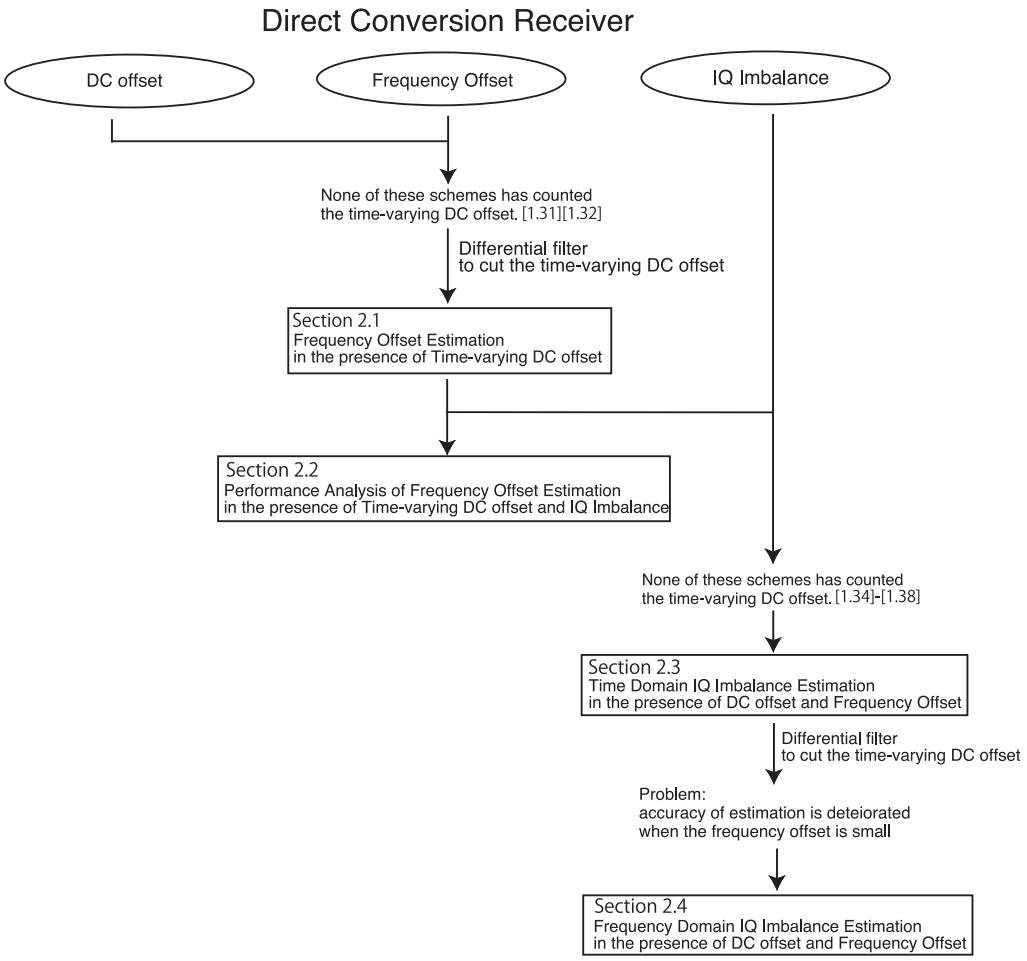

Figure 1.21: Overall model about distortion due to RF components.

in Fig. 1.23.

Chapter 5 presents overall conclusion of this dissertation. Table 1.3 shows the outline of the proposed approaches from Chapter 2 to Chapter 4.

1.6 References

[1.1] T. Hattori and M. Fujioka, "Wireless Broadband Textbook Vol.1," Impress, 2006.

[1.2] T. Hattori and M. Fujioka, "Wireless Broadband Textbook Vol.2," Impress, 2006.

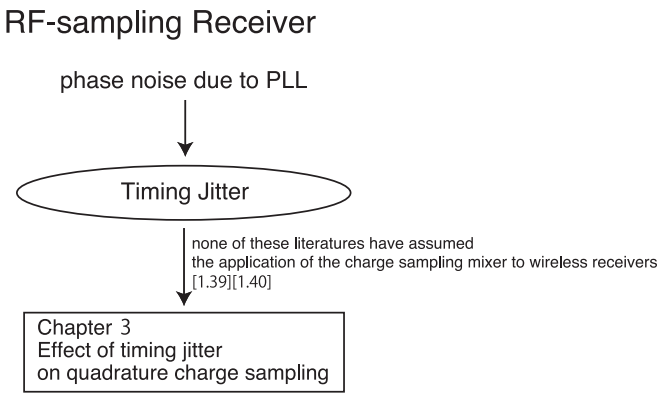

Figure 1.22: Overall model about distortion due to PLL.

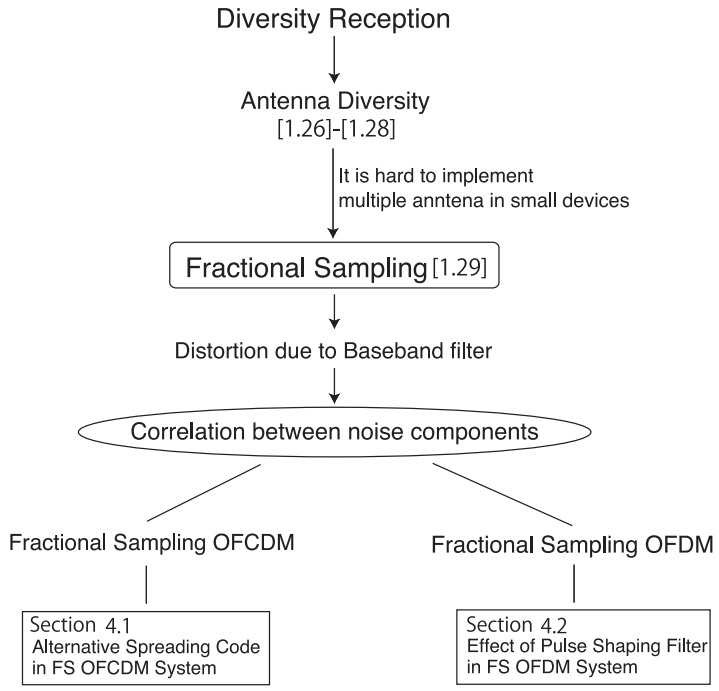

Figure 1.23: Overall model about distortion due to baseband filters.

[1.3] D. Falconer, F. Adachi, and B. Gudmundson, "Time Division Multiple Access Methods for Wireless Personal Communications," IEEE Communications Magazine, vol.33, no.1, pp.50-57, Jan. 1995.

[1.4] R. Kohno, R. Meidan, and L. B. Milstein, "Spread Spectrum Access Methods for Wireless Communications," IEEE Communications Magazine, vol.33,

Table 1.3: Outline of the proposed approaches.

Chapter 2	Purpose	Compensate the signal distortion due to RF components in direct conversion receiver
	Research issue	Frequency offset and IQ imbalance estimation in the presence of time-varying DC offset
	Proposed scheme	Differential filter to cut the DC offset
	Achievement	The proposed low-complexity estimation scheme with differential filter has shown the superior performance as compared with the conventional scheme with high pass filter, which is suitable for low-cost and low-power-consumption direct conversion receivers.
Chapter 3	Purpose	Compensate the signal distortion due to PLL in RF-sampling jitter
	Research issue	Analyze the effect of the timing jitter on the charge sampling
	Proposed scheme	Model the phase noise in PLL and analyze the distributions of the timing jitter based on the phase noise
	Achievement	The timing jitter deteriorates the SINR of the demodulated signal due to the crosstalk between the I-phase and Q-phase components of the received signal.
Chapter 4	Purpose	Compensate the signal distortion due to baseband filter in FS OFDM system
	Research issue	Cancel the correlation between noise components
	Proposed scheme	Alternative spreading code and pulse shaping filter
	Achievement	Despreading with the alternative spreading code cancels most of the correlated noise components in FS OFCDM system. The Frobenius norm of a whitening matrix corresponding to the pulse shaping filter has significant effect on the BER performance especially with a small numbers of subcarriers in FS OFDM system.

no.1, pp.58-67, Jan. 1995.

[1.5] IEEE 802.15-05-648r0, "IEEE P802.15 Working Group for Wireless Personal Area Networks (WPANs)," IEEE 802.15, Dec. 2002.

[1.6] IEEE.802.11b-1999.

[1.7] IEEE.802.11a-Part 11: Wireless LAN Medium Access Control (MAC) and Physical Layer (PHY) specifications; Highspeed Physical Layer in the 5GHZ Band.

[1.8] IEEE.802.11g-Part 11: Wireless LAN Medium Access Control (MAC) and Physical Layer (PHY) specifications; Highspeed Physical Layer in the 2.4GHZ Band.

[1.9] Y. Xiao, "IEEE 802.11n: enhancements for higher throughput in wireless LANs," IEEE Communications Magazine, vol.12, no.6, pp.82-91, Dec. 2005.

[1.10] IEEE.802.16-Part 16: Air Interface for Fixed Broadband Wireless Access Systems, 2004, IEEE Std. 802.16.

[1.11] IEEE 802.20 WG, "PAR Form," IEEE 802.20 PD-02, Dec.11, 2002.

[1.12] R. Chang and R. Gibby, "A Theoretical Study of Performance of an Orthogonal Multiplexing Data Transmission Scheme," IEEE Trans. on Commun., vol.16, no.4, pp.529-540, Oct. 1968.

[1.13] S. Weinstein, and P. Ebert, "Data Transmission by Frequency-Division Multiplexing Using the Discrete Fourier Transform," IEEE Trans. on Commun., vol.19, no.5, pp.628-634, Oct. 1971.

[1.14] L. J. Cimini, Jr., "Analysis and Simulation of a Digital Mobile Channel Using Orthogonal Frequency Division Multiplexing," IEEE Trans. on Commun,, vol.33, no.7, pp.665-675, July 1985.

[1.15] J. G. Proakis, M. Salehi, and G. Bauch, "Contemporary Communication Systems using MATLAB and SIMULINK," the second edition, Thomson-Brooks/Cole, 2004.

[1.16] S. Mirabbasi and K. Martin, "Classical and modern receiver architectures," IEEE Communications Magazine, vol.38, no.11, pp.132-139, Nov. 2000.

[1.17] Nikkei Electronics, pp.132-139, no.773, July 2007.

[1.18] A. Abidi, "Direct-conversion radio transceivers for digital communications," IEEE J. Solid-State Circuits, vol.30, no.12, pp.1399-1410, Dec. 1995.

[1.19] W. Namgoong and T. H. Meng, "Direct-conversion RF Receiver Design," IEEE Trans. on Commun., vol.49, no.3, pp.518-529, March 2001.

[1.20] R. Svitek and S. Raman, "DC offsets in direct-conversion receivers: characterization and implications," IEEE Microwave Magazine, vol.6, no.3, pp.76-86, Sept. 2005.

[1.21] J. Li, G. Liu, and G. B. Giannakis, "Carrier Frequency Offset Estimation for OFDM-based WLANs," IEEE Trans. on Signal Processing Letters, vol.8, no.3, March 2001.

[1.22] T. Yuba and Y. Sanada, "Decision Directed Scheme for IQ Imbalance Compensation on OFCDM Direct Conversion Receiver," IEICE Trans. on Commun., vol.E89-E, no.1, pp.184-190, Jan.2006.

[1.23] J. Tubbax, A. Fort, L. V. Perre, S. Donnay, M. Moonen, and H. D. Man, "Joint Compensation of IQ Imbalance and Frequency Offset in OFDM Systems," Proc. of IEEE Global Telecommunications Conference, vol.3, pp.2365-2369, May 2003.

[1.24] R. H. Walden, "Performance Trends for Analog-to-Digital Converters," IEEE Communications Magazine, vol.37, no.2, pp.96-101, Feb. 1999.

[1.25] K. Muhammad, D. Leipold, B. Staszewski, Y. C. Ho, C. M. Hung, K. Maggio, C. Fernando, T. Jung, J. Wallberg, J. S. Koh, S. John, I. Deng, O. Moreira, R. Staszewski, R. Katz, and O. Friedman, "Discrete-Time Bluetooth Receiver in a 0.13 μ m Digital CMOS Process," Proc. of International Solid-State Circuits Conference, vol.1, pp.268-527, Feb. 2004.

[1.26] N. Maeda, H. Atarashi, S. Abeta, and M. Sawahashi, "Antenna Diversity Reception Appropriate for MMSE Combining in Frequency Domain for Forward Link OFCDM Packet Wireless Access", IEICE Trans. on Commun., vol.E85-B, no.10, pp.1966-1977, Oct. 2002.

[1.27] N. Miki, H. Atarashi, and M. Sawahashi, "Effect of Time Diversity in Hybrid ARQ Considering Space and Path Diversity for VSF-OFCDM Downlink Broadband Wireless Access", Proc. of the 15th IEEE Symposium on Personal Indoor and Mobile Radio Communications 2004, pp.604-608 vol.1, Sep. 2004.

[1.28] K. Suto and T. Otsuki, "Space-Time-Frequency Block Codes over Frequency Selective Fading Channels", IEICE Trans. on Commun., vol.E86-B, no.7, pp.1939-1945, July 2004.

[1.29] C. Tepedelenlioglu and R. Challagulla, "Low-Complexity Multipath Diversity Through Fractional Sampling in OFDM," IEEE Trans. on Signal Processing, vol.52, no.11, pp.3104-3116, Nov. 2004.

[1.30] S. Otaka, T. Yamaji, R. Fujimoto, and H. Tanimoto, "A Low Offset 1.9-GHz Direct Conversion Receiver IC with Spurious Free Dynamic Range of over

67 dB," IEICE Trans. on Fundamentals, vol.E84-A, no.2, pp.513-519, Feb. 2001.

[1.31] C. K. Ho, S. Sun, and P. He, "Low complexity frequency offset estimation in the presence of DC offset, " Proc. of International Conference on Communications, vol.3, pp.2051-2055, May 2003.

[1.32] D. Hui, B. Lidoff, and K. Zangi, "Enhanced DC Estimation via Sequence-Specific Frequency Offset," Proc. of the 56th IEEE Vehicular Technology Conference, vol.1, pp.161-165, Sept. 2002

[1.33] J. Olsson, "WLAN/WCDMA Dual-Mode Receiver Architecture Design Trade-Offs," Proc. of the 6th IEEE Circuits and Systems Symposium, vol.2, pp.725-728, May 2004.

[1.34] G. Xing, M. Shen, and H. Liu, "Frequency Offset and I/Q Imbalance Compensation for Direct Conversion Receivers," IEEE Trans. on Commun., vol.4, no.2, pp.673-680, March 2005.

[1.35] G. T. Gil, I. H. Sohn, Y. H. Lee, Y. I. Song, and J. K. Park, "Joint ML Estimation of Carrier Frequency, Channel, I/Q Mismatch, and DC Offset in Communications Receivers," in IEEE Trans. on Veh. Tech., vol.54, no.1, pp.338-349, Jan. 2005.

[1.36] S. D. Rore, E. L. Estraviz, F. Horlin, and L. V. Perre, "Joint Estimation of Carrier Frequency Offset and IQ Imbalance for 4G Mobile Wireless Systems," Proc. of International Conference on Communications, vol.5, pp.2066-2071, June 2006.

[1.37] M. Windisch and G. Fettweis, "On the Performance of Standard-Independent I/Q Imbalance Compensation in OFDM Direct-Conversion Receivers," Proc. of the 13th European Signal Processing Conference, Sept. 2005.

[1.38] Y. Egashira, Y. Tanabe, and K. Sato, "A Novel IQ Imbalance Compensation Method with Pilot-Signals for OFDM System," IEICE Trans. on Commun., vol.E91-B, no.5, pp.558-565, May 2008. (In Japanese)

[1.39] S. Karvonen, T. Riley, and J. Kostamovaara, "On the Effects of Timing Jitter in Charge Samping," Proc. of International Symposium on Circuits and Systems, vol.1, pp.737-740, May 2003.

[1.40] G. Xu and J. Yuan, "Performance Analysis of General Charge Sampling," IEEE Trans. on Circuts and Systems-II:Express Briefs, vol.52, pp.107-111, no.2, Feb. 2005.

[1.41] S. Karvonen, T. A. D. Riley, and J. Kostamovaara, "A CMOS Quadrature Charge-Domain Sampling Circuit with 66-dB SFDR up to 100HMz," IEEE Trans. on Circuits and Systems-I, vol.52, no.2, pp.105-117, Mar. 2003.

[1.42] M. Itami, "OFDM Modulation Technique," Triceps, 2000.

Chapter 2

Frequency Offset and IQ Imbalance Estimation Scheme in the Presence of Time-varying DC offset for Direct Conversion Receivers

In this chapter, compensation schemes for signal distortion in a direct conversion receiver are discussed. The OFDM direct conversion receiver is superior to a superheterodyne receiver in cost, size, and power consumption. However, this receiver architecture suffers from DC offset, frequency offset, and IQ imbalance. In the proposed scheme, the key idea is to use a differential filter for the reduction of the DC offset. In Section 2.1, the frequency offset estimation scheme in the presence of time-varying DC offset is presented. The performance analysis of the frequency offset estimation scheme with the differential filter in the presence of IQ imbalance is derived in Section 2.2. In Section 2.3 and Section 2.4, time and frequency domain IQ imbalance estimation schemes in the presence of the frequency offset and the DC offset are proposed. The IQ imbalance is calculated in time domain using a simple equation without the impulse response of a channel in the presence of the frequency offset and the DC offset.

2.1 Frequency Offset Estimation Scheme in the Presence of Time-varying DC Offset for Direct Conversion Receivers

This section presents a frequency offset estimation scheme for OFDM direct conversion receivers. The key idea is to employ the differential filter for reduction of the DC offset. Frequency offset is estimated in the presence of the time-varying DC offset base on the IEEE 802.11a/g training sequence. In order to overcome the varying DC levels under automatic gain control (AGC) circuits, a threshold level is set for the output of the differential filter. The proposed compensation scheme is compared with a conventional scheme with a high pass filter.

2.1.1 Introduction

IEEE standard 802.11a/g has become the most popular WLAN standard. In this system, OFDM is used as a modulation scheme to realize high data rate transmission. OFDM achieves high frequency utilization efficiency if the orthogonality of subcarriers is kept. However, at the receiver, frequency offset may deteriorate the orthogonality between the subcarriers. The frequency offset is caused by oscillators' mismatch between the transmitter and receiver.

The direct conversion architecture has been implemented for WLAN receivers. Direct conversion receivers may suffer from the problems such as DC offset. The main source of the DC offset is LO, as shown in Fig. 2.1. The LO signal can mix with itself down to zero IF, resulting in the generation of the DC offset. This is known as self-mixing, which is due to finite isolation typical between the LO and RF ports of a LNA or a mixer. Moreover, the DC offset is attributed to the mismatch between the mixer components [2.1][2.2].

Therefore, in OFDM direct conversion architecture, not only the frequency offset but also the DC offset deteriorate the received signal. In the presence of the DC offset, the frequency offset can not be estimated well. Several joint compensation schemes have been presented [2.3]-[2.5]. In [2.1], a HPF is used to reduce the DC offset. In [2.3], DC offset is estimated with the presence of controlled frequency offset and specific training sequence. If the amount of the frequency offset is unknown, this scheme is not applicable. In [2.4], the frequency offset and the DC offset are estimated as well as IQ imbalance with the maximum likelihood criterion. Though this scheme achieves the performance close to the Cramer-Rao bound, it requires large amount of computation. In [2.5], the frequency offset is

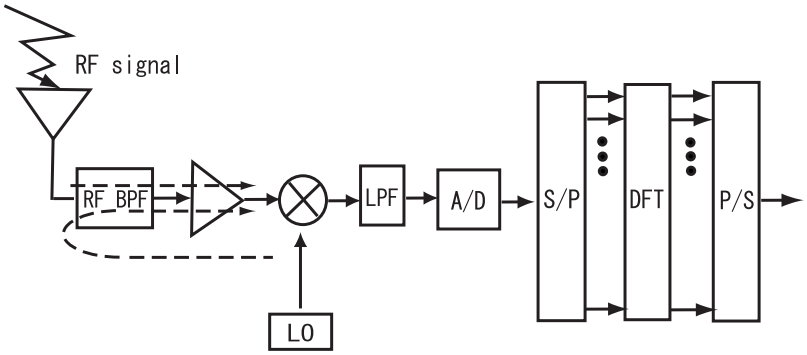

Figure 2.1: OFDM direct conversion architecture.

estimated in the presence of the DC offset. In this scheme, DC offset estimation is carried out first. The residual DC offset and the frequency offset are then estimated concurrently. This scheme requires the condition that the mean of the preamble is zero.

None of these schemes has counted the time-varying DC offset. The DC offset is varied because of gain shift in the LNA. Though the HPF is employed in order to eliminate the DC offset, the higher frequency components of the time-varying DC offset may pass through the HPFs. On the other hand, in IEEE 802.11a/g, the received signal has a dynamic range of more than 50[dB]. To receive these wide dynamic range signals with a low-cost and low-power A/D converter correctly, the LNA gain must be switched. The 802.11a preamble is used for various receiving processes such as signal detection, AGC, diversity selection, timing synchronization, and channel and frequency offset estimation. Thus, only the beginning of the preamble is allowed for the first three processes [2.6]. Therefore, frequency offset estimation suffers from the residual of the time-varying DC offset.

In this section, a new frequency offset estimation scheme is proposed. The proposed scheme can estimate the frequency offset in the presence of the time-varying DC offset. The key idea is the use of differential filter, which detects the level shift of the DC offset and also alleviate the constant DC offset. The frequency offset can be estimated by simple calculation.

This section is organized as follows. Subsection 2.1.2 gives the system model and the preamble structure. In subsection 2.1.3, the conventional and proposed schemes are explained. Subsection 2.1.4 shows the numerical results through computer simulation. Subsection 2.1.5 gives our conclusions.

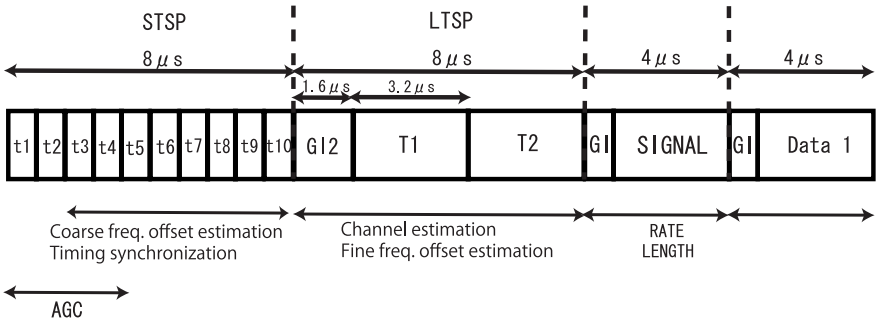

Figure 2.2: IEEE 802.11a/g burst structure.

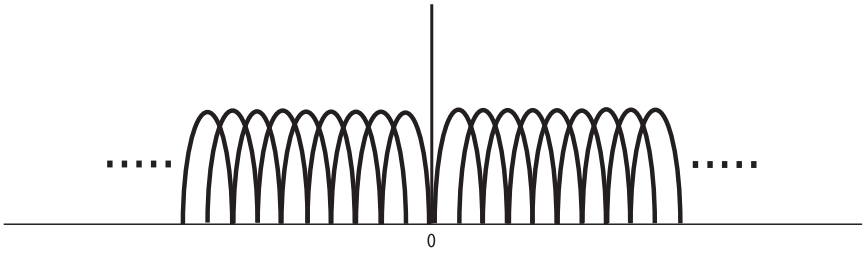

Figure 2.3: Subcarriers allocation.

2.1.2 System Model

2.1.2.1 Preamble Model

Figure 2.2 shows the IEEE 802.11a/g burst structure of the preamble signal [2.8][2.9]. In 802.11a/g preamble, short training sequence preamble (STSP) symbols and long training sequence preamble (LTSP) symbols are used for frequency estimation. In Fig. 2.2, t_1 to t_{10} are STSP symbols and T_1 and T_2 are LTSP symbols.

The STSP symbols consist of 12 subcarrier signals, which is repeated with a period of $0.8\mu s$ ($= T_{DFT}/4 = 3.2/4$), where T_{DFT} is IDFT/DFT period. On the other hand, the LTSP symbols consist of 52 subcarrier signals, which has two period of $3.2\mu s (= T_{DFT})$.

In this section, it is assumed that the frequency offset is estimated two times. Coarse estimation is carried out with the STSP symbols and it is re-estimated with the LTSP symbols as fine estimation.

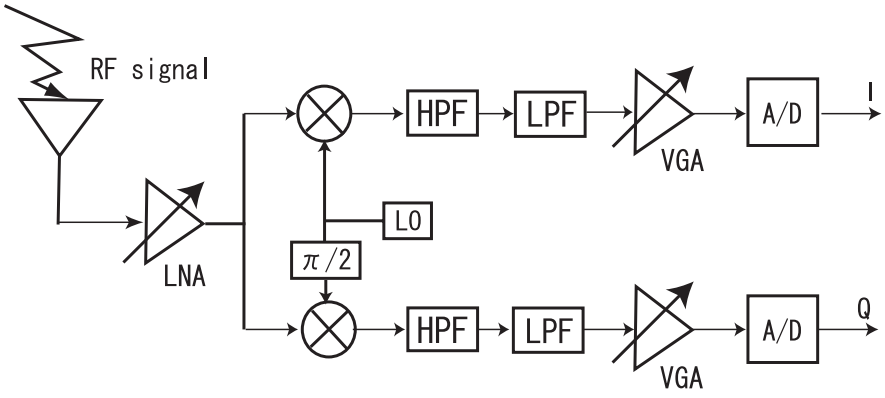

Figure 2.4: Receiver architecture.

2.1.2.2 Subcarrier Allocation

In the IEEE 802.11a/g, subcarrier at frequency zero is not used. This is for avoiding the interference from the DC offset. Figure 2.3 shows subcarrier allocation. Though the subcarriers do not interfere with each other, if frequency offset exists, the orthogonality between the subcarriers and the DC offset is deteriorated.

However, as number zero subcarrier is not used, the DC offset does not interfere to the OFDM subcarriers. Also, a HPF can be used to eliminate the DC offset without removing the received signal.

2.1.2.3 RF Architecture and Automatic Gain Control

In order to keep the received signal amplitude at a proper fixed level, AGC circuits are used. In a WLAN system, at the middle of STSP, AGC controls the received signal gain. In 802.11a/g standard, gain control of more than 50[dB] is required [2.6]. Assumed RF architecture in this section is shown in Fig. 2.4. As shown in this figure, gain control is applied in both LNA and variable gain amplifiers (VGAs). Here, the LNA with two gain modes is assumed. This kind of LNAs has been presented in literatures such as [2.7] or [2.11].

In the direct conversion receiver, DC offset may be eliminated by HPFs as shown in Fig. 2.4 [2.1][2.7]. However, as the gain of the LNA changes, DC offset level varies [2.12]. The higher frequency components of the time-varying DC offset pass through the HPFs. These components deteriorate the accuracy of frequency offset estimation.

In this section, mean square error (MSE) of frequency offset estimation under the time-varying DC offset is discussed. It is assumed that AGC controls the power

of the received signal at the end of the STSP symbol t_4. Moreover, DC offset level is assumed to vary with the two step function model as the LNA has only two gain modes [2.13][2.14].

2.1.3 Frequency Offset Estimation

2.1.3.1 Coarse Estimation and Fine Estimation

As mentioned in Section 2.1.2.1, the frequency offset is estimated two times. First, it is calculated with the STSP symbols (coarse frequency offset estimation). However, not all the STSP symbols are used. Since t_1 and t_2 symbols may suffer from the effect of the delayed signals due to multi-path and filter delay, these signals are not used for frequency offset estimation. Thus, the coarse frequency offset estimation is calculated with t_3 to t_{10} symbols. After the first estimation, the frequency offset is re-estimated with the LTSP symbols (T_1 and T_2) (fine frequency offset estimation).

2.1.3.2 Conventional Scheme

In the presence of the DC offset, it is difficult to estimate the frequency offset accurately.

In order to reduce the DC offset, a HPF with low cutoff frequency is often used [2.1]. The effect of the DC offset is alleviated by selecting the cutoff frequency appropriately.

Assuming that the n-th digitized sample of the OFDM preamble in time domain is defined as $s[n]$, the received signal with frequency offset is expressed

$$r[n] = s[n] \exp(j\frac{2\pi\alpha}{N}n) + \delta[n] + v[n], \tag{2.1}$$

where N is the number of the samples for DFT, $\delta[n]$ is the n-th residual DC offset through the HPF, α is the frequency offset normalized by subcarrier separation, and $v[n]$ is the n-th AWGN sample with zero mean and variance ${\sigma^2}_v$.

The frequency offset is estimated in STSP as follows.

$$\alpha_{co}^{'} = \frac{4}{2\pi} \arg\{\sum_{m=2}^{8} \sum_{n=0}^{\frac{N}{4}-1} r_{SP}^{*}[n + \frac{mN}{4}] r_{SP}[n + \frac{mN}{4} + \frac{N}{4}]\}, \tag{2.2}$$

where $r_{SP}[n]$ is the n-th signal in STSP. Based on the estimated value, the frequency offset is compensated. The residual frequency offset is estimated in LTSP

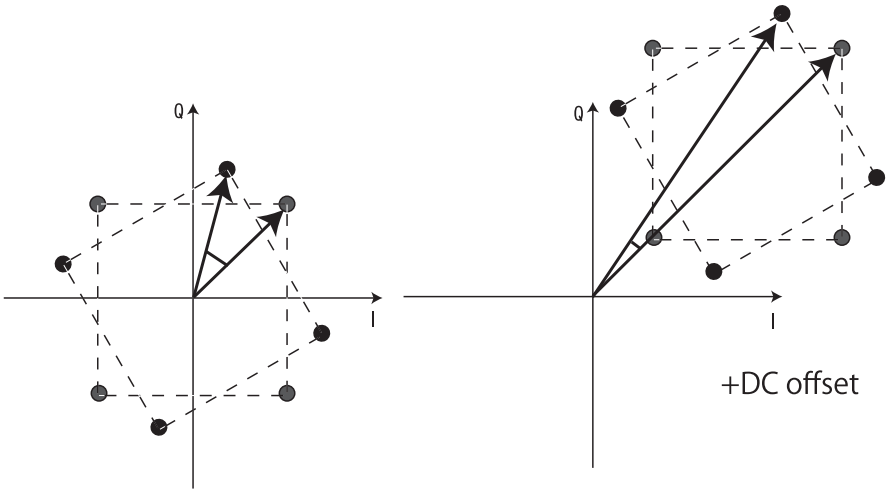

Figure 2.5: Effect of DC offset in conventional scheme.

as follows.

$$\alpha_{co}^{''} = \frac{1}{2\pi} \arg\{\sum_{n=0}^{N-1} r_{LP}^{*}[n] r_{LP}[n+N]\}, \tag{2.3}$$

where $r_{LP}[n]$ is the n-th received signal in LTSP. As a result, the total frequency offset $\hat{\alpha}_{co}$ is estimated as

$$\hat{\alpha}_{co} = \alpha_{co}^{'} + \alpha_{co}^{''}. \tag{2.4}$$

2.1.3.3 Proposed Scheme

In the conventional scheme, time-varying DC offset is not assumed. However, due to the AGC, the power of the DC offset may change in the middle of the STSP. If the level of the DC offset changes, the residual DC offset in Eq. (2.1) may increase and deteriorate the estimation accuracy of the frequency offset as shown in Fig. 2.5.

On the other hand, the proposed scheme can estimate the frequency offset under the time-varying DC offset. The baseband model of the proposed scheme is shown in Fig. 2.6. The frequency offset and the DC offset are added to the received signal. Then, the AWGN channel is added. After high pass filtering, the received signal is digitized and put into the differential filter. The DC offset reduction and the frequency offset estimation are carried out during the preamble period. Then, the STSP and LTSP preamble signals pass through the differential filter to cut the

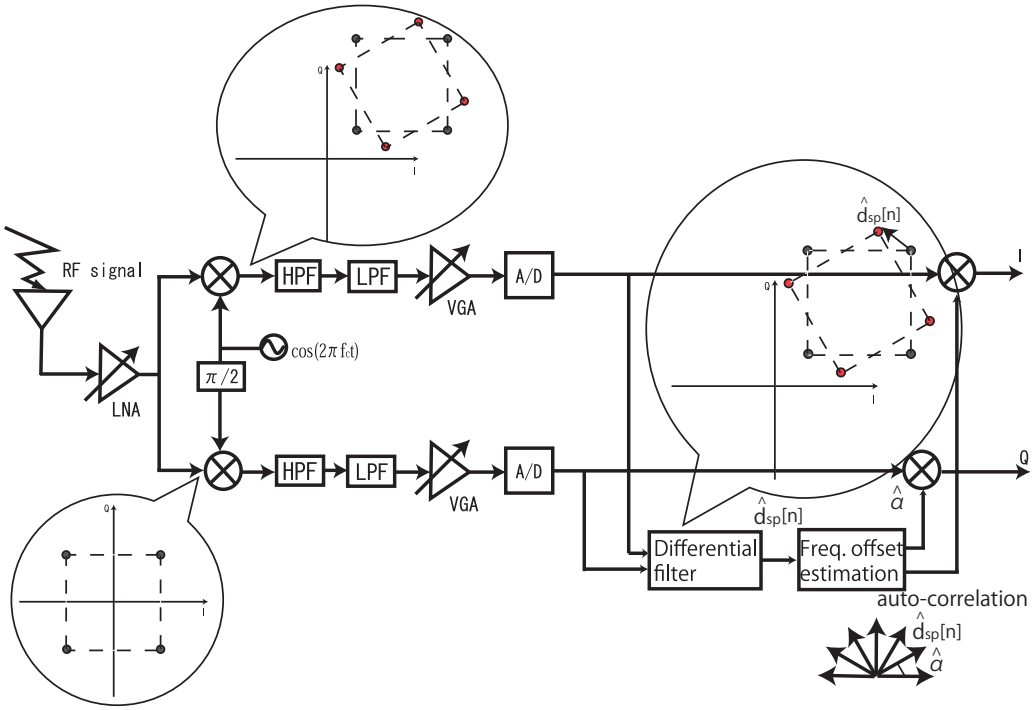

Figure 2.6: Overall system model.

residual DC offset. The frequency offset is then estimated with the auto-correlation values of the output of the differential filter.

The frequency offset is estimated as follows. The n-th STSP output signal $d_{SP}[n]$ after differential filtering is given as

$$d_{SP}[n] = r_{SP}[n] - r_{SP}[n-1], \ n \geq 1 \tag{2.5}$$

where $r_{SP}[n]$ is the n-th signal in the STSP period. In STSP, the short preamble period with the period of $N/4$ samples are repeated 10 times. Therefore, it is

shown in the absence of AWGN that

$$\begin{aligned}
& d_{SP}[n+\frac{N}{4}] \\
= \; & r_{SP}[n+\frac{N}{4}] - r_{SP}[n+\frac{N}{4}-1] \\
= \; & -\left[s_{SP}[n+\frac{N}{4}] \exp\{j\frac{2\pi\alpha}{N}(k+\frac{N}{4})\} + \delta[n+\frac{N}{4}] \right] \\
& -\left[s_{SP}[n+\frac{N}{4}-1] \exp\{j\frac{2\pi\alpha}{N}(n+\frac{N}{4}-1)\} + \delta[n+\frac{N}{4}-1] \right] \\
= \; & r_{SP}[n]\exp(j\frac{2\pi\alpha}{4}) - r_{SP}[n-1]\exp(j\frac{2\pi\alpha}{4}) \\
& -\Delta\delta[n,n-1]\exp(j\frac{2\pi\alpha}{4}) + \Delta\delta[n+\frac{N}{4}, n+\frac{N}{4}-1] \\
= \; & d_{SP}[n]\exp(j\frac{2\pi\alpha}{4}) - \Delta\delta[n,n-1]\exp(j\frac{2\pi\alpha}{4}) + \Delta\delta[n+\frac{N}{4}, n+\frac{N}{4}-1]
\end{aligned} \tag{2.6}$$

where $\Delta\delta[n, n-1]$ is the difference of the n-th and $[n-1]$-th residual DC offset samples, which is relatively small and has smaller effect to automatic frequency control (AFC) than the conventional scheme. From Eqs. (2.5) and (2.6), the frequency offset estimation with STSP α' is hence

$$\alpha_{pr}^{'} = \frac{4}{2\pi}\arg\{\sum_{m=2}^{8}\sum_{n=0}^{\frac{N}{4}-1} d_{SP}^{*}[n+\frac{mN}{4}] d_{SP}[n+\frac{mN}{4}+\frac{N}{4}]\}, \tag{2.7}$$

where $d_{SP}[n]$ is the n-th output of the differential filter in STSP. Meanwhile, in LTSP, the coarse frequency offset value obtained in STSP is used for compensation. Since the same signal is repeated 2 times, residual frequency offset value α'' is calculated as follows,

$$\alpha_{pr}^{''} = \frac{1}{2\pi}\arg\{\sum_{n=1}^{N-1} d_{LP}^{*}[n] d_{LP}[n+N]\}, \tag{2.8}$$

where $d_{LP}[n]$ is the n-th output of the differential filter in LTSP. As a result, the fine frequency estimation $\hat{\alpha}_{pr}$ is expressed as

$$\hat{\alpha}_{pr} = \alpha_{pr}^{'} + \alpha_{pr}^{''}. \tag{2.9}$$

2.1.3.4 Time-varying DC Offset

In this section, it is assumed that the gain of the LNA is switched at the beginning of the STSP symbol t_5, as shown in Fig. 2.7(a). According to the gain shift,

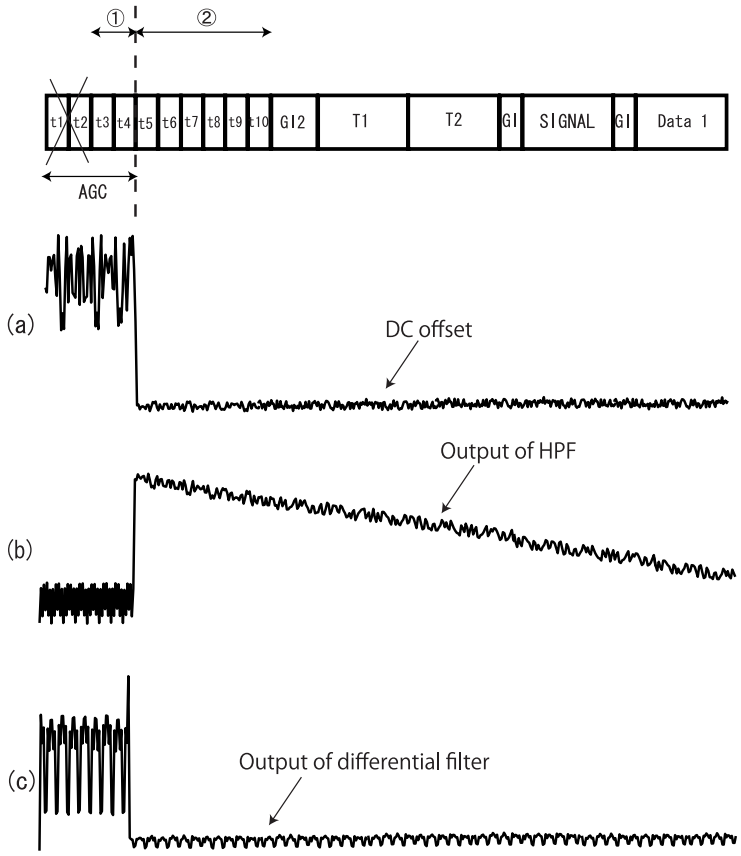

Figure 2.7: DC offset and the output of differential filter.

the level of the DC offset changes. Here, it is modeled as the two step function [2.13][2.14].

The signal with the time-varying DC offset contains higher frequency components, as shown in Fig. 2.7(a). Thus, at the output of the HPF, the residual DC offset increases. The residual DC offset then deteriorates the accuracy of frequency offset estimation in the conventional scheme. Based on cut off frequency of the HPF, the residual DC offset may overlap to the LTSP symbols, as shown in Fig. 2.7(b).

On the other hand, in the proposed scheme, the residual DC offset through the HPF is cut by the differential filter, as shown in Fig. 2.7(c). The output signal of the differential filter reflects the variation of the residual DC offset. Only the sharp impulse waveform is output from the differential filter at the same timing as the gain shift. If this sharp impulse waveform is put into the frequency offset estimation

Table 2.1: Simulation conditions.

Trial number	1,000,000 times
Modulation scheme	QPSK+OFDM
Number of subcarrier	64
Number of data subcarrier	52
Channel	AWGN
Rx HPF	1st order Butterworth filter f_B=1,10,100[kHz]
LNA gain	35/15[dB]
Normalized frequency offset	0.1-0.5

circuits, the MSE of the estimated frequency offset will increase. Therefore, the output of the differential filter exceeds the threshold, the corresponding samples are not used for frequency offset estimation. The threshold level can be calculated according to the amount of the gain shift of the LNA and the received signal level. The receive signal strength indicator (RSSI) circuit before the LNA or after the HPF can detect the received signal level.

2.1.4 Numerical Results

2.1.4.1 Simulation Conditions

The MSE of the frequency offset estimation is evaluated through computer simulation. The simulation conditions are shown in Table 2.4. Information bits are modulated with QPSK on each subcarrier. The number of DFT/IDFT points is set to 64 while 52 subcarriers are used for the LTSP symbols, which follows IEEE 802.11a/g standard. The 1st order butterworth filter is employed as the Rx HPF. The cutoff frequency of the received HPF is set from 1[kHz] to 100[kHz]. The normalized frequency offset is from 0.1 to 0.5.

Figure 2.8 shows the model of the LNA and the mixer. The gain of the LNA can be selected between 35 and 15[dB] [2.15]. The isolation between LO output and LNA input is assumed as -60[dB] [2.15]. Therefore, if the LO signal power is set to 0[dBm], the DC offset level is -25/-45[dBm].

On the other hand, the received signal power is set to -53[dBm] which is equivalent to -70[dBm] on each subcarrier in LTSP. This is the case when the DC offset is 10[dB] larger than the signal power on each subcarrier.

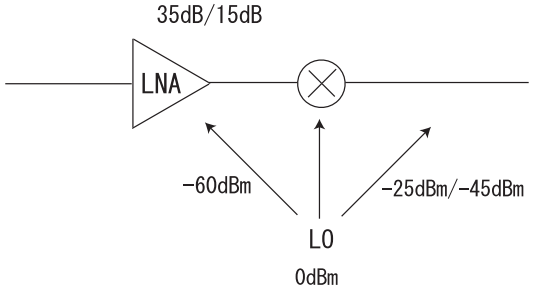

Figure 2.8: LO leakage.

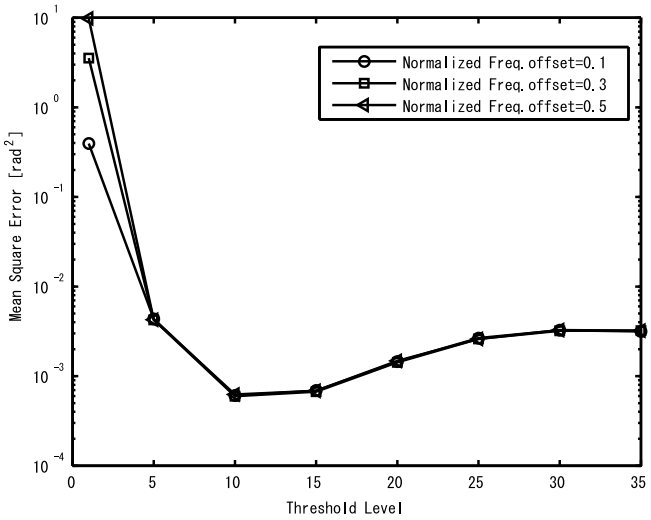

Figure 2.9: MSE vs. threshold level performance of frequency offset estimation (cutoff freq.=1[kHz], E_b/N_0=15[dB]).

2.1.4.2 MSE vs. Threshold Level Under Time-varying DC Offset

As mentioned in Section 2.1.3.4, at the beginning of t_5, the gain of the LNA is shifted. The output of the differential filter then generates the sharp impulse waveform. In order to detect this gain shift, the output of the differential filter is compared with the threshold. Figures 2.9 to 2.11 show the relationship between the MSE of frequency offset estimation and the threshold of the proposed scheme only with STSP (coarse). The threshold level is normalized by the average signal amplitude on each subcarrier in LTSP for representation. E_b/N_0 is 15[dB]. From these figures, it is clear that the optimum performance can be obtained if the appropriate threshold level is chosen.

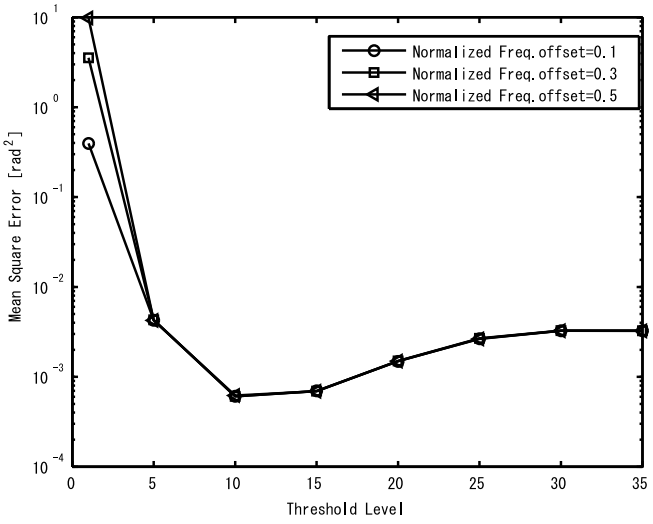

Figure 2.10: MSE vs. threshold level performance of frequency offset estimation (cutoff freq.=10[kHz], E_b/N_0=15[dB]).

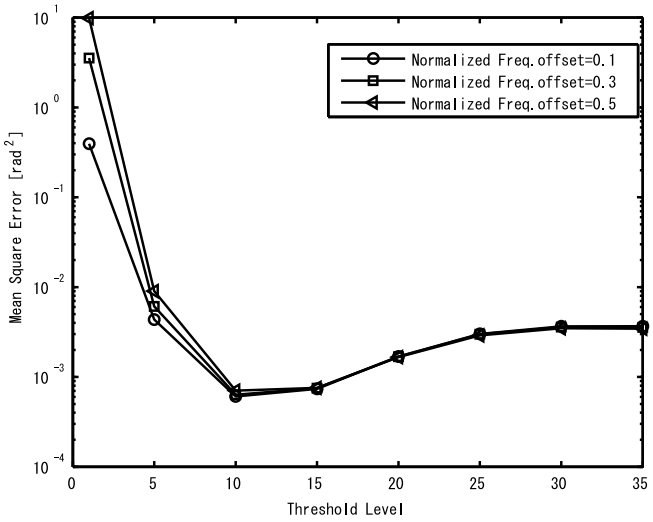

Figure 2.11: MSE vs. threshold level performance of frequency offset estimation (cutoff freq.=100[kHz], E_b/N_0=15[dB]).

If the threshold level is too small, even the received signal may exceed the threshold. If it is too large, the residual time-variant DC offset output from the differential filter may be included in the estimation of the frequency offset. This

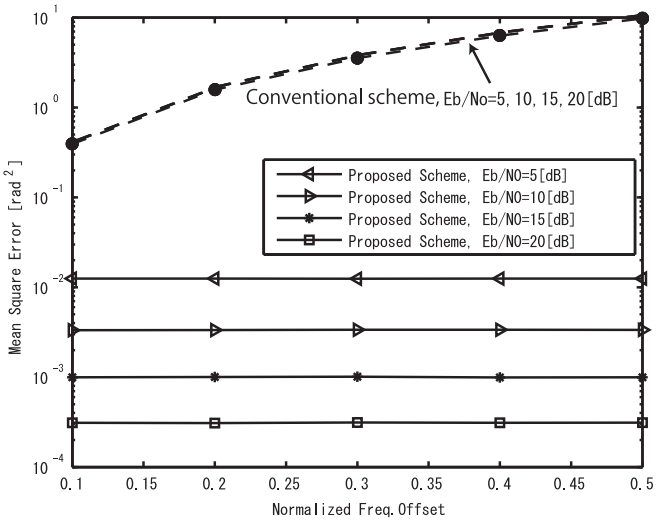

Figure 2.12: MSE performance of frequency offset estimation under time-varying DC offset (coarse+fine, cutoff freq.=10[kHz]).

tendency does not depend on the cutoff frequency of the HPF. The threshold level does not have to be decided strictly and should be set at around 10 to 15.

2.1.4.3 MSE of Frequency Estimation Under Time-varying DC Offset

Figure 2.12 shows the MSE performance of the conventional scheme and the proposed scheme with STSP and LTSP (coarse+fine) under time-varying DC offset. From Section 2.1.4.2, the normalized threshold level is set to 10. It is clear that the MSE of the proposed scheme does not depend on the normalized frequency offset. It is only affected by the noise variance. On the other hand, the conventional scheme suffers from the residual DC offset output from the HPF. When the cutoff frequency is 1[kHz] or 100[kHz], the similar performance can be obtained as in Fig. 2.12.

2.1.4.4 MSE vs. Threshold Level Under Constant DC Offset

Figure 2.13 shows the MSE performance of the conventional scheme and the proposed scheme with STSP and LTSP (coarse+fine) under constant DC offset. If the DC offset is in steady state, it is clear that the conventional scheme is superior to the proposed scheme. This is because the differential filter increases the noise variance at the output. However, the difference is small enough to use the proposed

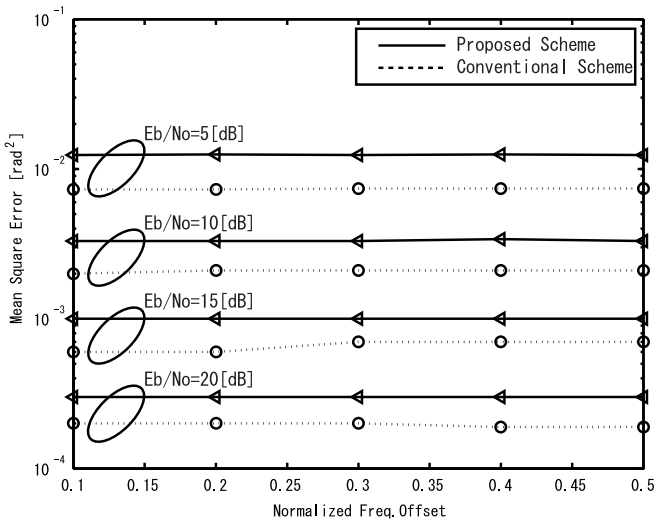

Figure 2.13: MSE performance of frequency offset estimation under constant DC offset (coarse+fine, cutoff freq.=10[kHz]).

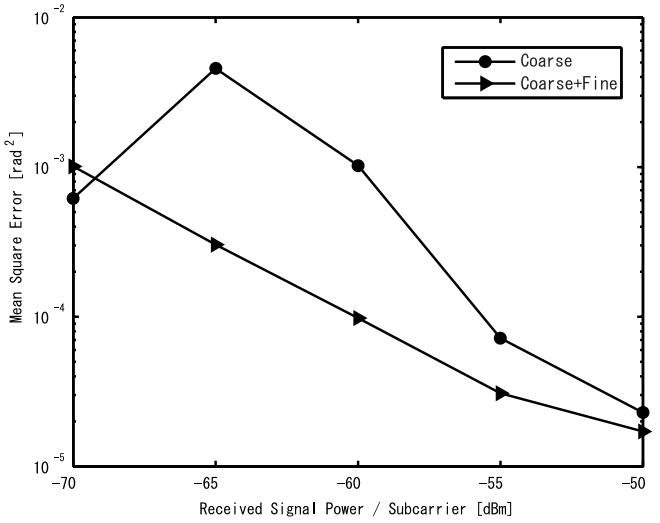

Figure 2.14: MSE vs. received signal power (E_b/N_0=15[dB], cutoff freq.=10[kHz]).

scheme.

2.1.4.5 MSE under Various Received Signal Power

Figure 2.14 shows the MSE performance of the proposed scheme vs. the received signal power only with STSP (coarse) and with STSP and LTSP (coarse+fine). Here, the normalized frequency offset is set to 0.3, the cutoff frequency of HPF is set to 10[kHz], and E_b/N_0 is 15[dB]. Moreover, the normalized threshold level is set to the optimum level at each received signal power.

As for the coarse estimation, it is clear that if the received signal power is small, the level shift of the DC offset can be detected by setting the threshold at the output of the differential filter. This is because the difference between DC offset and the received signal power is large. On the other hand, if the received signal power is large, the residual DC offset is relatively small as compared with the received signal. Therefore, as the received signal power increases more than -65[dBm], the MSE decreases.

On the other hand, the residual DC offset is eliminated by the differential filter in LTSP. As received signal power increases, the MSE for coarse+fine estimation then reduces.

2.1.5 Conclusions

In this section, the frequency offset estimation scheme in the presence of the time-varying DC offset has been proposed. As compared with the conventional scheme, it is shown that the residual DC offset is eliminated with the differential filter by setting the optimum threshold level. The frequency offset can be estimated accurately with the proposed scheme while the conventional scheme suffers from the residual DC offset.

2.2 Performance Analysis of Frequency Offset Estimation in the Presence of IQ Imbalance for OFDM Direct Conversion Receivers with Differential Filter

In WLAN receivers, the direct conversion architecture has been implemented in recent years. Though this architecture reduces cost and power consumption, it may suffer from the DC offset and the frequency offset. To reduce the effect of the DC offset, a frequency offset estimation scheme with differential filter for OFDM direct conversion receivers has been proposed. However, the receiver may also suffer from the IQ imbalance, which deteriorates the performance of frequency offset

estimation. In this section, the performance analysis of the frequency offset estimation scheme with the differential filter in the presence of IQ imbalance is derived. Evaluation of the presented estimation scheme is carried out on an OFDM communication system designed to the specifications of the IEEE 802.11a/g standard for WLANs.

2.2.1 Introduction

At the receiving end, a direct conversion architecture has been implemented. As mentioned in Section 2.1, the direct conversion receivers may suffer from the problem of DC offset [2.1][2.2].

In order to eliminate the time-varying DC offset, we have proposed a frequency offset estimation scheme with a differential filter [2.19][2.28]. However, the direct conversion receiver may also suffer from the IQ imbalance [2.21]. This IQ imbalance is mainly attributed to the mismatched components along the I and Q paths. The IQ imbalance also deteriorates the performance of the frequency offset estimation scheme with the differential filter. The purpose of this section is to analyze the performance of the proposed frequency offset estimation scheme in the presence of the IQ imbalance (the DC offset is assumed to be eliminated in the HPF). It is also clarified that the MSE of frequency offset estimation depends on the waveform of the preamble symbols. This dependency is also caused by IQ imbalance.

This section is organized as follows. Subsection 2.2.2 gives the system model. In subsection 2.2.3, the frequency offset estimation scheme using the differential filter is explained and the performance analysis is presented. Numerical results are discussed in subsection 2.2.4. Subsection 2.2.5 gives our conclusions.

2.2.2 System Model

The receiver architecture assumed in this section is shown in Fig. 2.15. In this section, the performance of proposed estimation scheme with the differential filter is analyzed on the same training sequence of the IEEE 802.11a/g standard as Section 2.1. During the period of the LTSP as shown in Fig. 2.2, the OFDM training symbols for channel estimation are transmitted [2.8][2.9]. Therefore, frequency offset needs to be estimated appropriately during the period of coarse estimation [2.6]. In this section, the coarse frequency offset estimation in STSP period is focused.

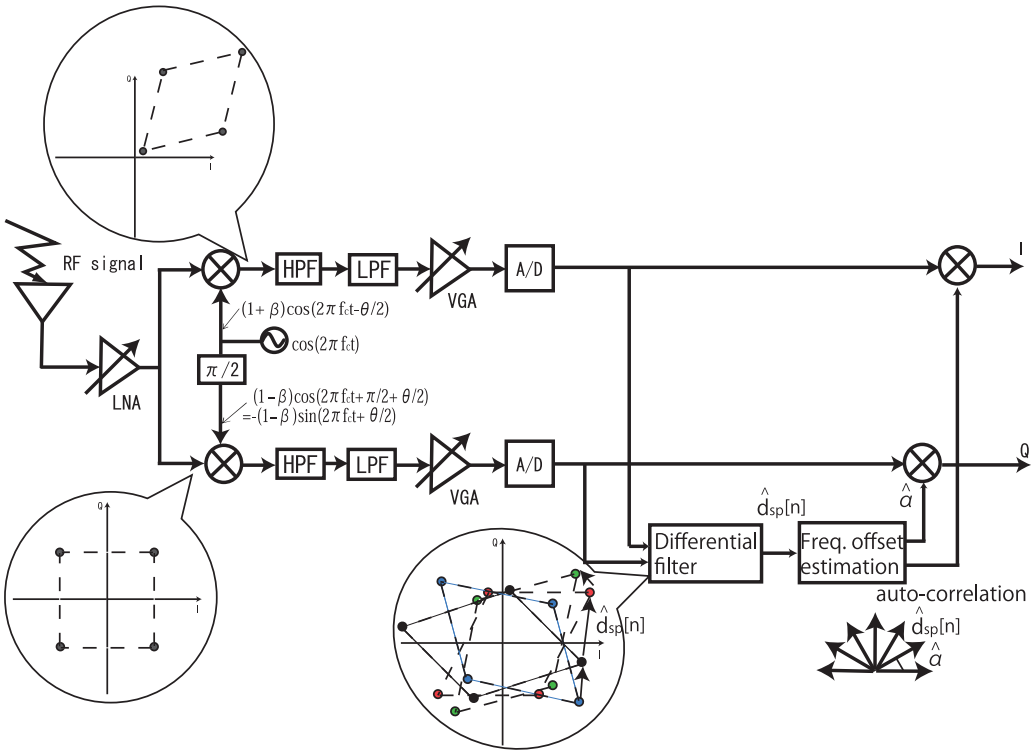

Figure 2.15: Receiver architecture.

2.2.3 Analysis of Frequency Offset Estimation

2.2.3.1 Frequency Offset Estimation with Differential Filter

From Eq. (1.5) in Chapter 1, the received signal with IQ imbalance in the time domain is given as

$$\hat{r}[n] = \phi r[n] + \psi^* r^*[n], \tag{2.10}$$

where

$$\phi = \cos(\frac{\theta}{2}) + j\beta \sin(\frac{\theta}{2}), \tag{2.11}$$

$$\psi = \beta \cos(\frac{\theta}{2}) + j \sin(\frac{\theta}{2}). \tag{2.12}$$

In the frequency offset estimation scheme, the received signal with IQ imbalance is substituted into the differential filter used to cut the residual DC offset that

passes through the HPF. The n-th output $\hat{d}_{SP}[n]$ after the differential filter is

$$\begin{aligned}\hat{d}_{SP}[n] &= \hat{r}_{SP}[n] - \hat{r}_{SP}[n-1] \\ &= \phi\{r_{SP}[n] - r_{SP}[n-1]\} + \psi^*\{r^*_{SP}[n] - r^*_{SP}[n-1]\},\ n \geq 1\end{aligned} \tag{2.13}$$

where

$$\hat{r}_{SP}[n] = \phi r_{SP}[n] + \psi^* r^*_{SP}[n], \tag{2.14}$$

$r_{SP}[n]$ is the n-th signal with the frequency offset in the STSP period. In the STSP, the short preamble with the period of $N/4$ samples are repeated 10 times. From Eq. (2.13), the auto-correlation value used for frequency offset estimation with the IQ imbalance is given as

$$\begin{aligned}&\hat{d}^*_{SP}[n]\hat{d}_{SP}[n+\frac{N}{4}] \\ =\ &[\phi\{r_{SP}[n] - r_{SP}[n-1]\} + \psi^*\{r^*_{SP}[n] - r^*_{SP}[n-1]\}]^* \\ &\cdot[\phi\{r_{SP}[n+\frac{N}{4}] - r_{SP}[n+\frac{N}{4}-1]\} + \psi^*\{r^*_{SP}[n+\frac{N}{4}] - r^*_{SP}[n+\frac{N}{4}-1]\}] \\ =\ &\rho_1[n] + \rho_2[n] + \rho_3[n] + \rho_4[n] + \rho_5[n] \\ &+\Delta(|\phi|^2 vv^*) + \Delta(\phi^*\psi^* v^*) + \Delta(\phi^*\psi^*(v^*)^2) \\ &+\Delta(\phi\psi v) + \Delta(\phi\psi v^2) + \Delta(|\psi|^2 v) + \Delta(|\psi|^2 v^*) + \Delta(|\psi|^2 vv^*),\end{aligned} \tag{2.15}$$

where,

$$\rho_1[n] = |\phi|^2 \Big| s_{SP}[n]\exp(j\frac{2\pi\alpha}{N}n) - s_{SP}[n-1]\exp(j\frac{2\pi\alpha}{N}(n-1))\Big|^2 \exp(j\frac{2\pi\alpha}{4}), \tag{2.16}$$

$$\rho_2[n] = \phi^*\psi^*\{s^*_{SP}[n]\exp(-j\frac{2\pi\alpha}{N}n) - s^*_{SP}[n-1]\exp(-j\frac{2\pi\alpha}{N}(n-1))\}^2 \exp(-j\frac{2\pi\alpha}{4}), \tag{2.17}$$

$$\rho_3[n] = \phi\psi\{s_{SP}[n]\exp(j\frac{2\pi\alpha}{N}n) - s_{SP}[n-1]\exp(j\frac{2\pi\alpha}{N}(n-1))\}^2 \exp(j\frac{2\pi\alpha}{4}), \tag{2.18}$$

$$\rho_4[n] = |\psi|^2 \Big| s_{SP}[n]\exp(j\frac{2\pi\alpha}{N}n) - s_{SP}[n-1]\exp(j\frac{2\pi\alpha}{N}(n-1))\Big|^2 \exp(-j\frac{2\pi\alpha}{4}), \tag{2.19}$$

$$
\begin{aligned}
\rho_5[n] &= |\phi|^2 v[n+\frac{N}{4}]\{s^*_{SP}[n]\exp(-j\frac{2\pi\alpha}{N}n) - s^*_{SP}[n-1]\exp(-j\frac{2\pi\alpha}{N}(n-1))\} \\
&- |\phi|^2 v[n+\frac{N}{4}-1]\{s^*_{SP}[n]\exp(-j\frac{2\pi\alpha}{N}n) - s^*_{SP}[n-1]\exp(-j\frac{2\pi\alpha}{N}(n-1))\} \\
&+ |\phi|^2 v^*[n]\{s_{SP}[n]\exp(j\frac{2\pi\alpha}{N}n) - s_{SP}[n-1]\exp(j\frac{2\pi\alpha}{N}(n-1))\}\exp(j\frac{2\pi\alpha}{4}) \\
&- |\phi|^2 v^*[n-1]\{s_{SP}[n]\exp(j\frac{2\pi\alpha}{N}n) - s_{SP}[n-1]\exp(j\frac{2\pi\alpha}{N}(n-1))\}\exp(j\frac{2\pi\alpha}{4}),
\end{aligned}
\tag{2.20}
$$

and $\Delta(|\phi|^2 vv^*)$, $\Delta(\phi^*\psi^* v^*)$, $\Delta(\phi^*\psi^*(v^*)^2)$, $\Delta(\phi\psi v)$, $\Delta(\phi\psi v^2)$, $\Delta(|\psi|^2 v)$, $\Delta(|\psi|^2 v^*)$, and $\Delta(|\psi|^2 vv^*)$ are the terms including the noise components that are $|\phi|^2 vv^*$, $\phi^*\psi^* v^*$, $\phi^*\psi^*(v^*)^2$, $\phi\psi v$, $\phi\psi v^2$, $|\psi|^2 v$, $|\psi|^2 v^*$, and $|\psi|^2 vv^*$, respectively. Also, $s_{SP}[n]$ is the n-th sample of the STSP symbol.

The estimated frequency offset with STSP, $\hat{\alpha}$, is given as

$$
\hat{\alpha} = \frac{4}{2\pi}\arg\{\sum_{n=N}^{\frac{9N}{4}-1} \hat{d}^*_{SP}[n]\hat{d}_{SP}[n+\frac{N}{4}]\}, \tag{2.21}
$$

where $n = N$ corresponds to the time index of the first symbol of t_5 and $n = \frac{9N}{4}-1$ corresponds to the time index of the last symbol of t_9. Here, the STSP symbols from t_5 to t_{10} are used for frequency offset estimation. The auto-correlations between t_1 and t_4 are not used because of passible gain shift of the LNA [2.19]. The total amount of the distortion in the sum of the auto-correlations depends on the number of the samples for summation and the waveform of the preamble signals.

2.2.3.2 MSE Performance

To evaluate the performance of frequency offset estimation with the differential filter, the MSE is analyzed. From Eq. (2.12), the absolute value of ψ is relatively small. Also $|v|^2$ is negligible as compared with the signal amplitude if the SNR is large enough. Therefore, Δ terms in Eq. (2.15) are neglected and it is assumed that Eq. (2.15) consists of 5 terms from $\rho_1[n]$ to $\rho_5[n]$, which indicates the effect of IQ imbalance. Vectors corresponding to those terms are given in Fig. 2.16. Without IQ imbalance, Eq. (2.15) has only one vector, $\rho_1[n]$. $\rho_2[n]$ is conjugate of $\rho_3[n]$. Thus the addition of $\rho_2[n]$ and $\rho_3[n]$ resolves in a vector with only a real component. $\rho_5[n]$ contains the noise components. The summation of terms from $\rho_2[n]$ to $\rho_5[n]$ deteriorates the accuracy of frequency offset estimation.

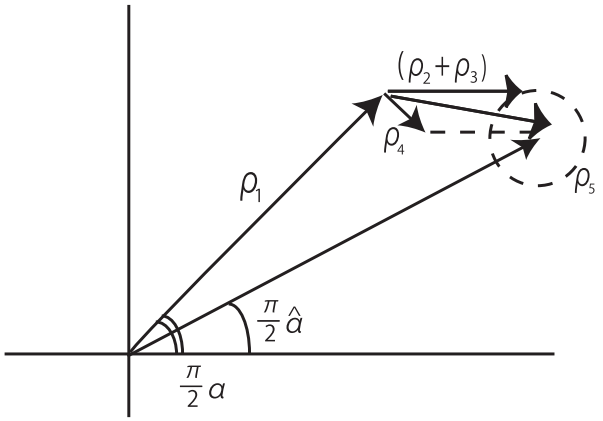

Figure 2.16: Vectors representation of auto-correlation.

Based on Eq. (2.15), the error of the estimation is given as

$$\alpha - \hat{\alpha} = \alpha - \frac{4}{2\pi}[\arg\{\sum_{n=N}^{\frac{9N}{4}-1} \rho_1[n] + \rho_2[n] + \rho_3[n] + \rho_4[n] + \rho_5[n]\}]. \quad (2.22)$$

The variance of $\rho_5[n]$ is expressed as

$$\begin{aligned} \sigma_v^2 &= \mathrm{E}\{|\sum_{n=N}^{\frac{9N}{4}-1} \rho_5[n]|^2\} \\ &= \mathrm{E}\{|\sum_{n=N}^{\frac{9N}{4}-1} \rho'[n] + \rho''[n] + \rho'''[n] + \rho''''[n]|^2\}. \end{aligned} \quad (2.23)$$

where from Eq. (2.20),

$$\rho'[n] = |\phi|^2 v[n + \frac{N}{4}]\{s_{SP}^*[n]\exp(-j\frac{2\pi\alpha}{N}n) - s_{SP}^*[n-1]\exp(-j\frac{2\pi\alpha}{N}(n-1))\}, \quad (2.24)$$

$$\rho''[n] = -|\phi|^2 v[n + \frac{N}{4} - 1]\{s_{SP}^*[n]\exp(-j\frac{2\pi\alpha}{N}n) - s_{SP}^*[n-1]\exp(-j\frac{2\pi\alpha}{N}(n-1))\}, \quad (2.25)$$

$$\rho'''[n] = |\phi|^2 v^*[n]\{s_{SP}[n]\exp(j\frac{2\pi\alpha}{N}n) - s_{SP}[n-1]\exp(j\frac{2\pi\alpha}{N}(n-1))\}\exp(j\frac{2\pi\alpha}{4}), \quad (2.26)$$

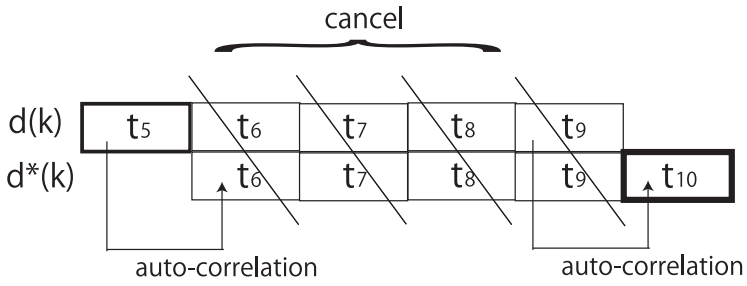

Figure 2.17: Cancelation in auto-correlation.

$$\rho''''[n] = -|\phi|^2 v^*[n-1]\{s_{SP}[n]\exp(j\frac{2\pi\alpha}{N}n) - s_{SP}[n-1]\exp(j\frac{2\pi\alpha}{N}(n-1))\}\exp(j\frac{2\pi\alpha}{4}). \tag{2.27}$$

Here,

$$\rho'[n] = \rho'''[n+\frac{N}{4}], \tag{2.28}$$

$$\rho''[n] = \rho''''[n+\frac{N}{4}]. \tag{2.29}$$

As a result, due to $\rho_5[n]$, the STSP symbols from t_6 to t_9 are canceled and only the following terms remains after the summation as shown in Fig. 2.17.

$$\begin{aligned}
&\sum_{n=N}^{\frac{9N}{4}-1}\rho_5[n] \\
=\ &\sum_{n=N}^{\frac{5N}{4}-1}[|\phi|^2 v^*[n]\{s_{SP}[n]\exp(j\frac{2\pi\alpha}{N}n) - s_{SP}[n-1]\exp(j\frac{2\pi\alpha}{N}(n-1))\}\exp(j\frac{2\pi\alpha}{4}) \\
&-|\phi|^2 v^*[n-1]\{s_{SP}[n]\exp(j\frac{2\pi\alpha}{N}n) - s_{SP}[n-1]\exp(j\frac{2\pi\alpha}{N}(n-1))\}\exp(j\frac{2\pi\alpha}{4})] \\
&+\sum_{n=2N}^{\frac{9N}{4}-1}[|\phi|^2 v[n+\frac{N}{4}]\{s^*_{SP}[n]\exp(-j\frac{2\pi\alpha}{N}n) - s^*_{SP}[n-1]\exp(-j\frac{2\pi\alpha}{N}(n-1))\} \\
&-|\phi|^2 v[n+\frac{N}{4}-1]\{s^*_{SP}[n]\exp(-j\frac{2\pi\alpha}{N}n) - s^*_{SP}[n-1]\exp(-j\frac{2\pi\alpha}{N}(n-1))\}].
\end{aligned} \tag{2.30}$$

Thus, Eq. (2.23) is approximated as

$$\sigma_v^2 = 4\cdot\frac{N}{4}\cdot E_d\cdot\frac{1}{2\cdot\mathrm{SNR}}, \tag{2.31}$$

where SNR $= E_s/\sigma_n^2$, $E_s = \mathrm{E}\{|s_{SP}[n]|^2\}$, and $E_d = \mathrm{E}\{|r_{SP}[n] - r_{SP}[n-1]|^2\}$. Here, it is assumed that

$$|\phi|^2 \approx 1, \tag{2.32}$$

and

$$|\sum_{n=N}^{\frac{9N}{4}-1}\{\rho_1[n] + \rho_2[n] + \rho_3[n] + \rho_4[n]\}| \gg |\sum_{n=N}^{\frac{9N}{4}-1}\rho_5[n]|. \tag{2.33}$$

With the above approximations, the MSE of frequency offset estimation is then obtained as

$$\begin{aligned} & \mathrm{E}\{|\hat{\alpha} - \alpha|^2\} \\ = \; & |\alpha - \frac{4}{2\pi}[\arg\{\sum_{n=N}^{\frac{9N}{4}-1}\rho_1[n] + \rho_2[n] + \rho_3[n] + \rho_4[n]\}]|^2 \\ & + \frac{\sigma_v^2}{\mathrm{E}\{|\sum_{n=N}^{\frac{9N}{4}-1}\rho_1[n] + \rho_2[n] + \rho_3[n] + \rho_4[n]|^2\}} \\ = \; & |\alpha - \frac{4}{2\pi}[\arg\{\sum_{n=N}^{\frac{9N}{4}-1}\rho_1[n] + \rho_2[n] + \rho_3[n] + \rho_4[n]\}]|^2 + \frac{2}{5 \cdot \mathrm{SNR}}. \end{aligned} \tag{2.34}$$

The normalized MSE of frequency offset estimation, $\mathrm{NMSE}\{\hat{\alpha}\}$, is given as

$$\mathrm{NMSE}\{\hat{\alpha}\} = \frac{E\{|\hat{\alpha} - \alpha|^2\}}{\alpha^2}. \tag{2.35}$$

2.2.4 Numerical Results

2.2.4.1 Simulation Conditions

The MSE of the frequency offset estimation is evaluated through computer simulation. The simulation conditions are shown in Table 2.2. Information bits are modulated with QPSK on each subcarrier. The number of DFT/IDFT points is set to 64 while 52 subcarriers are used for the LTSP symbols, which follows the IEEE802.11a/g standard. The 1st order butterworth filter is employed as the Rx HPF. The cutoff frequency of the received HPF is set to 10[kHz]. The normalized frequency offset is from 0.1 to 0.5. The mismatch of the amplitude is set at a range of 0.01 to 0.05 and the mismatch of the phase is set at a range of 1 to 5[degrees] [2.21].

Table 2.2: Simulation conditions.

Trial number	10,000 times
Modulation scheme	QPSK+OFDM
Number of subcarrier	64
Number of data subcarrier	52
Channel	AWGN
Rx HPF	1st order Butterworth filter f_B=10[kHz]
Normalized frequency offset	0.1-0.5
Gain mismatch β	0.01-0.05
Phase mismatch θ	1-5 [degrees]

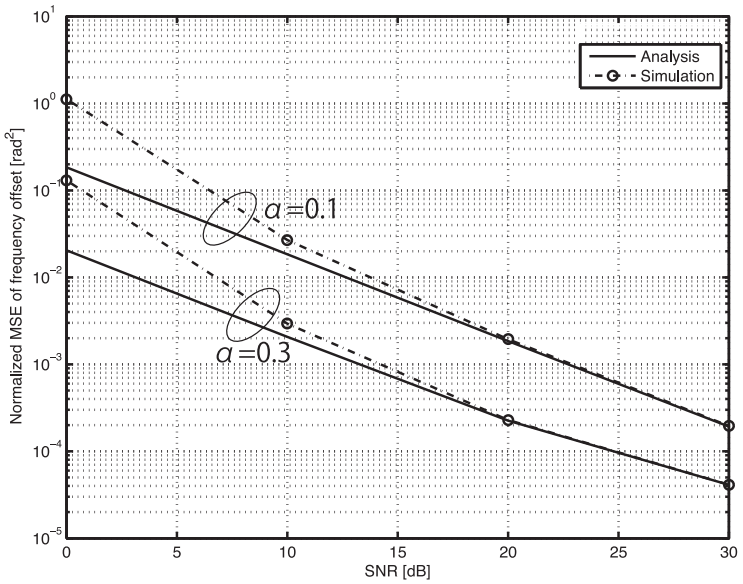

Figure 2.18: MSE vs. SNR (β=0.05, θ=5[degrees]).

2.2.4.2 MSE Performance of Frequency Offset Estimation under IQ imbalance

Fig. 2.18 shows the relationship between the MSE performance and the SNR. Here, the gain mismatch is set to 0.05, the phase mismatch is set to 5[degrees]. The MSE curves for the theoretical analysis is close to the numerical results obtained through computer simulation when the SNR is more than 10[dB]. The difference between the analysis and simulation is due to the noise components in Eq. (2.15) that are neglected in the MSE derivation.

Fig. 2.19 shows the MSE performance of frequency offset estimation when the

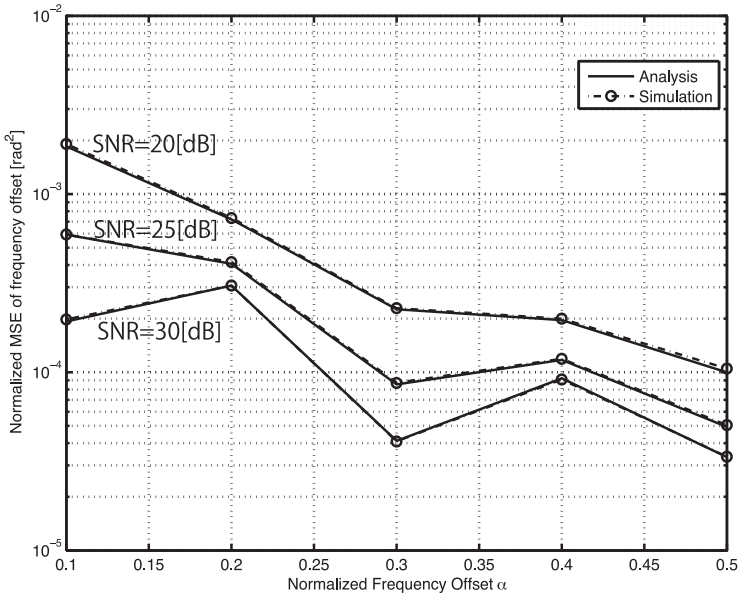

Figure 2.19: MSE vs. normalized frequency offset (θ=5[degrees], β=0.05).

normalized frequency offset is varied. It is assumed that the gain mismatch β is 0.05, the phase mismatch θ is 5[degrees], and the SNR is 20, 25, and 30[dB]. The MSE curves for the theoretical analysis are very close to the simulated curves. It can be seen from Fig. 2.19 that the normalized MSE performance improves as the frequency offset increases. The dependency of the MSE on the normalized frequency offset is due to the amount of the residual distortion caused by IQ imbalance after the sum of the auto-correlation samples in Eq. (2.21). The distortion changes according to the waveform of the preamble symbols with frequency offset as shown in Eq. (2.15). This fluctuation is observed without thermal noise (SNR $= \infty$).

Fig. 2.20 shows the MSE performance vs. gain mismatch. Here, the normalized frequency offset is set to 0.3, the phase mismatch is set to 5[degrees], and the SNR is 20, 25, and 30[dB]. The MSE curves for the theoretical analysis are very close to the ones obtained through computer simulation. As the gain mismatch increases, the MSE performance of frequency offset estimation is deteriorated.

Fig. 2.21 shows the MSE performance vs. phase mismatch. Here, the normalized frequency offset is set to 0.3, the gain mismatch is set to 0.05, and the SNR is 20, 25, and 30[dB]. Again, the MSE curves for the theoretical analysis are very close to the ones for the computer simulation. As the phase mismatch increases, the MSE increases.

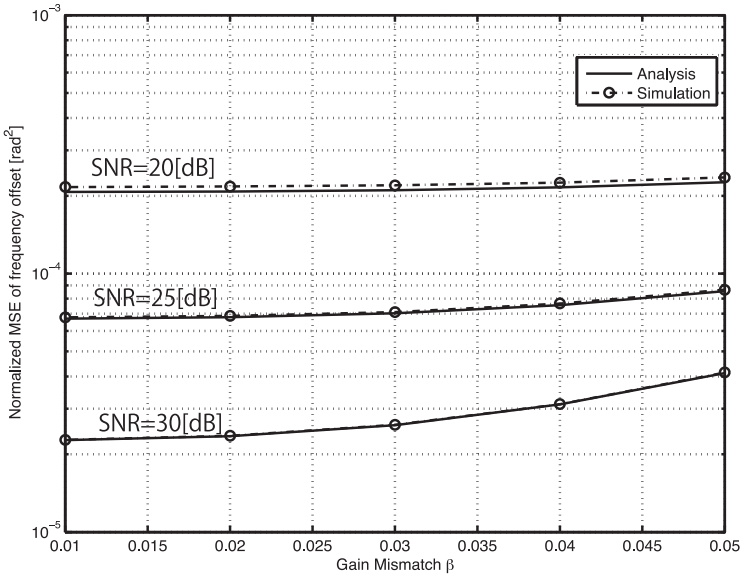

Figure 2.20: MSE vs. gain mismatch (normalized freq. offset=0.3, θ=5[degrees]).

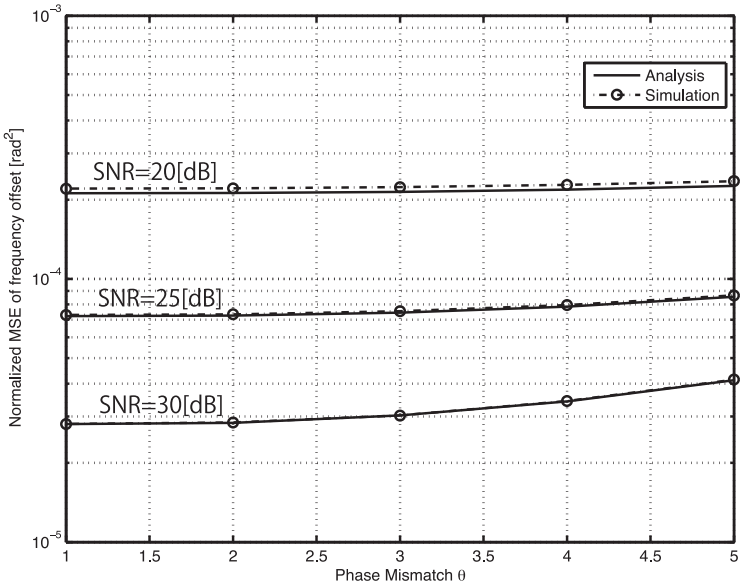

Figure 2.21: MSE vs. phase mismatch (normalized freq. offset=0.3, β=0.05).

2.2.5 Conclusions

In this section, the performance of the frequency offset estimation with the differential filter in the presence of IQ imbalance has been analyzed. Frequency offset is

estimated through the auto-correlation of the preamble symbols that goes through the differential filter. IQ imbalance deteriorates the accuracy of the frequency offset estimation scheme. The theoretical curves matches the numerical results obtained through the computer simulation when the SNR is more than 10[dB]. It has been shown that the MSE varies according to the amount of frequency offset. This is due to the residual distortion of the auto-correlation caused by IQ imbalance and it depends on the waveform of the preamble symbols.

2.3 Time Domain IQ Imbalance Estimation Scheme in the Presence of Frequency Offset and Time-varying DC Offset for Direct Conversion Receivers

A direct conversion architecture reduces the cost and power consumption of a receiver. However, the direct conversion receiver may suffer from DC offset, frequency offset, and IQ imbalance. This section presents a time domain IQ imbalance estimation scheme for OFDM direct conversion receivers. The proposed IQ imbalance estimation scheme operates in the presence of the time-varying DC offset and the frequency offset. The proposed scheme calculates the IQ imbalance from a simple equation. It employs the knowledge of the preamble symbols of the IEEE 802.11 a/g standards while it does not require the impulse response of the channel.

2.3.1 Introduction

In IEEE 802.11a/g, the high data rate transmission is realized because an OFDM modulation scheme is used as the 2nd modulation. At the receiving end, a direct conversion architecture has been implemented, which reduces the cost and power consumption of the receiver. However, as mentioned in Chapter 1, OFDM direct conversion receivers may suffer from the DC offset, the frequency offset, and the IQ imbalance [2.1]-[2.22]. These distortions deteriorate the quality of the demodulated signal. They should be compensated within the received frame since the amount of mismatch depends on the transmitter.

Several joint compensation schemes have been presented [2.23]-[2.21]. In [2.23], the frequency offset and the IQ imbalance are estimated using a nonlinear least-squares scheme. This scheme requires the covariance matrix of the received samples. In [2.4], the IQ imbalance as well as the frequency offset and the DC offset are estimated using the maximum likelihood criterion. Although this scheme achieves a performance close to the Cramer-Rao bound, it requires a large amount of com-

putation and channel response. In [2.24], a frequency offset and IQ imbalance estimation scheme is proposed on the basis of simple calculation. The scheme in [2.21] carries out frequency offset and IQ imbalance estimation in the time domain. However, these schemes assume the absence of DC offset. Blind estimation and compensation schemes in the time domain have also been proposed [2.25]-[2.27]. Although the amount of computation for each iteration of the adaptive processes is relatively small, these schemes do not assume the time-varying DC offset. If the time-varying DC offset is present, the convergence time may exceed the duration of the short preamble.

The level of DC offset varies due to the gain switching in the LNA. However, none of the above studies take into account the time-varying DC offset, frequency offset, and IQ imbalance at the same time.

In this section, a novel time domain IQ imbalance estimation scheme is investigated allowing for the time-varying DC offset and the frequency offset. In the proposed scheme, the differential filter is employed to remove the time-varying DC offset. In previous sections, it has been shown that the differential filter effectively estimates the frequency offset in the presence of the time-varying DC offset [2.19]-[2.29]. In the proposed scheme, from the output of the differential filter, the IQ imbalance as well as the frequency offset is estimated from a simple equation. The proposed scheme employs the knowledge of the preamble symbols of the IEEfE 802.11a/g standards, while it does not require the impulse response of the channel. Therefore, this scheme is suitable for low-cost and low-power-consumption receivers.

This section is organized as follows. Subsection 2.3.2 gives the system model and the IQ imbalance model. In subsection 2.3.3, the frequency offset estimation using the differential filter is explained. Subsection 2.3.4 describes the proposed IQ imbalance estimation. In subsection 2.3.5 numerical results obtained through computer simulation are presented. Subsection 2.3.6 gives our conclusions.

2.3.2 System Model

In this section, the IQ imbalance estimation is employed on the training sequence of IEEE 802.11a/g [2.8][2.9]. To maintain the received signal amplitude at a suitable fixed level, the AGC is used. In a WLAN receiver, the AGC controls the receiver gain in the middle of the STSP. In the 802.11a/g standards, gain control of more than 50dB is required [2.6]. The assumed RF architecture in this section is shown in Fig. 2.23. As shown in the figure, gain control is applied in both the LNA and the VGAs. Here, an LNA with two gain modes is assumed [2.7]-[2.14]. This type

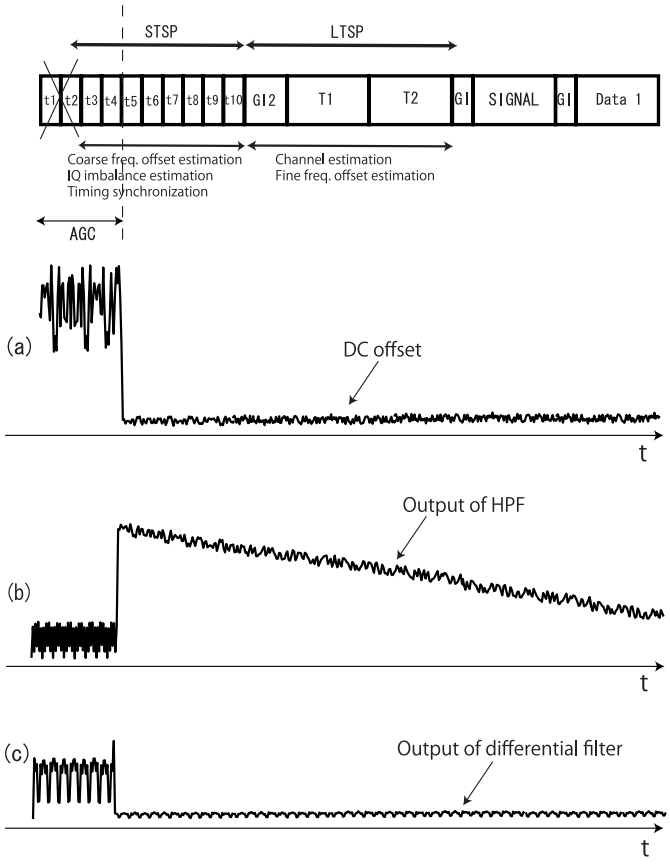

Figure 2.22: DC offset and the output of differential filter.

of LNA has been discussed in [2.7] and [2.11]. The VGAs at baseband compensate the rest of the required gain.

In the direct conversion receiver, the DC offset may be eliminated by the HPFs, as shown in Fig. 2.23 [2.1][2.7]. However, as the gain of the LNA changes, the DC offset level varies [2.12]. Figures 2.22 (a), (b), and (c) show the received signal (absolute value) of the training sequence preamble when the gain of the LNA is changed. At the beginning of the STSP, the gain of the LNA is set to the maximum because the power of the received signal is unknown to the receiver. If the power of the received signal is sufficiently large, the LNA is switched to the low-gain mode between t_4 and t_5. The DC offset level then decreases rapidly and the fluctuating DC offset level is input into the HPF. Here, the fluctuation of the DC offset level is modeled as a two-step function as shown in Fig. 2.22 (a) [2.12]. The transient response of the HPF due to the fluctuation of the DC offset level appears at

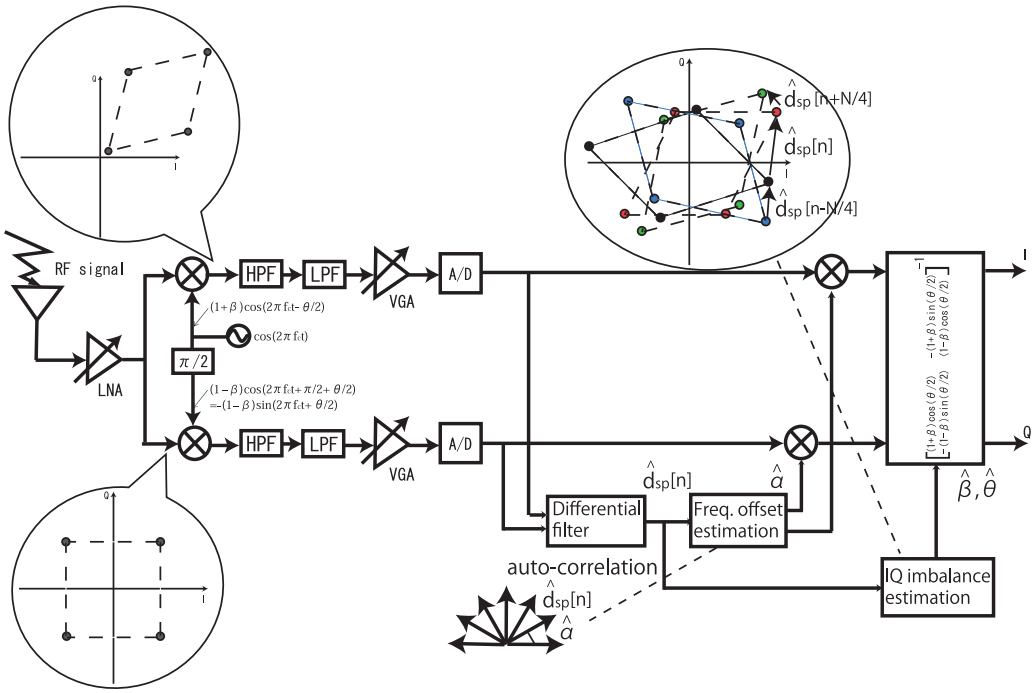

Figure 2.23: Receiver architecture.

the output of the HPF as shown in Fig. 2.22 (b). The component deteriorates the accuracy of frequency offset estimation and IQ imbalance estimation. In the proposed scheme, the transient response is removed using the differential filter. The cutoff frequency of the HPF is set to a relatively low value so as not to eliminate the data subcarriers adjacent to the DC subcarrier in the data period. Since the cutoff frequency of the HPF is low, the transient response decreases gradually. Thus, the differential filter can suppress the effect of the residual DC offset as shown in Fig. 2.22 (c).

2.3.3 Frequency Offset Estimation

2.3.3.1 Frequency Offset, DC Offset, and IQ Imbalance Model

In order to clarify the signal model with the frequency offset, the DC offset, and the IQ imbalance, the following explanation omits the noise term, $v[k]$, in Eq. (1.1) for simplicity. From Eq. (1.5) in Chapter 1, the received signal with the IQ imbalance in the time domain is given as

$$\hat{r}[n] = \phi r[n] + \psi^* r^*[n] + \delta[n], \tag{2.36}$$

where

$$\phi = \cos(\frac{\theta}{2}) + j\beta \sin(\frac{\theta}{2}), \tag{2.37}$$

$$\psi = \beta \cos(\frac{\theta}{2}) + j \sin(\frac{\theta}{2}), \tag{2.38}$$

and $\delta[n]$ is the DC offset that occurs at the mixer.

The frequency offset is estimated in the presence of the time-varying DC offset and the IQ imbalance. After coarse estimation, the LTSP symbols are used for channel estimation for each subcarrier.

2.3.3.2 Frequency Offset Estimation Using Differential Filter

In this frequency offset estimation scheme, the received signal with IQ imbalance is substituted into the differential filter used to eliminate the residual DC offset that passes through the HPF. The n-th output $\hat{d}_{SP}[n]$ after the differential filter is

$$\begin{aligned} \hat{d}_{SP}[n] &= \hat{r}_{SP}[n] - \hat{r}_{SP}[n-1] \\ &= \phi\{r_{SP}[n] - r_{SP}[n-1]\} + \psi^*\{r^*_{SP}[n] - r^*_{SP}[n-1]\} + \Delta\delta[n, n-1],\ n \geq 1, \end{aligned} \tag{2.39}$$

where

$$\hat{r}_{SP}[n] = \phi r_{SP}[n] + \psi^* r^*_{SP}[n], \tag{2.40}$$

$r_{SP}[n]$ is the n-th signal with the frequency offset in the STSP period, and $\Delta\delta[n, n-1]$ is the difference between the n-th and $[n-1]$-th residual DC offsets. In the STSP, a short preamble with a period of $N/4$ samples is repeated 10 times. From Eq. (2.39), the autocorrelation value for frequency offset estimation with the DC offset

and the IQ imbalance is given by

$$\begin{aligned}
& \hat{d}^*_{SP}[n]\hat{d}_{SP}[n+\frac{N}{4}] \\
= \; & |\phi|^2|r_{SP}[n+\frac{N}{4}]-r_{SP}[n+\frac{N}{4}-1]|^2\exp(j\frac{2\pi\alpha}{4}) && \text{(2.41a)} \\
& +\phi^*\psi^*(r_{SP}[n+\frac{N}{4}]-r_{SP}[n+\frac{N}{4}-1])^2\exp(-j\frac{2\pi\alpha}{4}) && \text{(2.41b)} \\
& +\phi\psi(r_{SP}[n+\frac{N}{4}]-r_{SP}[n+\frac{N}{4}-1])^2\exp(j\frac{2\pi\alpha}{4}) && \text{(2.41c)} \\
& +|\psi|^2|r_{SP}[n+\frac{N}{4}]-r_{SP}[n+\frac{N}{4}-1]|^2\exp(-j\frac{2\pi\alpha}{4}) && \text{(2.41d)} \\
& +O(\Delta\delta[n+\frac{N}{4},n+\frac{N}{4}-1],\Delta\delta[n,n-1]). && \text{(2.41e)}
\end{aligned}$$

Here, $O(\Delta\delta[n+\frac{N}{4},n+\frac{N}{4}-1],\Delta\delta[n,n-1])$ is the product of $\Delta\delta[n+\frac{N}{4},n+\frac{N}{4}-1]$ and $\Delta\delta[n,n-1]^*$, N is the number of samples, and α is the normalized frequency offset in one OFDM symbol period. By averaging over 10 STSP symbols, the normalized frequency offset α is estimated from the first term (2.41a). The additional MSE in frequency offset estimation due to the IQ imbalance is caused by the terms given in (2.41b), (2.41c), and (2.41d). However, it is less than 10^{-3} of the square of the frequency offset [2.29]. Thus, the IQ imbalance is neglected at this stage for estimation of the frequency offset.

2.3.4 IQ Imbalance Estimation

2.3.4.1 IQ Imbalance Estimation

The IQ imbalance is also estimated from the outputs of the differential filter. From Eq. (2.39), the 3 preamble symbols repeated in $N/4$ samples in the STSP can be expressed as

$$\begin{aligned}
\hat{d}_{SP}[n-\frac{N}{4}] &= \hat{r}_{SP}[n-\frac{N}{4}]-\hat{r}_{SP}[n-\frac{N}{4}-1] \\
&= \phi\{r_{SP}[n]-r_{SP}[n-1]\}\exp(-j\frac{2\pi\alpha}{4}) \\
&\quad +\psi^*\{r^*_{SP}[n]-r^*_{SP}[n-1]\}\exp(j\frac{2\pi\alpha}{4}) \\
&= \phi d_{SP}[n]\gamma^{-1}+\psi^* d^*{}_{SP}[n]\gamma, && \text{(2.42)}
\end{aligned}$$

$$\begin{aligned}\hat{d}_{SP}[n] &= \hat{r}_{SP}[n] - \hat{r}_{SP}[n-1] \\ &= \phi\{r_{SP}[n] - r_{SP}[n-1]\} + \psi^*\{r^*_{SP}[n] - r^*_{SP}[n-1]\} \\ &= \phi d_{SP}[n] + \psi^* d^*{}_{SP}[n], \end{aligned} \tag{2.43}$$

$$\begin{aligned}\hat{d}_{SP}[n+\frac{N}{4}] &= \hat{r}_{SP}[n+\frac{N}{4}] - \hat{r}_{SP}[n+\frac{N}{4}-1] \\ &= \phi\{r_{SP}[n+\frac{N}{4}] - r_{SP}[n+\frac{N}{4}-1]\} \\ &\quad + \psi^*\{r^*_{SP}[n+\frac{N}{4}] - r^*_{SP}[n+\frac{N}{4}-1]\} \\ &= \phi\{r_{SP}[n] - r_{SP}[n-1]\}\exp(j\frac{2\pi\alpha}{4}) \\ &\quad + \psi^*\{r^*_{SP}[n] - r^*_{SP}[n-1]\}\exp(-j\frac{2\pi\alpha}{4}) \\ &= \phi d_{SP}[n]\gamma + \psi^* d^*{}_{SP}[n]\gamma^{-1}. \end{aligned} \tag{2.44}$$

Here,

$$d_{SP}[n] = r_{SP}[n] - r_{SP}[n-1], \tag{2.45}$$

$$\gamma = \exp(j\frac{2\pi\alpha}{4}). \tag{2.46}$$

Solving Eqs. (2.42), (2.43), and (2.44) as simultaneous equations, the following equation is derived.

$$\frac{\hat{d}_{SP}[n-\frac{N}{4}] - \hat{d}_{SP}[n]\gamma^{-1}}{(\hat{d}_{SP}[n]\gamma^{-1} - \hat{d}_{SP}[n+\frac{N}{4}])^*} = \frac{\psi^*}{\phi^*} = \varepsilon. \tag{2.47}$$

Here, with the assumption of small θ, ϕ and ψ are approximated as

$$\phi = \cos(\frac{\theta}{2}) + j\beta\sin(\frac{\theta}{2}) \approx 1 + j\beta\frac{\theta}{2}, \tag{2.48}$$

$$\psi = \beta\cos(\frac{\theta}{2}) + j\sin(\frac{\theta}{2}) \approx \beta + j\frac{\theta}{2}, \tag{2.49}$$

using the first-order approximation of the Taylor expansion. Thus, Eq. (2.47) becomes

$$\frac{\beta - j\frac{\theta}{2}}{1 - j\beta\frac{\theta}{2}} \approx \varepsilon_I + j\varepsilon_Q. \tag{2.50}$$

$\hat{\beta}$ and $\hat{\theta}$ can then be calculated as follows.

$$\hat{\beta} \approx \frac{2\varepsilon_I}{2 - \varepsilon_Q\theta}, \tag{2.51}$$

$$\hat{\theta} \approx \frac{-(\varepsilon_I^2 + \varepsilon_Q^2 - 1) - \sqrt{(\varepsilon_I^2 + \varepsilon_Q^2 - 1)^2 + 4\varepsilon_Q^2}}{\varepsilon_Q}. \tag{2.52}$$

To obtain ε in Eq. (2.47), α in Eq. (2.46) is substituted with the value estimated in Section 2.3.3.

In terms of complexity, the estimation of ε requires the following number of calculations;

$$C_\varepsilon = N_{sp} \times [2 \cdot C_{add} + 1 \cdot C_{mult}] + 1 \cdot C_{div}, \tag{2.53}$$

where C_{add}, C_{mult}, and C_{div} are the numbers of complex additions, multiplications, and divisions, respectively, and N_{sp} represents the number of samples in the STSP. The complexity is almost equivalent to the conventional scheme in [2.21].

Note that, similar to [2.21], the proposed scheme works well if α is more than 0.1. This can be understood by taking the noise term into consideration in Eq. (2.47). If the noise is included, the left side of Eq. (2.47) turns to

$$\frac{\psi^*\{s_{SP}^*[n]\exp(-j\frac{2\pi\alpha}{N}n) - s_{SP}^*[n-1]\exp(-j\frac{2\pi\alpha}{N}[n-1])\}(\gamma-\gamma^{-1}) + O(\phi,\psi,\gamma^{-1},v[n-\frac{N}{4}-1],v[n-\frac{N}{4}],v[n-1],v[n])}{\phi^*\{s_{SP}^*[n]\exp(-j\frac{2\pi\alpha}{N}n) - s_{SP}^*[n-1]\exp(-j\frac{2\pi\alpha}{N}[n-1])\}(\gamma-\gamma^{-1}) + O(\phi,\psi,\gamma,v[n-1],v[n],v[n+\frac{N}{4}-1],v[n+\frac{N}{4}])}. \tag{2.54}$$

Here, $O(\phi, \psi, \gamma^{-1}, v[n-\frac{N}{4}-1], v[n-\frac{N}{4}], v[n-1], v[n])$ is the product of ϕ, ψ, γ^{-1}, $v[n-\frac{N}{4}-1]$, $v[n-\frac{N}{4}]$, $v[n-1]$, $v[n]$. $O(\phi, \psi, \gamma, v[n-1], v[n], v[n+\frac{N}{4}-1], v[n+\frac{N}{4}])$ is also the product of ϕ, ψ, γ, $v[n-1]$, $v[n]$, $v[n+\frac{N}{4}-1]$, $v[n+\frac{N}{4}]$. If the frequency offset α is small, the term $(\gamma - \gamma^{-1})$ approaches 0. The left side of Eq. (2.47) is then approximated as

$$\begin{aligned} & \frac{\hat{d}_{SP}[n-\frac{N}{4}] - \hat{d}_{SP}[n]\gamma^{-1}}{(\hat{d}_{SP}[n]\gamma^{-1} - \hat{d}_{SP}[n+\frac{N}{4}])^*} \\ \approx\ & \frac{O(\phi,\psi,\gamma,v[n-\frac{N}{4}-1],v[n-\frac{N}{4}],v[n-1],v[n])}{O(\phi,\psi,\gamma,v[n-1],v[n],v[n+\frac{N}{4}-1],v[n+\frac{N}{4}])}. \end{aligned} \tag{2.55}$$

Thus, the estimation of IQ imbalance becomes inaccurate. In this case, the time difference among the outputs of the differential filter in Eqs. (2.42), (2.43), and (2.44) should be set to longer than $N/4$. The effective frequency offset then increases although the number of samples required to calculate Eq. (2.47) decreases.

2.3.4.2 IQ Imbalance Compensation

In the LTSP and the following data period, IQ imbalance is compensated on the basis of the phase mismatch and gain mismatch estimated in the STSP. By con-

Table 2.3: Simulation conditions.

Number of trials	10,000 times
Modulation scheme	Preamble: QPSK+OFDM Data: 64QAM+OFDM
Number of subcarriers	64
Number of data subcarriers	52
Channel	AWGN
Rx HPF	1st-order Butterworth filter f_c=10[kHz]
Normalized DC offset	35/15[dB]
Normalized frequency offset α	0.3
Gain mismatch β	0.01-0.05
Phase mismatch θ	0-5 [degrees]

solidating Eqs. (1.7) and (1.8) into a system of equations, we arrive at

$$\begin{aligned} \begin{bmatrix} \hat{r}_{d_I} \\ \hat{r}_{d_Q} \end{bmatrix} &= \begin{bmatrix} (1+\beta)\cos(\frac{\theta}{2}) & -(1+\beta)\sin(\frac{\theta}{2}) \\ -(1-\beta)\sin(\frac{\theta}{2}) & (1-\beta)\cos(\frac{\theta}{2}) \end{bmatrix} \begin{bmatrix} r_{d_I} \\ r_{d_Q} \end{bmatrix} \\ &= \mathbf{\Omega} \begin{bmatrix} r_{d_I} \\ r_{d_Q} \end{bmatrix}, \end{aligned} \tag{2.56}$$

where $\hat{r}_{d_I}$, $\hat{r}_{d_Q}$, r_{d_I}, and r_{d_Q} are the I and Q components of the received signal with and without IQ imbalance, respectively. The IQ imbalance is compensated using $\mathbf{\Omega}^{-1}$.

2.3.5 Simulation Results

2.3.5.1 Simulation Conditions

The MSE of the IQ imbalance estimation is evaluated through computer simulation. The simulation conditions are shown in Table 2.3. The number of trials is 10,000 times. Information bits are modulated with QPSK in the preamble period and 64 quadrature amplitude modulation (QAM) in the data period on each subcarrier. The number of DFT/IDFT points is set to 64, while 48 subcarriers are used for the data subcarriers and 4 subcarriers are used for the pilot subcarriers, which follows the IEEE 802.11a/g standards. As a channel model, AWGN channel is assumed. A 1st-order Butterworth filter is employed as the HPF. The cutoff frequency of the HPF is set to 10[kHz]. The normalized frequency offset, α, is 0.3. The gain mismatch is set from 0.01 to 0.05 and the phase mismatch is varied from 0 to 5[degrees] [2.21].

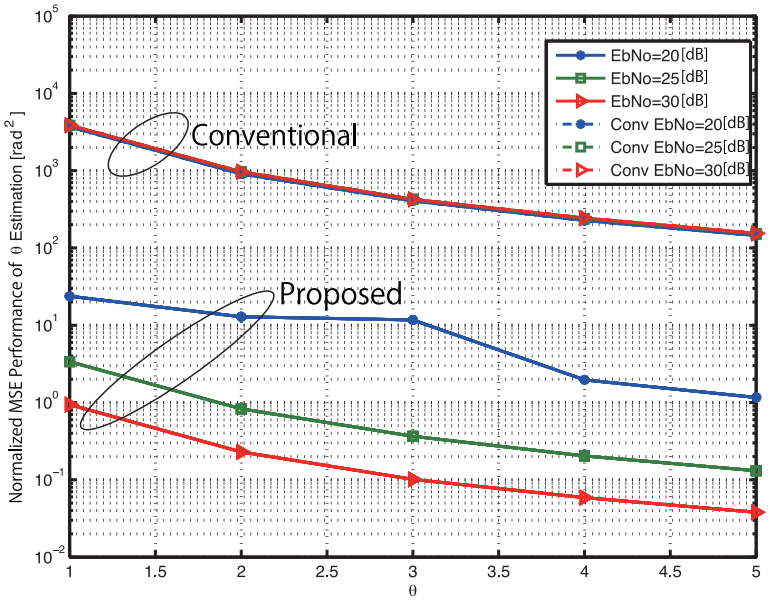

Figure 2.24: Normalized MSE performance of phase mismatch estimation vs. phase mismatch (β=0.05, normalized freq. offset = 0.3).

The gain of the LNA can be selected between 35 and 15[dB] [2.15]. The isolation between the LO output and the LNA input is assumed to be -60[dB]. Therefore, if the power of the LO signal is set to 0[dBm], the DC offset level is -25/-45[dBm].

On the other hand, the received signal power is set to -53[dBm], which is equivalent to -70[dBm] on each subcarrier in the LTSP. In this case, the DC offset is 10[dB] larger than the signal power on each subcarrier.

2.3.5.2 Normalized MSE Performance of Phase Mismatch Estimation vs. Phase Mismatch

Figure 2.24 shows the normalized MSE performance of phase mismatch estimation. In this figure, 'Conventional' refers to the IQ imbalance estimation scheme in the time domain presented in [2.21]. The gain mismatch β is set to 0.05 and the normalized frequency offset α is set to 0.3. In Fig. 2.24, the proposed scheme has better estimation performance.The reason for this is that the conventional scheme suffers from the residual DC offset. In this figure, the MSE improves as the phase mismatch increases. This is because the MSE is normalized by the mismatch θ. Furthermore, the normalized MSE performance improves as E_b/N_0 increases

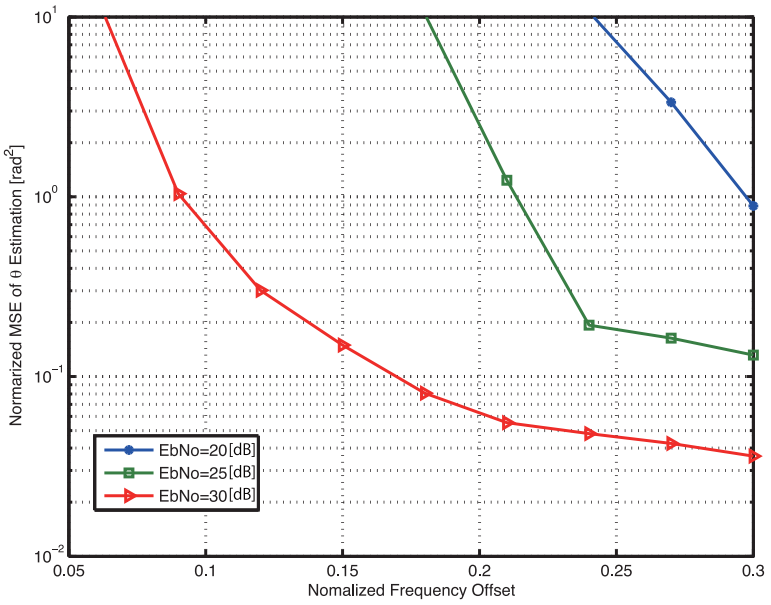

Figure 2.25: Normalized MSE performance of phase mismatch estimation vs. frequency offset (β=0.05, θ= 5[degrees]).

from 20 to 25[dB]. The normalized MSE of the phase mismatch θ fluctuates when E_b/N_0=20[dB]. This is because Eq. (2.52) has ε_Q in the denominator. If the estimated value of ε_Q approaches 0 due to noise, the MSE of the phase mismatch, θ, increases. This case rarely happens and does not change the average BER.

2.3.5.3 Normalized MSE Performance of Phase Mismatch Estimation vs. Frequency Offset

Figure 2.25 shows the normalized MSE performance of phase mismatch estimation with time-varying DC offset and frequency offset when the frequency offset is varied. The gain mismatch β is set to 0.05 and the phase mismatch θ is set to 5[degrees]. E_b/N_0 in the LTSP is set to {20, 25, or 30}[dB].

It is clear from Fig. 2.25 that the normalized MSE performance increases as the frequency offset reduces. This is because the term $(\gamma - \gamma^{-1})$ in Eq. (2.54) approaches 0 as mentioned in Section 2.3.4.1.

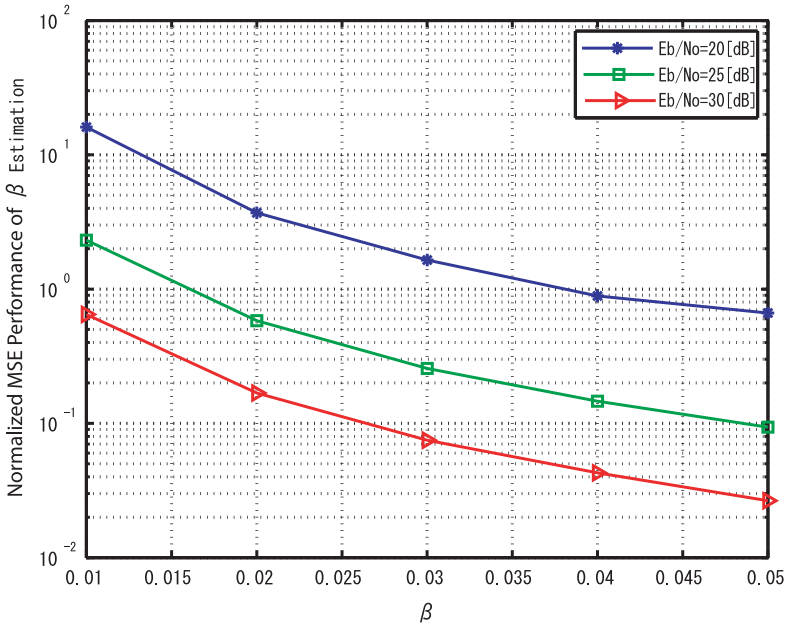

Figure 2.26: Normalized MSE performance of gain mismatch estimation (θ= 5[degrees], normalized freq. offset=0.3).

2.3.5.4 Normalized MSE Performance of Gain Mismatch Estimation

Figure 2.26 shows the normalized MSE performance of the gain mismatch estimation with the time-varying DC offset and frequency offset when the gain mismatch value is varied. The phase mismatch θ is set to 5[degrees] and the normalized frequency offset α is set to 0.3. E_b/N_0 in the LTSP is set to {20, 25, or 30}[dB].

It can be seen from Fig. 2.26 that the normalized MSE performance improves as the gain mismatch increases. This is because the MSE is normalized by the gain mismatch β. As E_b/N_0 increases to 10[dB], the normalized MSE is reduced by a factor of about 10.

2.3.5.5 BER Performance

The BER performance versus E_b/N_0 in the AWGN channel is shown in Fig. 2.27. The simulation conditions are the same as those with the static DC offset. From Fig. 2.27, it can be concluded that the performance degradation due to the proposed scheme is about 4[dB]. This plot is simulated using 1st order interpolation for phase compensation using pilot subcarriers. 125 OFDM symbols are transmit-

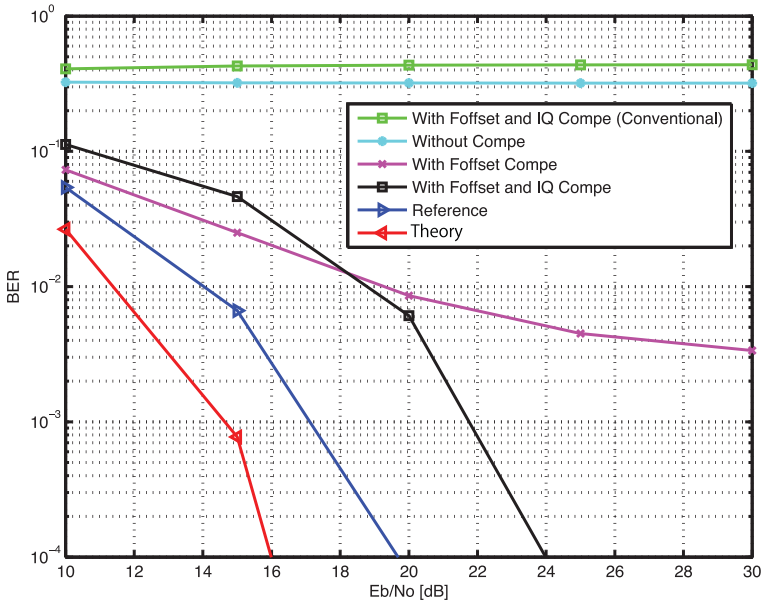

Figure 2.27: BER performance with 1st order interpolation (normalized freq. offset=0.3, β=0.05, θ=5[degrees]).

ted for each packet and 64QAM is assumed. The number of DFT/IDFT points is set to 64. The OFDM receiver is considered with normalized frequency offset $\alpha = 0.3$, gain imbalance $\beta = 0.05$, and phase mismatch $\theta = 5$[degrees].

'With Foffset and IQ Compe (Conventional)' refers to the case with frequency offset compensation and the IQ imbalance compensation presented in [2.21]. 'Without Compe' represents the simulation in the case of no frequency offset compensation or IQ imbalance compensation, 'With Foffset Compe' refers to frequency offset compensation, and 'With Foffset and IQ Compe' refers to the case of frequency offset compensation and IQ imbalance compensation. In addition, 'Reference' represents the simulation when phase compensation by pilot subcarriers is carried out under the frequency offset and the IQ imbalance. In each OFDM symbol, following the IEEE 802.11 a/g standards, 4 pilot subcarriers are inserted. 'Theory' is the theoretical BER curve for 64QAM.

As shown in this figure, the proposed scheme exhibits superior estimation performance since the conventional scheme suffers from the residual DC offset. Moreover, neither frequency offset compensation nor IQ imbalance compensation degrades the performance significantly. Comparing the proposed scheme with theoretical

results, there is a difference of 8[dB], in which 4[dB] of the difference is due to nonideal channel equalization by the pilot subcarriers. Thus, the BER using the proposed IQ imbalance estimation scheme exhibits about 4[dB] degradation with the large DC offset, the frequency offset, and the IQ imbalance. However, our proposed scheme has less complexity than existing algorithms.

2.3.6 Conclusions

The direct conversion receiver has disadvantages such as the DC offset, the frequency offset, and the IQ imbalance. In this section, a low-complexity IQ imbalance estimation scheme allowing for the time-varying DC offset and the frequency offset has been proposed. The IQ imbalance is calculated using a simple equation without requiring the impulse response of the channel. Therefore, the proposed scheme is suitable for low-cost and low-power-consumption terminals. Computer simulations show that the BER performance using the proposed IQ imbalance estimation scheme is satisfactory when E_b/N_0 is more than 20[dB], in which 64QAM is used for the 1st modulation. The system exhibits degradation of about 4[dB] with the large time-varying DC offset, the frequency offset, and the IQ imbalance.

2.4 Frequency Domain IQ Imbalance Estimation Scheme in the Presence of DC Offset and Frequency Offset

The direct conversion receivers in OFDM systems suffer from DC offset, frequency offset, and IQ imbalance. We have proposed the IQ imbalance estimation scheme in the presence of DC offset and frequency offset, which uses the preamble signals in the time domain as mentioned in Section 2.3. In this scheme, the DC offset is eliminated by the differential filter. However, the accuracy of IQ imbalance estimation is deteriorated when the frequency offset is small. To overcome this problem, a new IQ imbalance estimation scheme in the frequency domain has been proposed in this chapter. The IQ imbalance is estimated with pilot subcarriers. Numerical results obtained through computer simulation show that estimation accuracy and BER performance can be improved even if the frequency offset is small.

2.4.1 Introduction

As mentioned in Chapter 1, OFDM direct conversion receivers may suffer from the DC offset, the frequency offset, and the IQ imbalance [2.1][2.2]. These distortions

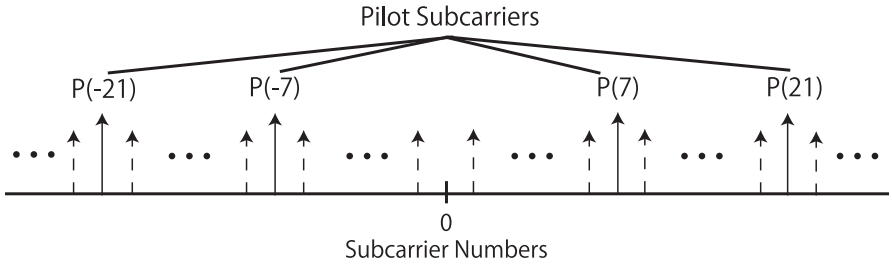

Figure 2.28: Subcarrier frequency allocation.

deteriorate the quality of the demodulated signal.

In Section 2.2, the IQ imbalance is estimated in the presence of the DC offset and frequency offset [2.30]. From the output of the differential filter, the IQ imbalance is estimated from a simple equation in the time domain. However, the estimation accuracy of the IQ imbalance is significantly deteriorated when the frequency offset is small. Therefore, a novel IQ imbalance estimation scheme in the frequency domain is investigated in this section. The proposed scheme uses a specific combination of symbols on symmetric pilot subcarriers. It works well if the frequency offset is relatively small.

This section is organized as follows. Subection 2.4.2 gives the system model and subsection 2.4.4 describes the proposed IQ imbalance model. In subsection 2.4.3, the frequency offset estimation using the differential filter is explained. Subsection 2.4.4 describes the proposed IQ imbalance estimation. In subsection 2.4.5, numerical results obtained through computer simulation are presented. Subsection 2.4.6 gives our conclusions.

2.4.2 System Model

In IEEE 802.11a/g, four subcarriers in one OFDM symbol during a data period are dedicated to pilot symbols [2.8][2.9]. These pilot symbols are transmitted on the subcarrier numbers of -21, -7, 7, 21 as shown in Fig. 2.28. Moreover, in IEEE 802.11a/g, the DC subcarrier is not used to avoid interference from the DC offset. Although the subcarriers do not interfere with one another, if frequency offset exists, the orthogonality between the subcarriers and the DC offset is deteriorated. A HPF can be used to eliminate the static DC offset without removing the received signal.

2.4.3 Frequency Offset Estimation Using Differential Filter

In this frequency offset estimation scheme, the received signal with IQ imbalance is substituted into the differential filter used to eliminate the residual DC offset that passes through the HPF. The n-th output, $\hat{d}_{SP}[n]$, after the differential filter is

$$\begin{aligned}\hat{d}_{SP}[n] &= \hat{r}_{SP}[n] - \hat{r}_{SP}[n-1] \\ &= \phi\{r_{SP}[n] - r_{SP}[n-1]\} + \psi^*\{r^*_{SP}[n] - r^*_{SP}[n-1]\} + \Delta\delta[n, n-1],\ n \geq 1,\end{aligned} \tag{2.57}$$

where

$$\hat{r}_{SP}[n] = \phi r_{SP}[n] + \psi^* r^*_{SP}[n], \tag{2.58}$$

$r_{SP}[n]$ is the n-th signal with the frequency offset in the STSP period, and $\Delta\delta[n, n-1]$ is the difference between the n-th and $[n-1]$-th residual DC offsets. In IEEE 802.11a/g standards, the coarse frequency offset estimation is carried out in STSP and the fine frequency offset estimation is carried out in LTSP [2.8][2.9]. In this section, the frequency offset estimation is calculated from auto-correlation value of STSP and LTSP received signals with IQ imbalance and frequency offset. From Eq. (2.21), the estimated frequency offset with STSP, $\hat{\alpha}'$, is given as

$$\hat{\alpha}' = \frac{4}{2\pi} \arg\{ \sum_{n=N}^{\frac{9N}{4}-1} \hat{d}^*_{SP}[n] \hat{d}_{SP}[n + \frac{N}{4}]\}, \tag{2.59}$$

where $n = N$ corresponds to the time index of the first symbol of t_5 and $n = \frac{9N}{4} - 1$ corresponds to the time index of the last symbol of t_9. Here, the STSP symbols from t_5 to t_{10} are used for frequency offset estimation. The auto-correlations between t_1 and t_4 are not used because of passible gain shift of the LNA [2.28]. The coarse frequency offset value obtained from STSP is used for compensation in LTSP. The estimated frequency offset with LTSP, $\hat{\alpha}''$, is then given as

$$\hat{\alpha}'' = \frac{1}{2\pi} \arg\{\sum_{n=1}^{N-1} \hat{d}^*_{LP}[n] \hat{d}_{LP}[n + N]\}, \tag{2.60}$$

where $\hat{d}_{LP}[n]$ is the n-th output of the differential filter in LTSP. As a result, the fine frequency estimation $\hat{\alpha}$ is expressed as

$$\hat{\alpha} = \hat{\alpha}' + \hat{\alpha}''. \tag{2.61}$$

The estimated frequency offset obtained from Eqs. (2.59) and (2.60) is deteriorated by the IQ imbalance because the frequency offset estimation in the time domain

Table 2.4: Pilot subcarriers.

	$k=-21$	$k=-7$	$k=7$	$k=21$
$2m$-th symbol	1	1	1	1
$2m+1$-th symbol	1	1	-1	-1

is carried out in the presence of the IQ imbalance. However, MSE of frequency offset estimation influenced by the IQ imbalance is less than 10^{-3} of the square of the frequency offset [2.29]. Thus, the IQ imbalance is neglected at this stage for estimation of the frequency offset.

2.4.4 Proposed IQ Imbalance Estimation

2.4.4.1 Influence of Differential Filter

Aforementioned in Section 2.4.3, the differential filter is used to cut the residual DC offset. The IQ imbalance is estimated by the pilot symbols in the data period, which passes through the differential filter as shown in Fig. 2.30. The phase and amplitude responses of the received symbols are affected due to the differential filter. The output after the differential filter in the frequency domain is

$$D[k] = H_{\mathrm{DF}}[k]R[k], \tag{2.62}$$

where $D[k]$, $H_{\mathrm{DF}}[k]$, and $R[k]$ are the output of the differential filter, the channel response of the differential filter, and the received signal with IQ imbalance on k-th subcarrier. The channel response on the k-th subcarrier is given as

$$\begin{aligned} & H_{\mathrm{DF}}[k]\Big|_{z=e^{j\frac{2\pi k}{N}}} \\ = \;& 1-\exp(-j\frac{2\pi k}{N}), \quad (k=-\frac{N}{2},\cdots,\frac{N}{2}-1). \end{aligned} \tag{2.63}$$

The frequency responses of the differential filter outputs are compensated from Eq. (2.63).

2.4.4.2 IQ Imbalance Estimation without Frequency Offset

In the proposed scheme, the pilot subcarriers in the data period are used for IQ imbalance estimation. If the frequency offset does not exist, the k-th received symbol in the frequency domain after DFT, $\hat{R}[k]$, is given as

$$\hat{R}[k] = \phi[k]R[k] + \psi^*[-k]R^*[-k], \tag{2.64}$$

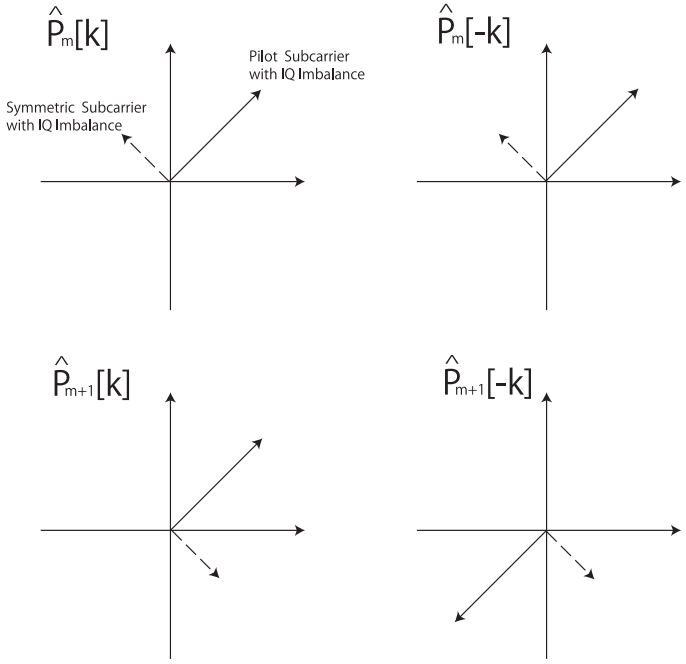

Figure 2.29: Vector representation of pilot subcarriers with IQ imbalance.

with

$$R[k] = \begin{cases} S[k] & k \in \mathbf{N_D}, \\ P[k] & k \in \mathbf{N_P}, \end{cases} \tag{2.65}$$

where $S[k]$ is the k-th data subcarrier, $P[k]$ is the k-th pilot subcarrier, $\mathbf{N_D}$ is the set of indices for the data subcarriers, and $\mathbf{N_P}$ is the set of indices for the pilot subcarriers. In Eq. (2.64),

$$\phi[k] = \phi H[k], \tag{2.66}$$

$$\psi[k] = \psi H[k], \tag{2.67}$$

and $H[k]$ is the channel response of the k-th subcarrier. From Eq. (2.64), the symbol on the k-th subcarrier OFDM symbol is affected by the the symbol on the $[-k]$-th subcarrier due to the IQ imbalance. To estimate the IQ imbalance, the pilot symbols shown in Table 2.4 are transmitted. The IQ imbalance is estimated from the m-th and $(m+1)$-th consecutive OFDM symbols. Those two pilot symbols are written as

$$\hat{P}_m[k] = \phi[k]P_m[k] + \psi^*[-k]P_m^*[-k], \tag{2.68}$$

$$\hat{P}_{m+1}[k] = \phi[k]P_{m+1}[k] + \psi^*[-k]P_{m+1}^*[-k]. \tag{2.69}$$

The mirror subcarriers of Eqs. (2.68) and (2.69) are also written as

$$\hat{P}_m[-k] = \phi[-k]P_m[-k] + \psi^*[k]P_m^*[k], \tag{2.70}$$
$$\hat{P}_{m+1}[-k] = \phi[-k]P_{m+1}[-k] + \psi^*[k]P_{m+1}^*[k]. \tag{2.71}$$

By substituting the values of the pilot symbols from Table 2.4 into Eqs. (2.68)-(2.71) as shown in Fig. 2.29, ϕ and ψ are calculated as

$$\psi^*[-k] = \frac{\hat{P}_m[k] + \hat{P}_{m+1}[k]}{2}, \tag{2.72}$$
$$\phi[k] = \frac{\hat{P}_m[k] - \hat{P}_{m+1}[k]}{2}, \tag{2.73}$$
$$\phi[-k] = \frac{\hat{P}_m[-k] + \hat{P}_{m+1}[-k]}{2}, \tag{2.74}$$
$$\psi^*[k] = \frac{\hat{P}_m[-k] - \hat{P}_{m+1}[-k]}{2}. \tag{2.75}$$

From Eqs. (2.72) to (2.75), it is given as

$$\frac{\psi^*}{\phi^*} = \frac{\psi^*[-k] + \psi^*[k]}{\phi^*[k] + \phi^*[-k]}, \quad \text{for} \quad k \in \mathbf{N_P}. \tag{2.76}$$

From Eqs. (2.51) (2.52) and (2.76), $\hat{\beta}$ and $\hat{\theta}$ are calculated. In the data period, the received signal is compensated with the estimations of ϕ and ψ given in Eqs. (2.37) and (2.38). The received symbol after IQ imbalance compensation, $\tilde{R}[k]$, is expressed as

$$\tilde{R}[k] = \frac{\phi^*\hat{R}[k] - \psi^*\hat{R}[-k]}{|\phi|^2 - |\psi|^2}, \quad \text{for } k \in \mathbf{N_D} \cup \mathbf{N_P}. \tag{2.77}$$

If the IQ imbalance is compensated completely, Eq. (2.77) is given as

$$\tilde{R}[k] = H[k]R[k], \quad \text{for} \quad k \in \mathbf{N_D} \cup \mathbf{N_P}. \tag{2.78}$$

The compensated symbol shown in Eq. (2.78) contains the channel response on the k-th subcarrier. From the estimated channel response on each pilot subcarrier, the channel response of the other subcarriers are compensated with the 1st order interpolation.

2.4.4.3 IQ imbalance Estimation in the presence of Frequency Offset

In the time domain, the frequency offset causes additional phase rotation in the data period. The frequency offset is estimated and compensated in the time domain and IQ imbalance estimation is carried out in the frequency domain as shown

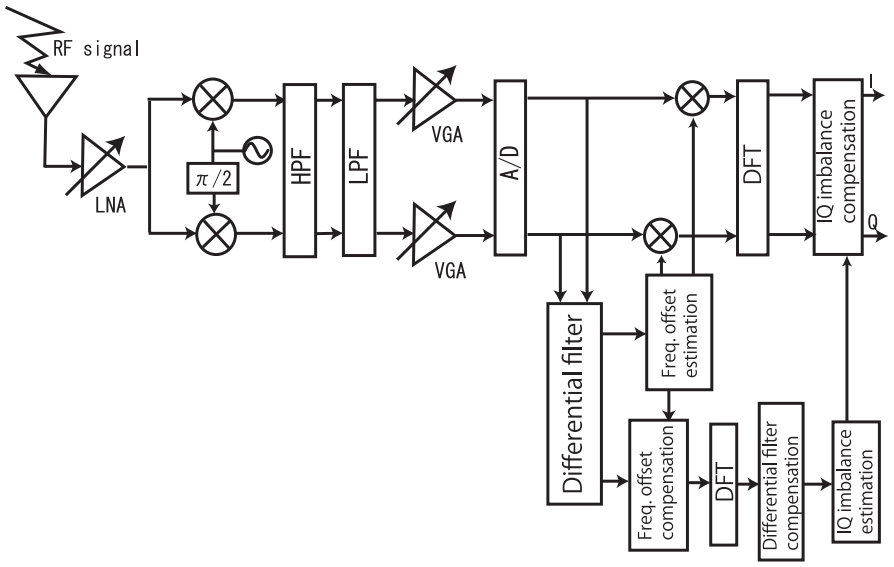

Figure 2.30: Receiver architecture of proposed scheme.

in Fig. 2.30. From Eq. (1.6), the n-th received signal after frequency offset compensation in the time domain, $\hat{r}^{'}[n]$, is expressed as

$$\hat{r}^{'}[n] = \phi r[n] + \psi^{*} r^{*}[n] \exp(-j\frac{2\pi(\alpha+\hat{\alpha})}{N}n). \tag{2.79}$$

The received symbol with the frequency offset in the frequency domain, $\hat{R}^{'}[k]$, is then given as

$$\begin{aligned} & \hat{R}^{'}[k] \\ = & \sum_{n=0}^{N-1} \hat{r}^{'}[n] \exp(-j\frac{2\pi l}{N}n) \\ = & \phi R[k] + \frac{\psi^{*}}{N}\Big(\sum_{n=0}^{N-1} R^{*}[-k] \exp(-j\frac{2\pi(\alpha+\hat{\alpha})}{N}n) \\ + & \sum_{n=0}^{N-1} \sum_{\substack{n=-\frac{N}{2} \\ k' \neq -k}}^{\frac{N}{2}-1} R^{*}[k'] \exp(-j\frac{2\pi(k'+k)}{N}n) \exp(-j\frac{2\pi(\alpha+\hat{\alpha})}{N}n)\Big). \end{aligned} \tag{2.80}$$

From Eq. (2.80), it is shown that the ICI from all the subcarriers and the closstalk from the symmetric subcarriers to the k-th subcarrier deteriorate the accuracy of IQ imbalance estimation as shown in Fig. 2.31. Moreover, the aver-

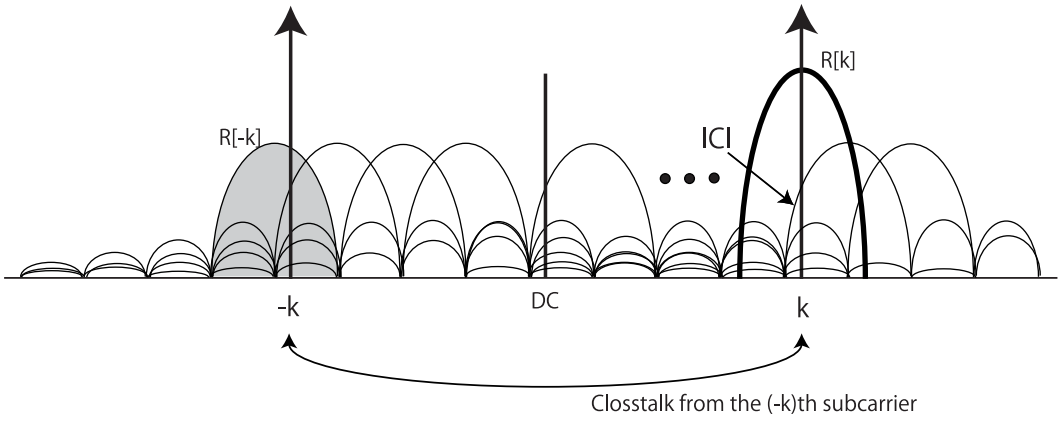

Figure 2.31: Effect of ICI and frequency offset.

aging does not ignore the accuracy since the ICI components are affected by the frequency offset.

2.4.5 Simulation Results

2.4.5.1 Simulation Conditions

The MSE of the IQ imbalance estimation is evaluated through computer simulation. The simulation conditions are shown in Table 2.5. Information bits are modulated with QPSK on each subcarrier. The number of DFT/IDFT points is set to 64 while 52 subcarriers are used for the LTSP symbols, which follows the IEEE 802.11a/g standard. The 1st order butterworth filter is employed as the Rx HPF. The cutoff frequency of the received HPF is set to 10[kHz]. The DC offset is set to 10[dB] [2.28]. The normalized frequency offset varies from 0.1 to 0.5. The mismatch of amplitude is set to values from 0 to 0.1 and the mismatch of phase is set to change from 0 to 10[degrees] [2.21].

2.4.5.2 Normalized MSE Performance vs. Frequency Offset

Figures 2.32 and 2.33 show the normalized MSE performance of gain and phase mismatch estimation, respectively, when the frequency offset α is varied. The phase mismatch β is set to 0.05 and the phase mismatch θ is set to 5[degrees]. E_b/N_0 is set to {10, 15, or 20}[dB]. In those figures, 'Conventional scheme' refers to the IQ imbalance estimation scheme in the time domain as shown in Section 2.3 [2.30]. It is clear that the proposed scheme is superior to the convetional scheme when the frequency offset α is less than 0.2.

Table 2.5: Simulation conditions.

Trial number	10,000 times
Modulation scheme	QPSK+OFDM (Preamble) 64QAM+OFDM (Data)
Number of subcarrier	64
Number of data Subcarrier	52
Channel	AWGN
Rx HPF	1st order Butterworth filter f_B=10[kHz]
DC offset	10 [dB]
Normalized frequency offset	0.001-0.1
Gain mismatch β	0.01-0.05
Phase mismatch θ	1-5 [degrees]

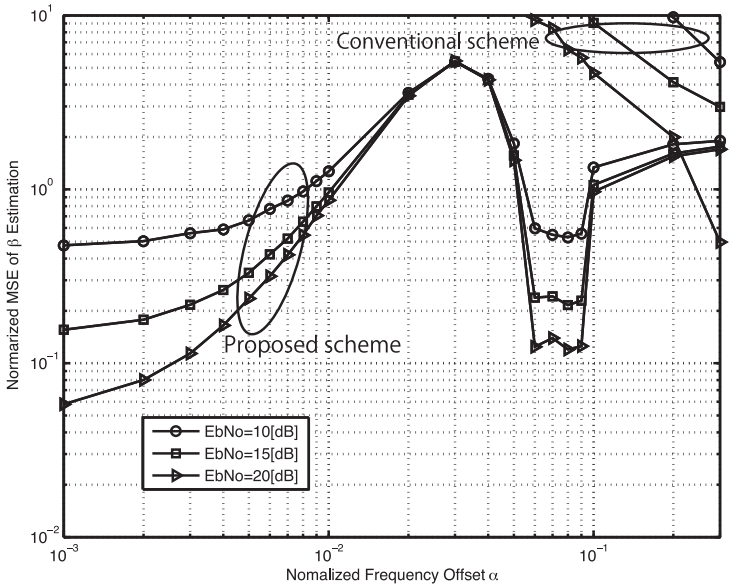

Figure 2.32: Normalized MSE performance of gain mismatch estimation (β=0.05, θ=5[degrees]).

In both figures, the fluctuation in the MSE of the proposed scheme for different frequency offset is due to the effect of the frequency offset in the second term of the right side of Eq. (2.80). This tendency can be observed without ICI ($R[k] = 0,\ \text{for}\ k \in \mathbf{N_D}$) in the numerical results. This is because the frequency offset rotates the phase of ψ^* in the second term of Eq. (2.80).

From Eq. (2.50), with the assumption of small θ, β and θ depend on ε_I and ε_Q,

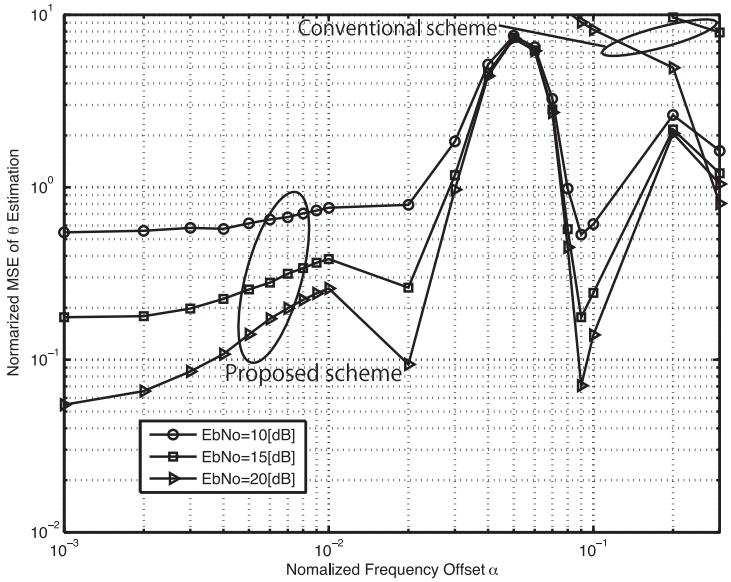

Figure 2.33: Normalized MSE performance of phase mismatch estimation (β=0.05, θ=5[degrees]).

respectively. To see the effect of the frequency offset, the real and imaginary parts of the second term of Eq. (2.80) without the thermal noise are shown in in Figs. 2.34 and 2.35, respectively, when the frequency offset α is varied. In the figures, 'Simulation' indicates the numerical values obtained through computer simulation and 'Ideal' means the value without frequency offset. The fluctuation of the real part directly corresponds to the MSE of β estimation through Eqs. (2.49) and (2.72) as indicated in Fig. 2.32. Also, the fluctuation of the imaginary part is strongly related to the MSE of θ estimation through Eqs. (2.49) and (2.72) as shown in Fig. 2.33.

2.4.5.3 Normalized MSE Performance vs. Gain Mismatch and Phase Mismatch

Figure 2.36 shows the normalized MSE performance of gain mismatch estimation with the DC offset and the frequency offset when the gain mismatch value is varied. The phase mismatch θ is set to 5[degrees] and the frequency offset α is set to 0.001. E_b/N_0 is set to {10, 15, or 20}[dB]. The MSE performance of the proposed scheme is superior than the conventional scheme. It can be seen from Fig. 2.36 that the normalized MSE performance improves as the gain mismatch increases. This is because the MSE is normalized by the gain mismatch β. The normalized MSE of the proposed scheme is reduced by a factor of about $10 - 100$ as compared to the conventional scheme.

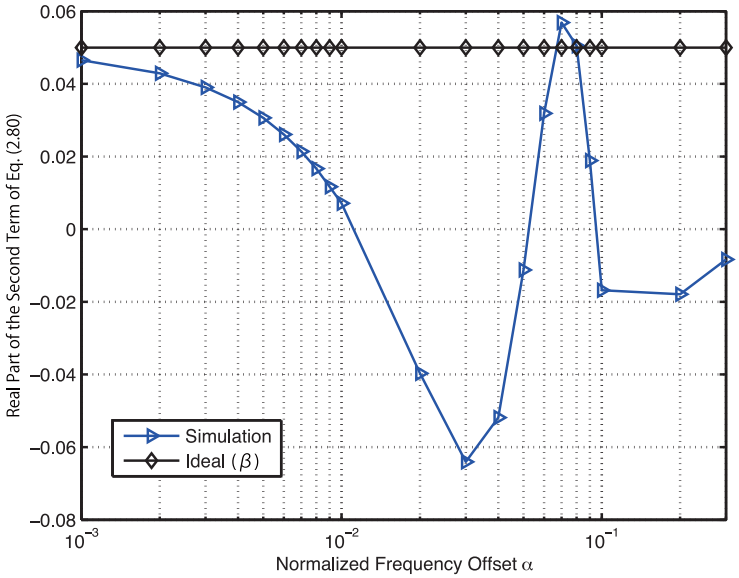

Figure 2.34: Real part of the second term of Eq. (2.80) (SNR = ∞, β=0.05, θ=5[degrees]).

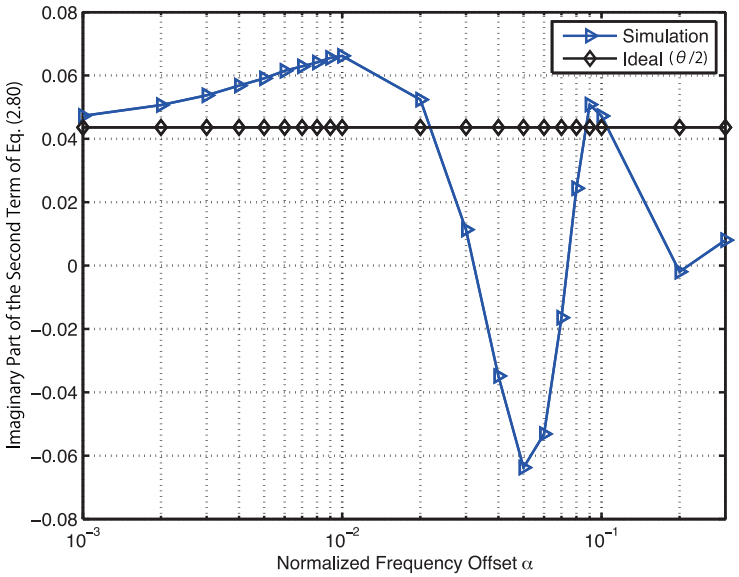

Figure 2.35: Imaginary part of the second term of Eq. (2.80) (SNR = ∞, β=0.05, θ=5[degrees]).

Figure 2.37 shows the normalized MSE performance of phase mismatch estimation with the DC offset and the frequency offset when the phase mismatch value is varied. The phase mismatch β is set to 0.05 and the frequency offset α is set to

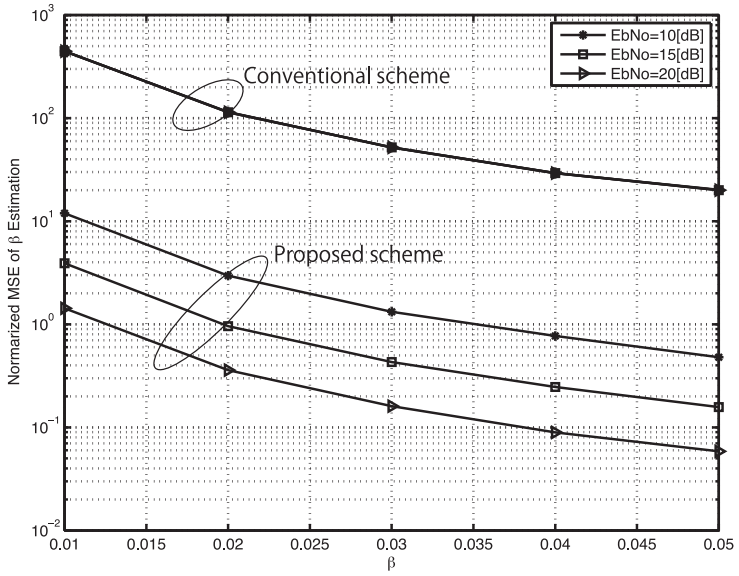

Figure 2.36: Normalized MSE performance of gain mismatch estimation (α=0.001, θ=5[degrees]).

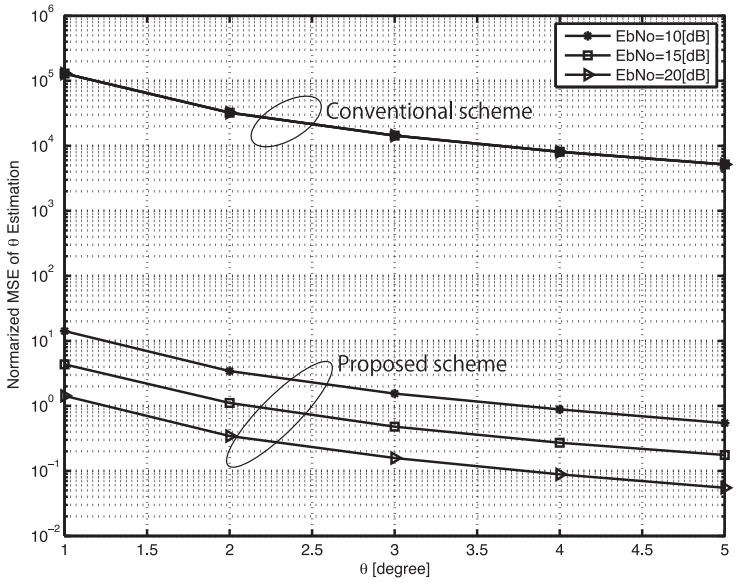

Figure 2.37: Normalized MSE performance of phase mismatch estimation (α=0.001, β=0.05).

0.001. E_b/N_0 is set to {10, 15, or 20}[dB]. In the conventional scheme, the MSE performance is deteriorated in the small frequency offset region and exceeds $(2\pi)^2$ for any amount of the phase mismatch. Thus, the MSE curve of the conventional

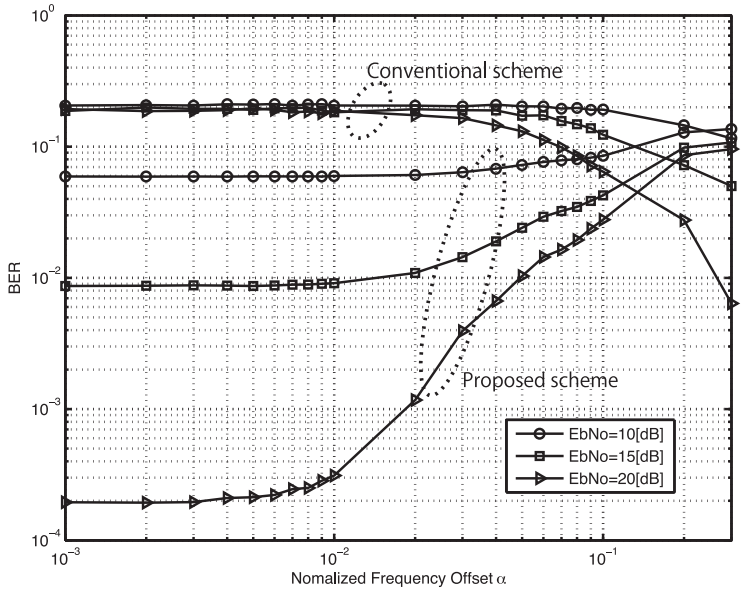

Figure 2.38: BER vs. normalized frequency offset α (64QAM, β=0.05, θ=5[degrees]).

scheme is set to $(2\pi)^2$ and normalized, here. The MSE performance of the proposed scheme is again superior than the conventional scheme. It can be seen from Fig. 2.37 that the normalized MSE curves of both the proposed and conventional schemes improve as the phase mismatch increases. This is because the MSE is normalized by the phase mismatch θ. The normalized MSE of the proposed scheme reduces by a factor of about $10^4 - 10^5$ as compared with the conventional scheme.

2.4.5.4 BER Performance vs. Frequency Offset

Figure 2.38 shows the BER performance versus the frequency offset α. The gain mismatch β is set to 0.05, the phase mismatch θ is set to 5 [degrees], and the frequency offset α ranges from 0.001 to 0.3.

As shown in this figure, the BER curve for the conventional scheme decreases as the frequency offset α increases. This is because IQ imbalance estimation does not work well when the frequency offset is small as mentioned in Section 2.4.4 [2.30]. On the other hand, the BER curve of the proposed scheme is deteriorated as the frequency offset α grows. This is again due to the ICI caused by the frequency offset. From this figure, the proposed scheme exhibits superior estimation performance as compared with the conventional scheme when the frequency offset is small.

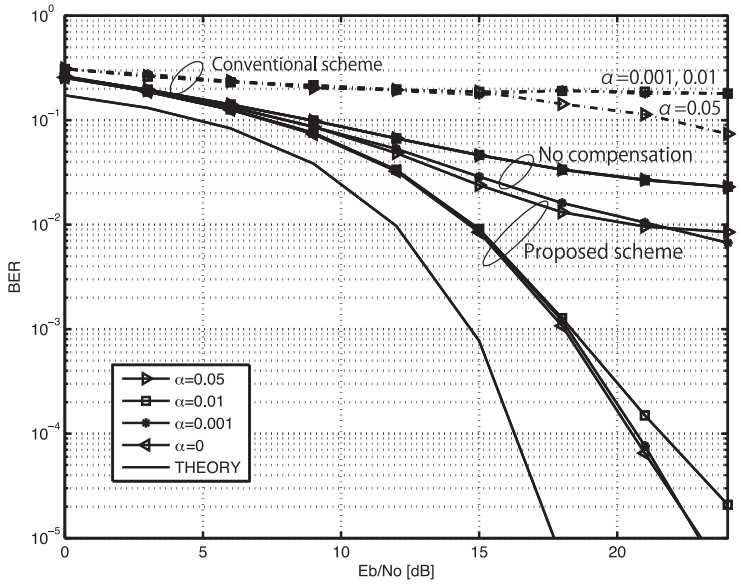

Figure 2.39: BER vs. E_b/N_0 (64QAM, β=0.05, θ=5[degrees]).

2.4.5.5 BER Performance vs. E_b/N_0

Figure 2.39 shows the BER performance in the presence of the frequency offset. 64QAM is used for data modulation. These plots are simulated using the 1st order interpolation for phase compensation by pilot subcarriers. The gain mismatch is $\beta = 0.05$, phase mismatch is $\theta = 5$[degrees], and frequency offset α is set to $\{0,\ 0.001,\ 0.01,\ \text{or}\ 0.05\}$. In this figure, 'Conventional scheme' refers to the IQ imbalance estimation scheme in the time domain as shown in Section 2.4.4 [2.30]. 'No compensation' represents the simulation in the case of no IQ imbalance and frequency offset compensation, 'THEORY' is the theoretical BER curve for 64QAM modulation.

As shown in Fig. 2.39, the BER curve of the conventional scheme actually makes the BER worse because of inaccurate estimation of the IQ imbalance. The proposed IQ imbalance estimation improves the BER performance. However, the BER performance is deteriorated as the frequency offset α increases. This is because the estimated value in Eq. (2.80) suffers from the phase rotation due to the frequency offset.

2.4.6 Conclusions

In this section, a low-complexity IQ imbalance estimation scheme in the presence of the DC offset and the frequency offset has been proposed. The conventional scheme uses the preamble signals in the time domain. However, the BER performance is deteriorated when the frequency offset is small. In the proposed IQ imbalance estimation scheme, the pilot subcarriers in the frequency domain are employed. The numerical results obtained through computer simulation shows that the proposed scheme works well when the frequency offset is small. The proposed scheme improves the accuracy of estimation by a factor of $10 - 10^2$ for the gain mismatch and $10^4 - 10^5$ for the phase mismatch with the small frequency offset.

2.5 Conclusions of Chapter 2

In Chapter 2, the frequency offset and IQ imbalance estimation scheme in the presence of time-varying DC offset for direct conversion receivers has been proposed. In the proposed scheme, the key idea is to use a differential filter for the reduction of the DC offset. The frequency offset and IQ imbalance are estimated with simple calculation from the outputs of the differential filter in the presence of the DC offset. Thus, the proposed low-complexity frequency offset and IQ imbalance estimation schemes are suitable for low-cost and low-power-consumption direct conversion receivers.

2.6 References

[2.1] W. Namgoong and T. H. Meng, "Direct-conversion RF Receiver Design," IEEE Trans. on Commun., vol.49, no.3, pp.518-529, March 2001.

[2.2] R. Svitek and S. Raman, "DC offsets in direct-conversion receivers: characterization and implications," IEEE Microwave Magazine, vol.6, no.3, pp.76-86, Sept. 2005.

[2.3] D. Hui, B. Lidoff, and K. Zangi, "Enhanced DC Estimation via Sequence-Specific Frequency Offset," Proc. of the 56th IEEE Vehicular Technology Conference, vol.1, pp.161-165, Sept. 2002.

[2.4] G. T. Gil, I. H. Sohn, Y. H. Lee, Y. I. Song, and J. K. Park, "Joint ML Estimation of Carrier Frequency, Channel, I/Q Mismatch, and DC offset

in Communications Receivers," IEEE Trans. on Vehi. Tech., vol.54, no.1, pp.338-349, Jan. 2005.

[2.5] C. K. Ho, S.Sun, and P.He, "Low complexity frequency offset estimation in the presence of DC offset," Proc. of IEEE International Conference on Communications, vol.3, pp.2051-2055, May 2003.

[2.6] T. Fujisawa, J. Hasegawa, K. Tsuchie, T. Shiozawa, T. Fujita, T. Saito, and Y. Unekawa, "A Single-Chip 802.11a MAC/PHY With a 32-b RISC Processor," IEEE Journal of Solid-State Circuits, vol.38, no.11, pp.2001-2009, Nov. 2003.

[2.7] H. Yoshida, T. Kato, T. Toyoda, I. Seto, R. Fujimoto, T. Kimura, O. Watanabe, T. Arai, T. Itakura, and H. Tsurumi, "Fully Differential Direct Conversion Receiver for W-CDMA using an Active Harmonic Mixer," Proc. of IEEE Radio Frequency Integrated Circuit Symposium, pp.395-398, Jun. 2003.

[2.8] IEEE.802.11a-Part 11: Wireless LAN Medium Access Control (MAC) and Physical Layer (PHY) specifications; Highspeed Physical Layer in the 5GHZ Band.

[2.9] IEEE.802.11g-Part 11: Wireless LAN Medium Access Control (MAC) and Physical Layer (PHY) specifications; Highspeed Physical Layer in the 2.4GHZ Band.

[2.10] W. Chen, T. Lee, and T. Lu, "A 5-GHz Direct Conversion Receiver with I/Q Phase and Gain Error Calibration," Proc. of IEEE Radio Frequency Integrated Circuit Symposium, pp.201-204, Jun. 2005.

[2.11] R. G. Meyer, W. D. Mack, and J. Hageraats, "A 2.5 GHz BiCMOS Transceiver for Wireless LAN," Proc. of International Solid-State Circuits Conference, pp.310-311, Feb 1997.

[2.12] S. Otaka, T. Yamaji, R. Fujimoto, and H. Tanimoto, "A Low Offset 1.9-GHz Direct Conversion Receiver IC with Spurious Free Dynamic Range of over 67 dB," IEICE Trans. on Fundamentals, vol.E84-A, no.2, pp.513-519, Feb. 2001.

[2.13] J. Olsson, "WLAN/WCDMA Dual-Mode Receiver Architecture Design Trade-Offs," Proc. of the 6th IEEE Circuits and Systems Symposium, vol.2, pp.725-728, May 2004.

[2.14] M. Faulkner, "DC Offset and IM2 Removal in Direct Conversion," IEE Proc. Communications, vol.149, no.3, pp.179-184, June 2002.

[2.15] T. Liu and E. Westerwick, "5 GHz CMOS Radio Transceiver Front-end Chipset," Proc. of International Solid-State Circuits Conference, pp.320-321, Feb. 2000.

[2.16] B. Razavi, "Design Considerations for Direct-Conversion Receivers," IEEE Trans. on Circuits and Systems II: Analog and Digital Signal Processing, vol.44, no.6, pp.428-435, June 1997.

[2.17] A. A. Abidi, "Direct-Conversion Radio Transceivers for Digital Communications," IEEE Journal of Solid-State Circuits, vol.30, no.12, pp.1399-1410, Dec. 1995.

[2.18] R. B. Palipana and K. Chung, "The Effects of Receiver Impairments in Terrestrial Digital Video Broadcasting," Proc. of the 9th Asia-Pacific Conference on Communications, vol.3, pp.1143-1146, Sept. 2003.

[2.19] M. Inamori, A. M. Bostamam, Y. Sanada, and H. Minami, "Frequency Offset Compensation Scheme under DC Offset for OFDM Direct Conversion Receivers," Proc. of the 9th International Symposium on Wireless Personal Multimedia Communications, pp.378-382, Sept. 2006.

[2.20] M. Inamori, A. M. Bostamam, Y. Sanada, and H. Minami, "Frequency Offset Estimation Scheme in the Presence of Time-varying DC Offset for OFDM Direct Conversion Receivers," IEICE Trans. on Commun., vol.E90-B, no.10, pp.2884-2890, Oct. 2007.

[2.21] J. Tubbax, A. Fort, L. V. Perre, S. Donnay, M. Moonen, and H. D. Man, "Joint Compensation of IQ Imbalance and Frequency Offset in OFDM Systems," Proc. of IEEE Global Telecommunications Conference, vol.3, pp.2365-2369, May 2003.

[2.22] D. S. Hilborn, S. P. Stapleton, and H. K. Cavers, "An Adaptive Direct Conversion Transmitter," IEEE Trans. on Veh. Tech., vol.43, no.2, pp.223-233, May 1994.

[2.23] G. Xing, M. Shen, and H. Liu, "Frequency Offset and I/Q Imbalance Compensation for Direct Conversion Receivers," IEEE Trans. on Commun., vol.4, pp.673-680, March 2005.

[2.24] S. D. Rore, E. L. Estraviz, F. Horlin, and L. V. Perre, "Joint Estimation of Carrier Frequency Offset and IQ Imbalance for 4G Mobile Wireless Systems," Proc. of IEEE International Conference on Communications, vol.5, pp.2066-2071, June 2006.

[2.25] A. C. Douglas and S. Haykin, "On the Relationship Between Blind Deconvolution and Blind Source Separation," Proc. of the 31st Asilomar Conference on Signals, Systems & Computers, vol.2, pp.1591-1595, Nov. 1997.

[2.26] M. Valkama, M. Renfors, and V. Koivunen, "Advanced Methods for I/Q Imbalance Compensation in Communication Receivers," IEEE Trans. Signal Processing, vol.49, no.10, pp.2335-2344, Oct. 2001.

[2.27] P. Rykaczewski, J. Brakensiek, and F. Jondral, "Decision Directed Methods of I/Q Imbalance Compensation in OFDM Systems," Proc. of the IEEE 69th Vehicular Technology Conference-Fall, vol.1, pp.484-487, Sept. 2004.

[2.28] M. Inamori, A. M. Bostamam, Y. Sanada, and H. Minami, "Frequency Offset Estimation Scheme in the Presence of Time-varying DC Offset for OFDM Direct Conversion Receivers," IEICE Trans. on Commun., vol.E90-B, no.10, pp.2884-2890, Oct. 2007.

[2.29] M. Inamori, A. M. Bostamam, Y. Sanada, and H. Minami, "Frequency Offset Estimation Scheme in the Presence of Time-varying DC Offset and IQ Imbalance for OFDM Direct Conversion Receivers," Proc. of the 18th Annual International Symposium on Personal Indoor and Mobile Radio Communications, pp.1-5, Sept. 2007.

[2.30] M. Inamori, A. M. Bostamam, Y. Sanada, and H. Minami, "IQ Imbalance Compensation Scheme in the Presence of Frequency Offset and Dynamic DC Offset for a Direct Conversion Receiver," IEEE Trans. on Wireless Communications, vol.8, no.5, pp.2214-2220, May 2009.

Chapter 3

Effect of Timing Jitter on Quadrature Charge Sampling

This chapter evaluates the effect of timing jitter on quadrature charge sampling for an RF-sampling receiver. In contrast to the voltage sampling, the charge sampling mixer integrates the signal current instead of tracking the signal voltage. The charge sampling mixer has been applied to RF direct sampling in wireless receivers. The effect of timing jitter on charge sampling has been analyzed in some literatures. However, in wireless receivers, quadrature sampling is required in order to demodulate I-phase and Q-phase signals. Different from simple charge sampling, timing jitter causes crosstalk between these signals. In this chapter, the effect of timing jitter on quadrature sampling is investigated.

3.1 Introduction

RF front-end and ADCs are the key components of receiver architectures. If it is possible to convert an RF signal directly to the digital samples, the analog components of the receiver can be simplified. However, as there is no ADCs that can be operated at RF, existing receivers cannot convert the received signal from analog to digital domain directly [3.1].

Lately, new receiver architectures have been proposed [3.2]-[3.6]. These receivers sample the received signal in RF. In these architectures, charge sampling mixers are used, and sampling and downconversion are carried out simultaneously. The baseband signal is then extracted through the discrete time analog filters.

The effect of timing jitter on charge sampling has been analyzed, for example, in [3.7][3.8]. It has been shown that the effect of timing jitter on the SNR performance of charge sampling is different from that of voltage sampling. If the timing jitter

is small, the SNR of charge sampling is worse than that of voltage sampling. However, none of these literatures have assumed the application of the charge sampling mixer to wireless receivers. In the wireless receiver, the received signal consists of the I-phase and Q-phase components, which are sampled by quadrature sampling [3.4][3.9]. The receiver may lose the orthogonality between the I-phase and Q-phase components due to timing jitter and suffer from crosstalk between them.

In this chapter, the effect of timing jitter on quadrature charge sampling for an RF-sampling receiver is investigated. The signal-to-interference and noise ratio (SINR) of the downconverted signal is evaluated with different data rates and modulation schemes. In addition, this chapter models the distributions of timing jitter based on the structure of the PLL. In the literature, such as in [3.7][3.8][3.10], it is assumed that timing jitter can be modeled with a Gaussian distribution. However, with a finite number of samples, the distribution of timing jitter has not only a white noise component, but also a doubly integrated white noise component $(1/f^2)$ [3.11][3.12]. It is also shown that the SINRs of charge sampling and voltage sampling are almost equivalent when the jitter is sufficiently small.

This chapter is organized as follows. Section 3.2 gives the model of the phase noise of the PLL. In Section 3.3, the effect of the phase noise on the received signal constellation is analyzed. Section 3.4 shows the numerical results obtained by computer simulation. In this section, the phase noise is generated with random numbers based on the model given in Section 3.2. The SNR and SINR of quadrature charge sampling are presented, and the BER is simulated with AWGN. Section 3.5 gives our conclusions.

3.2 System Model

3.2.1 Receiver Architecture

The receiver architecture assumed in this chapter is shown in Fig. 3.1. In this architecture, the received signal is sampled with the quadrature charge sampler. The quadrature charge sampler samples the received signal at RF. The sampled signals are then input into the finite impulse response (FIR) filters. Here, it is assumed that all the coefficients of the FIR filters are set to 1 and they work as an LPF. The LPF extracts the baseband aliasing component of the sampled signal. Thus, with the charge sampler and the FIR filters, down conversion of the RF signal can be achieved.

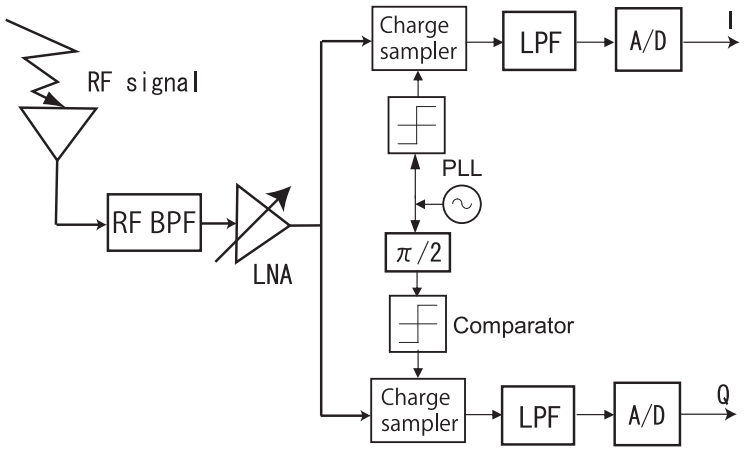

Figure 3.1: Block diagram of the receiver.

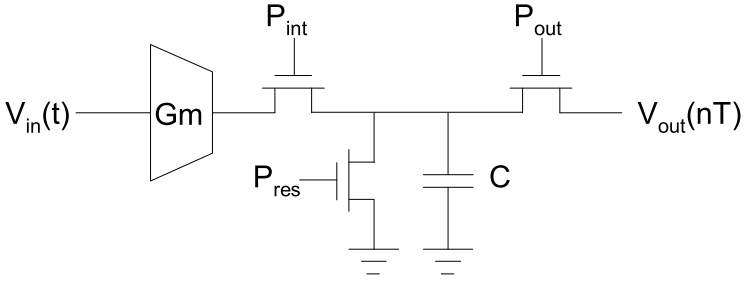

Figure 3.2: Simple integrating charge sampling circuit.

3.2.2 Charge Sampling Circuit

The simple circuit of the charge sampler is shown in Fig. 3.2 [3.7]. The input voltage is first transformed into a corresponding current with a transconductance element. For simplicity, it is assumed that this element performs ideal V-to-I conversion. The output current of the transconductor is integrated into the sampling capacitor during a predetermined period with the sampling switch P_{int}. After the integration period, the output is sampled with the switch P_{out}, and the sampling capacitor is discharged with the switch P_{res} before a new sample is taken.

3.2.3 PLL Model

The system model of the PLL is shown in Fig. 3.3. It is assumed that the output signal is synchronized with that of the carrier signal for simplicity. This assumption holds for a direct conversion receiver because the amount of phase rotation of

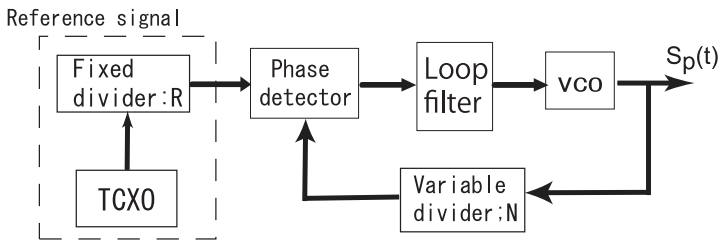

Figure 3.3: Block diagram of the PLL.

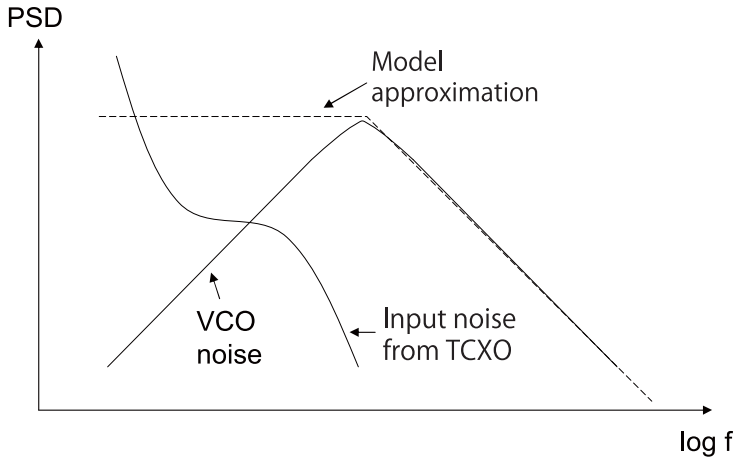

Figure 3.4: Typical PSD of the PLL phase noise.

the demodulated signal can be detected in the digital domain, and phase synchronization may be achieved ideally with a digitally controlled oscillator [3.6].

The output from the PLL contains the phase noise whose spectrum has the typical shape shown in Fig. 3.4. There are two major noise sources[3.11]. One is the voltage-controlled oscillator (VCO), the other one is the temperature-compensated crystal oscillator (TCXO) [3.12]. The phase noise caused by the TCXO is low-pass-filtered by the transfer function of the PLL, and its power spectrum is concentrated at around the carrier frequency. On the other hand, the power spectrum density (PSD) of the phase noise caused by the VCO is much lower than that of the noise caused by the TCXO at around the output frequency of the PLL. It can be seen in Fig. 3.4 that the PSD value increases with frequency until it reaches a peak and then decreases in proportion to the logarithm of frequency. It is the dominant source of the phase noise if the frequency is far away from the output frequency.

For simplicity, it is assumed here that the PSD of the phase noise consists of two components as shown in Fig. 3.5 [3.11]. One has a white spectrum shape with a

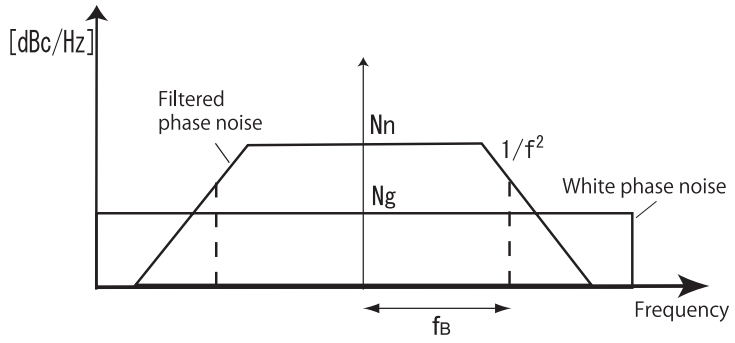

Figure 3.5: Modeled PSD of the PLL phase noise.

density of N_g. This component is dominant at frequency regions lower and higher than the output frequency. The other one has a nonwhite spectrum shape with a density of N_n at the output frequency. This PSD can be modeled by a single-pole low-pass filter with a cutoff frequency of f_B [3.12]. This component is dominant around the output frequency.

3.3 Numerical Analysis

In this section, the effect of the phase noise modeled in Section 3.2 on signal constellation with single carrier QAM and OFDM modulation is analyzed. The SNR and SINR are then derived.

3.3.1 Single Carrier QAM

The transmitted signal is modulated with single carrier QAM and transmitted over the AWGN channel. The received signal is given as

$$\begin{aligned} r(t) &= s(t) + v(t) \\ &= A_I(t)m_I \cos(\omega_c t) + A_Q(t)m_Q \sin(\omega_c t) + v(t), \end{aligned} \tag{3.1}$$

where A_I and A_Q are the amplitudes, and m_I and m_Q are the information signals of the I-phase and Q-phase components, respectively.

The received RF signal is sampled as shown in Fig. 3.6. Here, the sampling process is modeled by the multiplication of the received signal by the rectangular signal and integration. It is also assumed that the phase of the rectangular signal is synchronized with the received carrier signal. Each sampled signal of the I-phase or Q-phase components is an integrated half cycle of the carrier signal as shown in Fig. 3.7.

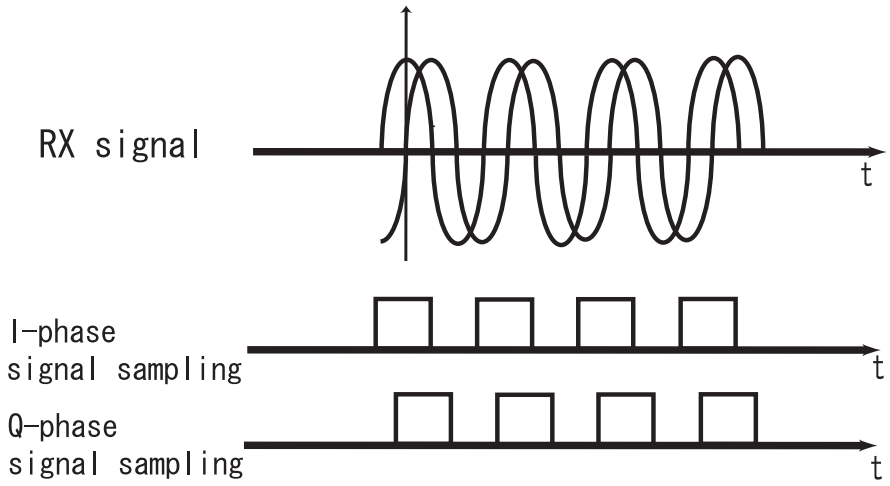

Figure 3.6: Quadrature sampling.

Here, the timing jitter on the I-phase or Q-phase signals is represented as $\tau[n]$. The narrow-band Gaussian noise $v(t)$ is given by

$$v(t) = v_I(t)\cos(\omega_c t) + v_Q(t)\sin(\omega_c t). \tag{3.2}$$

When the symbol rate is f_s, one symbol is transmitted from $-\frac{1}{4f_c}$ to $\frac{\frac{f_s}{f_c}-1}{f_c} + \frac{3}{4f_c}$. The n-th sampled signal of the I-phase component $r_I[n]$ is then given by

$$\begin{aligned} r_I[n] &= \frac{1}{\Delta}\int_{(\frac{n}{f_c}-\frac{\Delta}{2})+\tau[n]}^{(\frac{n}{f_c}+\frac{\Delta}{2})+\tau[n]} \{s(t)+v(t)\}\, dt \\ &= (A_I[n]m_I + v_I[n])\mathrm{sinc}(f_c\Delta)\cos(\omega_c\tau[n]) \\ &\quad +(A_Q[n]m_Q + v_Q[n])\mathrm{sinc}(f_c\Delta)\sin(\omega_c\tau[n]), \end{aligned} \tag{3.3}$$

where Δ is the integration period, and $A_I[n]$, $A_Q[n]$, $v_I[n]$, and $v_Q[n]$ are given as follows.

$$A_I[n] = \int_{(\frac{n}{f_c}-\frac{\Delta}{2})+\tau[n]}^{(\frac{n}{f_c}+\frac{\Delta}{2})+\tau[n]} A_I(t)\, dt, \tag{3.4}$$

$$A_Q[n] = \int_{(\frac{n}{f_c}-\frac{\Delta}{2})+\tau[n]}^{(\frac{n}{f_c}+\frac{\Delta}{2})+\tau[n]} A_Q(t)\, dt, \tag{3.5}$$

$$v_I[n] = \int_{(\frac{n}{f_c}-\frac{\Delta}{2})+\tau[n]}^{(\frac{n}{f_c}+\frac{\Delta}{2})+\tau[n]} v_I(t)\, dt, \tag{3.6}$$

$$v_Q[n] = \int_{(\frac{n}{f_c}-\frac{\Delta}{2})+\tau[n]}^{(\frac{n}{f_c}+\frac{\Delta}{2})+\tau[n]} v_Q(t)\, dt. \tag{3.7}$$

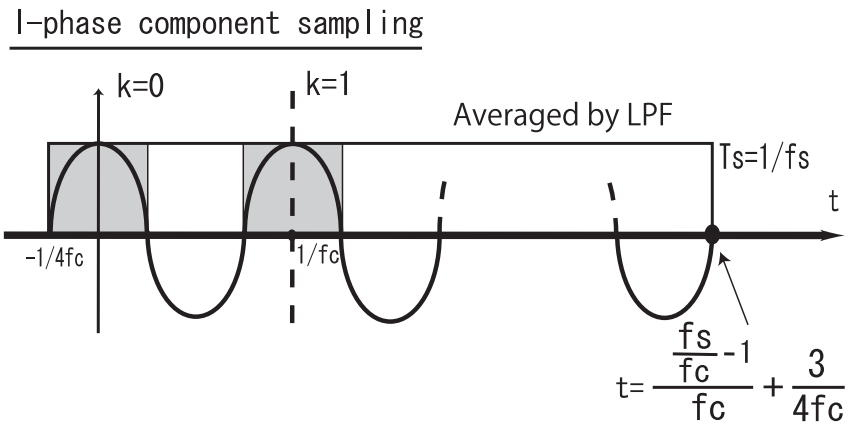

Figure 3.7: Sampling of the I-phase component.

$\omega_c\tau[n]$ is much less than the cycle of the carrier signal. The following approximation can then be applied.

$$\sin(\omega_c\tau[n]) \approx \omega_c\tau[n], \tag{3.8}$$

$$\cos(\omega_c\tau[n]) \approx 1 - {\omega_c}^2\tau[n]^2/2. \tag{3.9}$$

From Eqs. (3.8) and (3.9), by setting $\Delta = 1/2f_c$, Equation (3.3) is approximated as

$$\begin{aligned} r_I[n] &\approx \frac{2(A_I[n]m_I + v_I[n])}{\pi}(1 - \frac{{\omega_c}^2\tau[n]^2}{2}) + \frac{2(A_Q[n]m_Q + v_Q[n])}{\pi}(\omega_c\tau[n]) \\ &\approx \frac{2(A_I[n]m_I + v_I[n])}{\pi} + \frac{2(A_Q[n]m_Q + v_Q[n])}{\pi}(\omega_c\tau[n]). \end{aligned} \tag{3.10}$$

The n-th sampled signal of the Q-phase component is also given as

$$\begin{aligned} r_Q[n] &= \frac{1}{\Delta}\int_{\frac{k}{f_c}+\tau[n]}^{(\frac{n}{f_c}+\frac{1}{2f_c})+\tau[n]} \{s(t) + v(t)\}\, dt \\ &\approx \frac{2(A_Q[n]m_Q + v_Q[n])}{\pi} - \frac{2(A_I[n]m_I + v_I[n])}{\pi}(\omega_c\tau[n]). \end{aligned} \tag{3.11}$$

These sampled signals of the I-phase and Q-phase components are input into the

LPFs, respectively, the outputs of which are given by

$$\begin{aligned} d_I &= \sum_{n=0}^{f_c/f_s-1} r_I[n] \\ &= \sum_{n=0}^{f_c/f_s-1} \frac{2(\bar{A}_I[n]m_I + v_I[n])}{\pi} + \frac{2(\bar{A}_Q[n]m_Q + v_Q[n])}{\pi}(\omega_c\tau[n]) \\ &= \frac{2(\bar{A}_I[n]m_I + \bar{v}_I)(f_c/f_s)}{\pi} + \frac{2(\bar{A}_Q[n]m_Q + \bar{v}_Q)(f_c/f_s)}{\pi}(\omega_c\bar{\tau}), \quad (3.12) \\ d_Q &= \sum_{n=0}^{f_c/f_s-1} r_Q[n] \\ &= \sum_{n=0}^{f_c/f_s-1} \frac{2(\bar{A}_Q m_Q + v_Q[n])}{\pi} - \frac{2(\bar{A}_I m_I + v_I[n])}{\pi}(\omega_c\tau[n]) \\ &= \frac{2(\bar{A}_Q m_Q + \bar{v}_Q)(f_c/f_s)}{\pi} - \frac{2(\bar{A}_I m_I + \bar{v}_I)(f_c/f_s)}{\pi}(\omega_c\bar{\tau}), \quad (3.13) \end{aligned}$$

where

$$\bar{\tau} = \frac{f_s}{f_c}\sum_{n=0}^{f_c/f_s-1} \tau[n], \quad (3.14)$$

$$\bar{A}_I = \frac{f_s}{f_c}\sum_{n=0}^{f_c/f_s-1} A_I[n], \quad (3.15)$$

$$\bar{A}_Q = \frac{f_s}{f_c}\sum_{n=0}^{f_c/f_s-1} A_Q[n], \quad (3.16)$$

$$\bar{v}_I = \frac{f_s}{f_c}\sum_{n=0}^{f_c/f_s-1} v_I[n], \quad (3.17)$$

$$\bar{v}_Q = \frac{f_s}{f_c}\sum_{n=0}^{f_c/f_s-1} v_Q[n]. \quad (3.18)$$

Suppose that

$$G = 2(f_c/f_s)/\pi, \quad (3.19)$$

Eqs. (3.12) and (3.13) become

$$d_I = G\{(\bar{A}_I m_I + \bar{v}_I) + (\bar{A}_Q m_Q + \bar{v}_Q)(\omega_c\bar{\tau})\}, \quad (3.20)$$

$$d_Q = G\{(\bar{A}_Q m_Q + \bar{v}_Q) - (\bar{A}_I m_I + \bar{v}_I)(\omega_c\bar{\tau})\}, \quad (3.21)$$

where $\bar{v}_I$ and $\bar{v}_Q$ are the white Gaussian noise with zero mean and a variance of N_0, respectively.

From Eq. (1.13), $\bar{\tau}$ is given as

$$\begin{aligned}
\bar{\tau} &= \frac{f_s}{f_c} \sum_{n=0}^{f_c/f_s-1} \tau[n] \\
&= \frac{f_s}{f_c} \sum_{n=0}^{f_c/f_s-1} \frac{v_p(nt_c)}{\omega_c} \\
&= \frac{f_s}{\omega_c f_c} \sum_{n=0}^{f_c/f_s-1} v_p(nt_c) \\
&= \frac{\bar{v}_p}{\omega_c}. \qquad (3.22)
\end{aligned}$$

Thus, Eqs.(3.20) and (3.21) can be rewritten as

$$\begin{aligned}
d_I &= G\{(\bar{A}_I m_I + \bar{v}_I) + (\bar{A}_Q m_Q + \bar{v}_Q)(\bar{v}_p)\}, \qquad (3.23) \\
d_Q &= G\{(\bar{A}_Q m_Q + \bar{v}_Q) - (\bar{A}_I m_I + \bar{v}_I)(\bar{v}_p)\}. \qquad (3.24)
\end{aligned}$$

From d_I and d_Q, the QAM symbol is demodulated.

3.3.2 OFDM Modulation

For the case of OFDM modulation, from Eqs.(3.23) and (3.24), the n-th sampled signal of the I-phase or Q-phase component is rewritten as

$$\begin{aligned}
d_I[n] &= G\{(\bar{A}_I m_I[n] + \bar{v}_I[n]) + (\bar{A}_Q m_Q[n] + \bar{v}_Q[n])(\bar{v}_p)\}, \qquad (3.25) \\
d_Q[n] &= G\{(\bar{A}_Q m_Q[n] + \bar{v}_Q[n]) - (\bar{A}_I m_I[n] + \bar{v}_I[n])(\bar{v}_p)\}, \qquad (3.26)
\end{aligned}$$

where

$$d[n] = d_I[n] + j d_Q[n]. \qquad (3.27)$$

Therefore, the demodulated signal on the k-th subcarrier can be written as

$$s[k] = \frac{1}{N} \sum_{n=0}^{N-1} d[n] \exp(j2\pi kn/N). \qquad (3.28)$$

3.3.3 SNR and SINR

As shown in Eqs. (3.3) and (3.9), timing jitter reduces the received signal amplitude from $A_I[n]$ to $A_I[n](1 - \omega_c^2 \tau[n]^2/2)$. From Eqs. (3.14) and (3.15), the

amplitude of the received I-phase signal is given as $\bar{A}_I(1-\omega_c^2\bar{\tau}^2/2)$. Therefore, the SNR of the sampled I-phase component is calculated as [3.7][3.8]

$$\text{SNR} = \frac{(\bar{A}_I + \bar{v}_I)^2}{(\bar{A}_I + \bar{v}_I)^2(\frac{\omega_c^2\bar{\tau}^2}{2})^2} = \frac{4}{\omega_c^4\bar{\tau}^4}. \tag{3.29}$$

However, as shown in Eq. (3.3), for the case of quadrature sampling, there is a crosstalk component from the Q-phase signal. Therefore, the SINR of the received signal is calculated as

$$\text{SINR} = \frac{(\bar{A}_I + \bar{v}_I)^2}{((\bar{A}_I + \bar{v}_I)\frac{\omega_c^2\bar{\tau}^2}{2})^2 + ((\bar{A}_Q + \bar{v}_Q)\omega_c\bar{\tau})^2}. \tag{3.30}$$

3.3.4 Comparison of Charge Sampling and Voltage Sampling

From Fig. 3.7 and Eq. (3.3), the charge sampling of the I-phase component of the carrier signal with the integration period of Δ and the timing jitter of $\tau[n]$ is expressed as

$$\begin{aligned} & \frac{1}{\Delta}\int_{-\infty}^{\infty} \text{rect}\big(\frac{t-(\frac{n}{f_c}+\tau[n])}{\Delta}\big)\cos(\omega_c t)dt \\ = \; & \frac{1}{\Delta}\int_{(\frac{n}{f_c}-\frac{\Delta}{2})+\tau[n]}^{(\frac{n}{f_c}+\frac{\Delta}{2})+\tau[n]} \cos(\omega_c t)dt \end{aligned} \tag{3.31}$$

where $\text{rect}(at)$ is the rectangular pulse shape with a width of a.

For charge sampling with the integration period of Δ, Eq. (3.31) is rewritten as

$$\begin{aligned} & \frac{1}{\Delta\omega_c}[\sin(\omega_c t)]_{\frac{n}{f_c}-\frac{\Delta}{2}+\tau[n]}^{\frac{n}{f_c}+\frac{\Delta}{2}+\tau[n]} \\ = \; & \frac{1}{\Delta\omega_c}(\sin(2\pi k + \pi f_c\Delta + \omega_c\tau[n]) - \sin(2\pi k - \pi f_c\Delta + \omega_c\tau[n])) \\ = \; & \frac{2}{\Delta\omega_c}\sin(\pi f_c\Delta)\cos(\omega_c\tau[n]) \\ = \; & \text{sinc}(f_c\Delta)\cos(\omega_c\tau[n]). \end{aligned} \tag{3.32}$$

The charge sampling of the Q-phase component is described as

$$\begin{aligned} & \int_{(\frac{n}{f_c}-\frac{\Delta}{2})+\tau[n]}^{(\frac{n}{f_c}+\frac{\Delta}{2})+\tau[n]} \sin(\omega_c t)dt \\ = & \frac{2}{\Delta\omega_c}\sin(\pi f_c\Delta)\sin(\omega_c\tau[n]) \\ = & \operatorname{sinc}(f_c\Delta)\sin(\omega_c\tau[n]). \end{aligned} \tag{3.33}$$

Then the SINR is given as in Eq. (3.30) with the condition of $\Delta = 1/2f_c$.

On the other hand, as Δ approaches 0, the rectangular pulse turns into Dirac's delta function. Voltage sampling is then expressed as follows:

$$\begin{aligned} & \lim_{\Delta\to 0}\frac{1}{\Delta}\int_{-\infty}^{\infty}\operatorname{rect}\Big(\frac{t-(\frac{n}{f_c}+\tau[n])}{\Delta}\Big)r(t)dt \\ = & \int_{-\infty}^{\infty}\delta\big(t-(\frac{n}{f_c}+\tau[n])\big)r(t)dt \\ = & r\big(\frac{n}{f_c}+\tau[n]\big). \end{aligned} \tag{3.34}$$

The SINR of the voltage sampling is then given as [3.8]

$$\begin{aligned} & \frac{E[r^2(\frac{n}{f_c})]}{E[(r(\frac{n}{f_c}+\tau[n])-r(\frac{n}{f_c}))^2]} \\ \approx & \frac{E[r^2(\frac{n}{f_c})]}{E[r'^2(\frac{n}{f_c})\tau^2[n]]} \\ = & \frac{E[(A_I(\frac{n}{f_c})m_I(\frac{n}{f_c})+n_I(\frac{n}{f_c}))^2\cos^2(\omega_c\frac{n}{f_c})]}{E[((-A_I(\frac{n}{f_c})m_I(\frac{n}{f_c})+n_I(\frac{n}{f_c}))^2\sin(\omega_c\frac{n}{f_c})+(A_Q(\frac{n}{f_c})m_Q(\frac{n}{f_c})+n_Q(\frac{n}{f_c}))\cos(\omega_c\frac{n}{f_c}))^2\omega_c^2\tau^2[n]]} \\ = & \frac{(\bar{A_I}+\bar{v}_I)^2}{(\bar{A_Q}+\bar{v}_Q)^2\omega_c^2\bar{\tau}^2}. \end{aligned} \tag{3.35}$$

Comparing Eqs. (3.30) and (3.35), depending on the phase of the carrier signal, it is clear that the SNR of voltage sampling can be much better than that of charge sampling with small timing jitter. However, in terms of the SINR, there is no significant difference between charge sampling and voltage sampling.

3.4 Numerical Results

3.4.1 Simulation Conditions

The effect of the modeled timing jitter on the received signal is evaluated by computer simulation. The simulation conditions are shown in Table 3.1.

Table 3.1: Simulation conditions.

RF frequency	2.4 GHz
Number of simulated symbols	1,000,000 symbols
Modulation scheme	QAM (QPSK, 16QAM, 64QAM)
	OFDM (QPSK, 16QAM, 64QAM)
Number of subcarriers (OFDM)	64
Symbol rate f_s	0.1,1,10,100 [Msymbol/s]
Channel	AWGN
PSD of nonwhite phase noise N_n	-80
Cutoff frequency f_B	10 [kHz]
PSD of white phase noise N_g	-150∼-100 [dBc/Hz]

White noise components of the phase noise are assumed to have PSDs ranging from -150 to -100 [dBc/Hz]. For example, the noise of the PLL proposed in [3.13] shows a PSD of -110 [dBc/Hz]. The non-white noise component is modeled by the single-pole low-pass filter with a cutoff frequency of 10 [kHz]. The PSD of this component, N_n, is simulated with -80 [dBc/Hz] [3.13]. The simulation is conducted with the symbol rates ranging from 0.1 to 100 [Msymbol/sec]. The effects of the timing jitter on the SINR and BER performances are evaluated with single carrier QAM and OFDM modulation.

3.4.2 SNR and SINR

Figures 3.8 and 3.9 show the SNR and SINR of the I-phase component defined in Eqs. (3.29) and (3.30) as functions of the symbol rate. E_b/N_0 is set to 14 [dB]. The SNR and SINR show the same performance curves for both modulation schemes. As the symbol rate decreases, both the SNR and SINR improve due to the noise reduction capability of the FIR filter. The SNR remains unchanged among three different modulation schemes, whereas the SINR largely depends on them. This is due to the fact that the SINR is defined by the crosstalk term between the I-phase and Q-phase components. With the same E_b/N_0, the crosstalk term becomes larger as the modulation index increases. Also, the SINR is significantly lower than the SNR. Thus, instead of the SNR, the SINR should be calculated for quadrature charge sampling in wireless receivers.

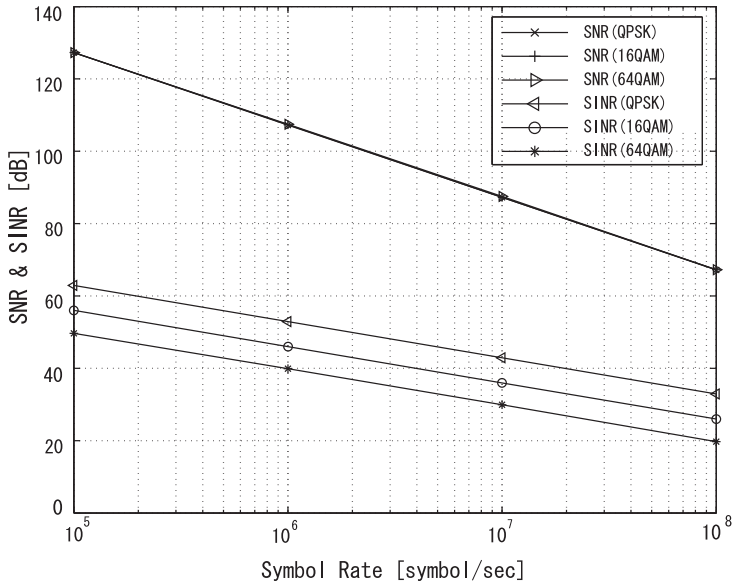

Figure 3.8: SNR and SINR versus symbol rate, (single carrier, $E_b/N_0 = 14$ [dB]).

3.4.3 BER

The BER performance versus E_b/N_0 with single carrier 64QAM is shown in Fig. 3.10. The symbol rate is 100 [Msymbol/s]. In this figure, when N_g is more than -110 [dBc/Hz], the BER performance is worse than the theoretical performance. This is due to the crosstalk component caused by the timing jitter in the quadrature charge sampling mixers.

This result can be confirmed with a simple approximation. Assume that N_g is -100 [dBc/Hz] and the symbol rate is 100 [Msymbol/s]. From Eq. (1.13), $E[(\omega_c \tau[n])^2] = -20$ [dB], and from Eq. (3.30), the SINR of the sampled signal is about 20 [dB]. When $E_b/N_0 = 14$ [dB], i.e., $E_s/N_0 = 22$ [dB], the variance of the thermal noise is almost the same as that of the interference. Thus, the BER with the timing jitter and $E_b/N_0 = 14$ [dB] should be the same as the theoretical performance with $E_b/N_0 = 11$ [dB], which is the result obtained in Fig. 3.10.

The BER performance versus the symbol rate with single carrier 64QAM is shown in Fig. 3.4.3. E_b/N_0 is set to 14 [dB]. As shown in this figure, as the symbol rate increases, the BER increases. This is because the averaging effect of the FIR filter decreases as the bandwidth increases.

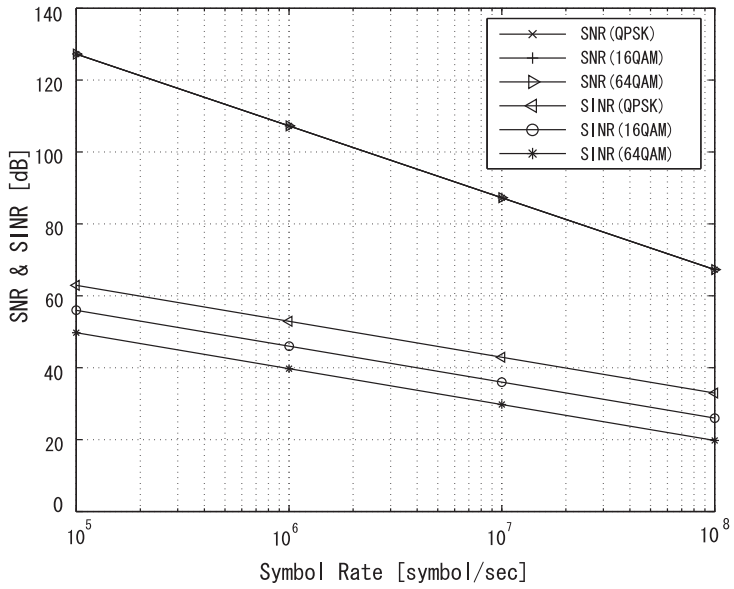

Figure 3.9: SNR and SINR versus symbol rate, (OFDM, $E_b/N_0 = 14$ [dB]).

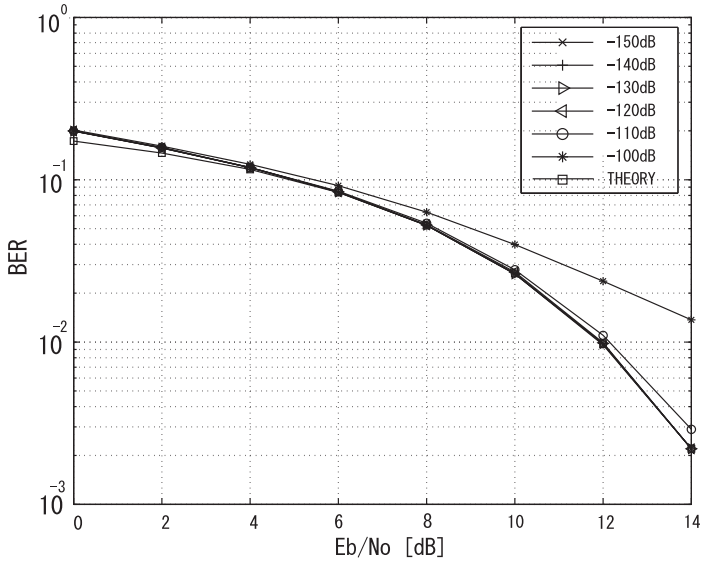

Figure 3.10: BER versus Eb/No, (N_g =-100 [dBc/Hz], symbol rate=100 [Msymbol/s], single carrier 64QAM).

3.5 Conclusions of Chapter 3

In this chapter, the effect of timing jitter on quadrature charge sampling has been derived and evaluated through computer simulation. Instead of the SNR, the

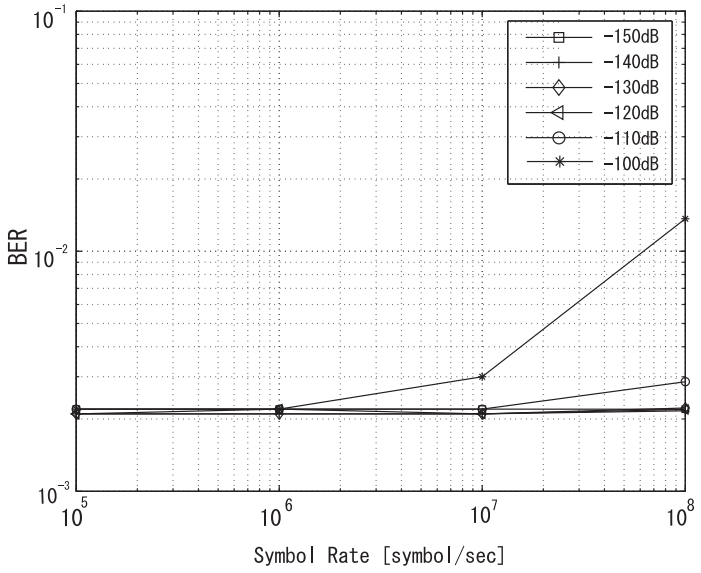

Figure 3.11: BER versus symbol rate (N_g = -100 [dBc/Hz], E_b/N_0 = 14 [dB], single carrier 64QAM).

SINR of the demodulated signal has been analyzed for wireless communication applications. It has been shown that timing jitter deteriorates the SINR of the demodulated signal due to crosstalk between the I-phase and Q-phase components of the received signal. The BER performances with both single carrier QAM and OFDM modulation schemes has shown the error floor with higher data rates. Therefore, in a wideband system, the timing jitter in quadrature charge sampling may limit the performance of the receiver. It has also been shown that the SINRs of charge sampling and voltage sampling are almost the same, while the SNR of voltage sampling is better than that of charge sampling.

3.6 References

[3.1] R. H. Walden, "Performance Trends for Analog-to-Digital Converters," IEEE Communications Magazine, vol.37, no.2, pp.96-101, Feb. 1999.

[3.2] J. Yuan, "A Charge Sampling Mixer with Embedded Filter Function for Wireless Applications," Proc. of the 2nd International Conference on Microwave and Millimeter Wave Technology, pp.315-318, Sept. 2000.

[3.3] S. Karvonen, T. Riley, and J. Kostamovaara, "Charge Sampling Mixer with $\Delta\Sigma$ Quantized Impulse Response," Proc. of International Symposium on Circuits and Systems, vol.1, pp.129-132, May 2002.

[3.4] K. Muhammad, D. Leipold, B. Staszewski, Y. C. Ho, C. M. Hung, K. Maggio, C. Fernando, T. Jung, J. Wallberg, J. S. Koh, S. John, I. Deng, O. Moreira, R. Staszewski, R. Katz, and O. Friedman, "Discrete-Time Bluetooth Receiver in a 0.13 μ m Digital CMOS Process," Proc. of International Solid-State Circuits Conference, vol.1, pp.268-527, Feb. 2004.

[3.5] K. Muhammad and R. B. Staszewski, "Direct RF Sampling Mixer with Recursive Filtering in Charge Domain," Proc. of International Symposium on Circuits and Systems, vol.1, pp.577-580, May 2004.

[3.6] R. B. Staszewski, K. Muhammad, D. Leipold, C. M. Hung, Y. C. Ho, J. L. Wallberg, C. Fernando, K. Maggio, R. Staszewski, T. Jung, J. S. Koh, S. John, D. I. Yuanying, V. Sarda, O. M. Tamayo, V. Mayega, R. Katz, O. Friedman, O. E. Eliezer, E. Obaldia, and P. T. Balsara, "All-Digital TX Frequency Synthesizer and Discrete-Time Receiver for Bluetooth Radio in 130-nm CMOS," IEEE Journal of Solid-State Circuits, vol.39, no.12, pp.2278-2291, Dec. 2004.

[3.7] S. Karvonen, T. Riley, and J. Kostamovaara, "On the Effects of Timing Jitter in Charge Samping," Proc. of International Symposium on Circuits and Systems, vol.1, pp.737-740, May 2003.

[3.8] G. Xu and J. Yuan, "Performance Analysis of General Charge Sampling," IEEE Trans. on Circuts and Systems-II:Express Briefs, vol.52, no.2, pp.107-111, Feb. 2005.

[3.9] S. Karvonen, T. A. D. Riley, and J. Kostamovaara, "A CMOS Quadrature Charge-Domain Sampling Circuit with 66-dB SFDR up to 100HMz," IEEE Trans. on Circuits and Systems-I, vol.52, no.2, pp.105-117, March 2003.

[3.10] M. Shinagawa, Y. Akazawa, and T. Wakimoto, "Jitter Analysis of High-Speed Sampling Systems," IEEE Journal of Solid-State Circuits, vol.25, no.1, pp.220-224, Feb. 1990.

[3.11] N. D. Dait, M. Harteneck, C. Sandner, and A. Wiesbauer, "Numerical Modeling of PLL Jitter and the Impact of its Non-white Spectrum on the SNR of Sampled Signals," Proc. of Southwest Symposium on Mixed-Signal Design, pp.38-44, Feb. 2001.

[3.12] N. D. Dalt, "Effect of Jitter on Asynchronous Sampling with Finite Number of Samples," IEEE Trans. on Circuits and Systems-II: Express Briefs, vol.51, no.12, pp.660-664, Dec. 2004.

[3.13] R. B. Staszewski, C. Hung, D. Leipold, and P. T. Balsara, "A First Multi-gigahertz Digitally Controlled Oscillator for Wireless Applications," IEEE Trans. on Microwave Theory and Techniques, vol.51, no.11, pp.2154-2164, Nov. 2003.

Chapter 4

Correlated Noise Cancellation Scheme in Fractional Sampling OFDM System

In this chapter, compensation schemes for signal distortion in FS OFDM receivers are evaluated. The OFDM system with FS can achieve diversity with a single antenna. In FS system, as the number of subcarriers and the oversampling ratio increase, the correlation among the noise components over different subcarriers deteriorates the BER performance. In Section 4.1, a correlated noise cancellation scheme in FS OFCDM system is investigated. For applicability to OFDM systems, the effect of the correlation among the noise components in FS OFDM system is derived in Section 4.2. A metric weighting scheme for the coded FS OFDM system is also proposed and investigated.

4.1 Fractional Sampling OFCDM with Alternative Spreading Code

OFCDM has received large attention as a modulation scheme to realize high data rate transmission. On the other hand, FS is a diversity scheme with a single antenna, which achieves path diversity through oversampling and parallel signal demodulation. In this section, the OFCDM system with FS is investigated. FS causes correlation among noise components as the sampling rate is higher than the Nyquist rate. This correlation may deteriorate the BER performance at the receiver as the number of subcarriers and oversampling ratio increase. To overcome this problem, correlated noise cancellation scheme in FS OFCDM system is

discussed in this section.

4.1.1 Introduction

OFCDM has received large attention as a modulation scheme to realize high data rate transmission, which is based on code division multiple access (CDMA) [4.1]-[4.3]. The OFCDM system transmits signals using more than 1000 subcarriers that are orthogonally overlapped in the frequency domain.

On the other hand, various diversity schemes have been actively investigated for the OFCDM-based system [4.4][4.5]. One of the typical diversity schemes is antenna diversity in which multiple antenna elements are implemented in the receiver [4.4]. However, it may be difficult to implement multiple antenna elements in small devices. Therefore, a new diversity scheme called FS has been proposed in [4.6]. This scheme tries to acquire diversity gain through the signal sampled faster than the Nyquist rate in the receiver. FS is known to covert a single-input single-output (SISO) channel into a single-input multiple-output (SIMO) channel. In [4.6], subcarrier-based noise whitening and MRC have been investigated because of their low complexity. However, as the number of subcarriers and the oversampling ratio increase, the correlation among the noise components over different subcarriers deteriorates the BER performance.

To solve this problem, an OFCDM system with the alternative spreading code is investigated. This spreading code has positive and negative components alternatively. Therefore, the OFCDM system with the alternative spreading code can cancel the correlated noise components. The performance of the FS OFCDM system with the alternative spreading code is evaluated through computer simulation in this section.

Firstly, a system model is described briefly in subsection 4.1.2. The signal processing of the proposed scheme for the FS OFCDM system is then discussed in subsection 4.1.3. Numerical results are shown in subsection 4.1.4. Finally, conclusions are presented in subsection 4.1.5.

4.1.2 System Model

4.1.2.1 Transmitter Model

Figure 4.1 shows the block diagram of an OFCDM transmitter [4.1][4.2]. The input data is modulated with QPSK and is serial-to-parallel (S/P) converted to N/S_f parallel sequences, where N denotes the number of subcarriers and S_f denotes the spreading factor in the frequency domain. Each modulated symbol is duplicated

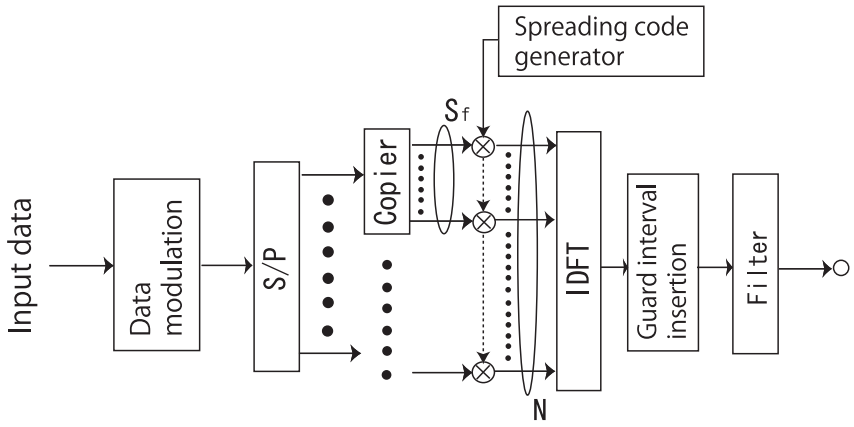

Figure 4.1: OFCDM transmitter block diagram.

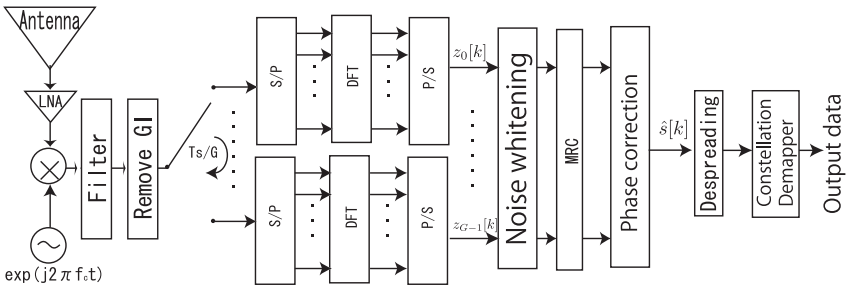

Figure 4.2: Receiver block diagram.

into S_f parallel copies. Each branch of the symbol stream is then multiplied by a chip from the spreading code with the repetition period of S_f, which is represented as

$$\begin{aligned} &s[(x-1)S_f + i] = d[x]q_i, \\ &1 \leq x \leq N/S_f, \quad 0 \leq i \leq S_f - 1, \end{aligned} \tag{4.1}$$

where $s[(x-1)S_f + i]$ is the i-th spread data component of the x-th data symbol transmitted over the $[(x-1)S_f]$-th subcarrier, and $d[x]$ is the x-th data symbol, and q_i is the i-th spreading code. The spread data sequence is modulated to the multi-carrier signal by IDFT, and the GI is inserted to the modulated signal.

4.1.2.2 Receiver Structure with Fractional Sampling

At the receiver side, FS and MRC are used to achieve diversity over a multipath channel [4.6]. The block diagram of an OFCDM receiver with FS is shown in Fig.

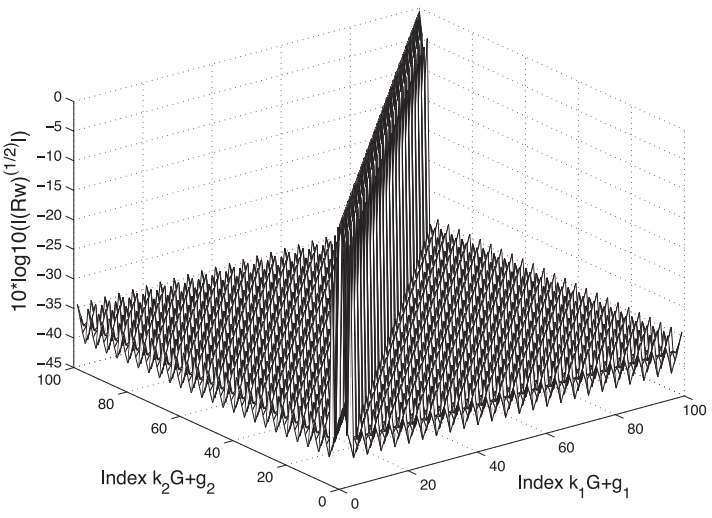

Figure 4.3: Correlation of the noise components (logarithmic representation of absolute value).

4.2. The received signal is downconverted to baseband and fractionally sampled. The sampled signals are separated to G branches. The GI is removed on each of the branches. The samples are serial-parallel converted and put into DFT. The outputs of the DFT are then parallel-to-serial (P/S) converted. The signals on all G branches are put into the whitening filter as the noise components of the fractionally sampled signals are correlated. The output of the whitening filter are then combined together as mentioned in subsection 1.4.3. The combined signal is despread and demodulated, which is represented as

$$\hat{d}[x] = \sum_{i=0}^{S_f-1} \hat{s}[(x-1)S_f + i]q_i. \tag{4.2}$$

In FS system, the received signal is sampled at a rate higher than the Nyquist rate in order to acquire the diversity gain. As the sampling rate G increases, G OFDM demodulators are required. The computational complexity is increased by a factor G as compared to usual OFDM system. In addition, the covariance matrix is required for noise whitening.

4.1.3 Proposed Scheme

4.1.3.1 Despreading with Non-alternative Spreading Code

Suppose that the spreading code with the following condition is employed.

$$q_i = q_{i+1} = \cdots = q_{i+S_f-1}. \tag{4.3}$$

From Eq. (1.42) in Chapter 1, the correlated noise after despreading from the k-th to the $(k+S_f-1)$-th subcarriers, $\gamma_{\mathbf{non}}[k, k+S_f-1]$, is expressed as

$$\begin{aligned}
& \gamma_{\mathbf{non}}[k, k+S_f-1] \\
= & \sum_{k_1=k}^{S_f+k-1} (\sum_{g_1=0}^{G-1} \sum_{\substack{k_2=0 \\ k_2 \neq k_1}}^{N-1} \sum_{g_2=0}^{G-1} H'_{g_1}[k_1][\mathbf{R}_n[k_1, k_2]]_{g_1,g_2} \omega_{g_2}[k_2]) \\
= & \sum_{g_1=0}^{G-1} \sum_{\substack{k_2=0 \\ k_2 \neq k_1}}^{N-1} \sum_{g_2=0}^{G-1} (H'_{g_1}[k][\mathbf{R}_n[k, k_2]]_{g_1,g_2} \\
& + H'_{g_1}[k+1][\mathbf{R}_n[k+1, k_2]]_{g_1,g_2} + \cdots + \\
& H'_{g_1}[k+S_f-1][\mathbf{R}_n[k+S_f-1, k_2]]_{g_1,g_2}) \omega_{g_2}[k_2].
\end{aligned} \tag{4.4}$$

The correlation among the noise components, $\mathbf{R}_w^{\frac{1}{2}}$, over the subcarriers and oversampling indexes ($k_1 G + g_1 \leq 100$, $k_2 G + g_2 \leq 100$) is shown in Fig. 4.3, where the non-diagonal elements of this matrix are almost periodic over the neighboring indexes. Moreover, from Eq. (1.36), if the number of subcarriers increases and the spreading factor is small enough, the following approximation on the noise covariance matrices can be assumed.

$$\mathbf{R}_w^{-\frac{1}{2}}[k] \approx \mathbf{R}_w^{-\frac{1}{2}}[k+1] \approx \cdots \approx \mathbf{R}_w^{-\frac{1}{2}}[k+S_f-1]. \tag{4.5}$$

Thus, from Eqs. (4.5),

$$\begin{aligned}
[\mathbf{R}_n[k, k_2]]_{g_1,g_2} & \approx [\mathbf{R}_n[k+1, k_2]]_{g_1,g_2} \\
& \approx \cdots \approx [\mathbf{R}_n[k+S_f-1, k_2]]_{g_1,g_2}.
\end{aligned} \tag{4.6}$$

If the correlation of the channel responses of the subcarriers is high, the following approximation is also derived.

$$H'_{g_1}[k] \approx H'_{g_1}[k+1] \approx \cdots \approx H'_{g_1}[k+S_f+1]. \tag{4.7}$$

From Eqs. (4.6) and (4.7), the correlated noise after despreading can be approximated as follows.

$$\begin{aligned}
& \gamma_{\mathbf{non}}[k, k+S_f-1] \\
\approx & \sum_{g_1=0}^{G-1} \sum_{\substack{k_2=0 \\ k_2 \neq k_1}}^{N-1} \sum_{g_2=0}^{G-1} S_f (H'_{g_1}[k][\mathbf{R}_n[k, k_2]]_{g_1,g_2}) \omega_{g_2}[k_2].
\end{aligned} \tag{4.8}$$

If the size of the matrix and the spreading factor increases, the total amount of the correlated noise in Eq. (1.42) grows. Therefore, the BER performance is deteriorated with the correlated noise component.

4.1.3.2 Despreading with Alternative Spreading Code

If the number of the subcarriers and the oversampling ratio increase, the total amount of the correlated noise in Eq. (1.42) grows. To solve this problem, a spreading code which has the following property is used.

$$q_{2i} = -q_{2i+1}, \qquad i = 0, 1, \cdots, S_f/2 - 1. \tag{4.9}$$

This code is referred to as the alternative spreading code in this section. From Eqs. (1.27) and (4.6), the correlated noise is approximated as

$$\begin{aligned} & \gamma_{\mathbf{alt}}[k, k+S_f-1] \\ = & \sum_{k_1=k}^{S_f+k} \sum_{g_1=0}^{G-1} \sum_{\substack{k_2=0 \\ k_2 \neq k_1}}^{N-1} \sum_{g_2=0}^{G-1} q_{(k_1-k)} H'_{g_1}[k_1] \cdot [\mathbf{R}_n[k_1, k_2]]_{g_1,g_2} \omega_{g_2}[k_2]. \end{aligned} \tag{4.10}$$

From Eqs. (4.7), (4.9), and (4.10), the correlated noise after despreading from the k-th to $(k+S_f-1)$-th subcarriers, $\gamma_{\mathbf{alt}}$, is given as

$$\begin{aligned} & \gamma_{\mathbf{alt}}[k, k+S_f-1] \\ \approx & \sum_{k_1=k}^{S_f+k} \sum_{g_1=0}^{G-1} H'_{g_1}[k] \cdot \sum_{\substack{k_2=0 \\ k_2 \neq k_1}}^{N-1} (-1)^{(k-k_1)} \{ \sum_{g_2=0}^{G-1} [\mathbf{R}_n[k_1, k_2]]_{g_1,g_2} \omega_{g_2}[k_2] \}. \end{aligned} \tag{4.11}$$

The inside of the braces in Eq. (4.11) cancels between the k_1-th and (k_1+1)-th subcarriers because of the element, $(-1)^{(k-k_1)}$. This element is based on the property of the alternative spreading code given in Eq. (4.9) Thus, despreading with the alternative spreading code cancels most of the correlated noise components. However, the drawback of this scheme is that the number of available spreading codes reduces to half. This is also due to the constraint shown in Eq. (4.9).

4.1.4 Numerical Results

4.1.4.1 Simulation Conditions

The FS OFCDM system with the alternative spreading code is evaluated through computer simulation. Simulation conditions are shown in Table 4.1, which assume

Table 4.1: Simulation conditions.

Bandwidth	80MHz
Number of subcarriers	256/512/1024
Guard Interval	12.8/25.6/51.2[μsec]
Subcarrier spacing Δf	78.1/39.1/19.5 [kHz]
Number of IDFT points	256/512/1024
DFT sampling speed T_s	12.5 [nsec]
Data modulation	QPSK
Channel estimation	Ideal
Fractional sampling ratio G	1,2,4
Spreading factor S_f	2/4/8/16
Channel model	Rayleigh fading 16 path uniform/24 path exponential

the 4G system is assumed. The data is modulated with QPSK. The received signal is sampled at the rates of $1/T_s$, $2/T_s$, and $4/T_s$. The spreading factor, S_f, is set from 2 to 16 in this simulation. Channel estimation is assumed to be ideal. Here, two channel models are considered. One is a 16 path Rayleigh fading model with a uniformed delay profile as shown in Fig. 4.5(a) [4.6]. The interval between the path delays in this model is $T_s/4$. The other one is a 24 path Rayleigh fading model with an exponential delay profile as shown in Fig. 4.5(b) [4.2]. The interval between the path delays is $5T_s$. The composite impulse response of the transmit and receive pulse shaping filters is assumed to be a sinc pulse with a duration of $2T_s$ [4.6]. Fig. 4.4 shows the frequency response of the pulse shaping filters with the impulse response of the rectangular pulse and the truncated sinc pulse. If the rectangular pulse is applied, the non-diagonal elements of $\mathbf{R}_w^{1/2}$ equal to 0, which means no correlated noise components. Therefore, the BER performance with the rectangular pulse is equivalent to that of a SIMO model [4.7].

4.1.4.2 BER Improvement with Alternative Spreading Code

Figures 4.6 and 4.7 show the BER performance of the 16 and 24 path Rayleigh fading channel models, respectively. The number of subcarriers is 1024 and the spreading factor is 2. Numerical results of the 1×4 SIMO model are shown in the same figure as a reference. This SIMO model is assumed to receive uncorrelated signals at each antenna.

From these figures, when the oversampling ratio is 1 or 2, the BERs with both alternative and non-alternative spreading codes are almost the same. On the other

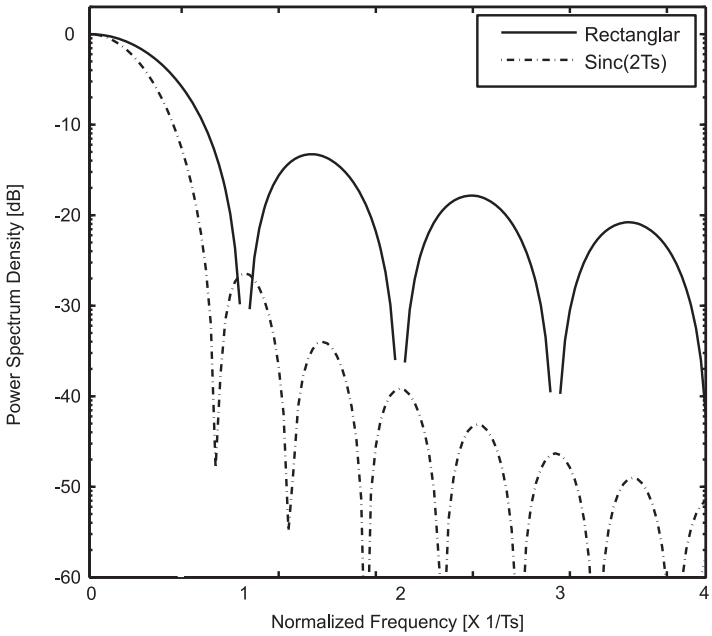

Figure 4.4: PSD vs. normalized frequency with different pulse shapes.

hand, if the oversampling ratio is 4, the BER with the non-alternative spreading code is larger than that with the oversampling ratio of 2. This is due to the correlated noise components in Eq. (1.42). On the contrary, the BER with the alternative spreading code reduces as the oversampling ratio increases. This is because the alternative spreading code cancels the correlated noise components among the adjacent subcarriers as shown in Eq. (4.11). In Fig. 4.7, the improvement on the BER curve is limited in comparison with Fig. 4.6. The reason is that the delay spread assumed in the exponentially decay model is larger. Therefore, the fluctuation on the channel responses among the adjacent subcarriers is larger and the approximation in Eq. (4.7) becomes inaccurate. Thus, the residual component of the correlated noise after despreading limits the improvement of the BER performance.

4.1.4.3 Number of Subcarriers

In Figs. 4.8 and 4.9, the relationship between the BER and the number of subcarriers for both alternative and non-alternative spreading codes is presented. Here, E_b/N_0 is set to 15[dB], the spreading factor is set to 2, and the oversampling ratio is set to $G = \{1, 2, 4\}$. In Fig. 4.9, the BERs are deteriorated when the number

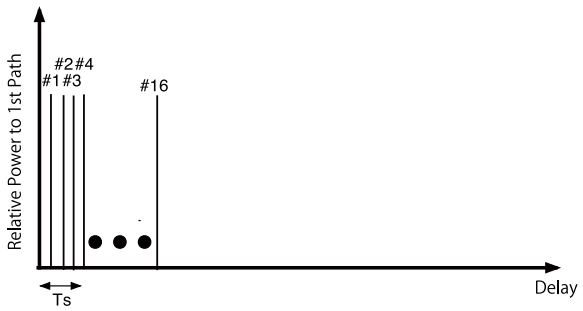

(a) 16 path Rayleigh fading model with uniform delay spread.

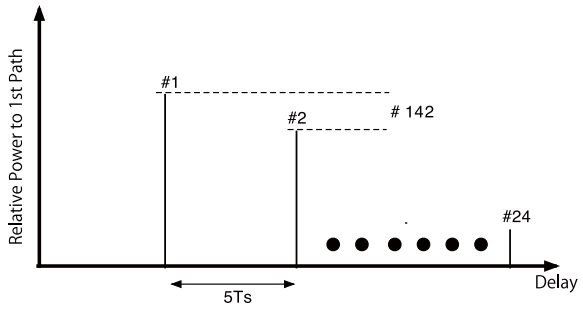

(b) 24 path Rayleigh fading model with exponential delay spread.

Figure 4.5: Multipath channel models.

of subcarriers is 256. This is because the delay spread is large on the 24 path Rayleigh fading channel and some of the paths have larger delays than the GI. When the number of subcarriers is more than 512, the largest delay of the paths is accommodated within the GI. In both figures, the BERs of $G = \{1, 2\}$ remain fairly constant. As the number of subcarriers increases, the BER with the non-alternative spreading code increases when $G = 4$ and the number of subcarriers is 1024. This is because of the correlated noise components between the adjacent subcarriers. The reason is that the value of the element in $\mathbf{R}_n[k, j]$ in Eq. (1.41) is of the order of 10^{-4} and the total amount of the correlated noise components becomes close to that of the white noise.

4.1.4.4 Spreading Factor S_f

In Figs. 4.10 and 4.11, the relationship between the BER and the spreading factor for both alternative and non-alternative spreading codes on different channel models is presented. Here, E_b/N_0 is set to 15[dB] and the oversampling ratio is set to $G = \{1, 2, 4\}$. The number of subcarriers is 1024. In Fig. 4.10, the BERs with $G = \{1, 2\}$ remain fairly constant. As the spreading factor increases, the

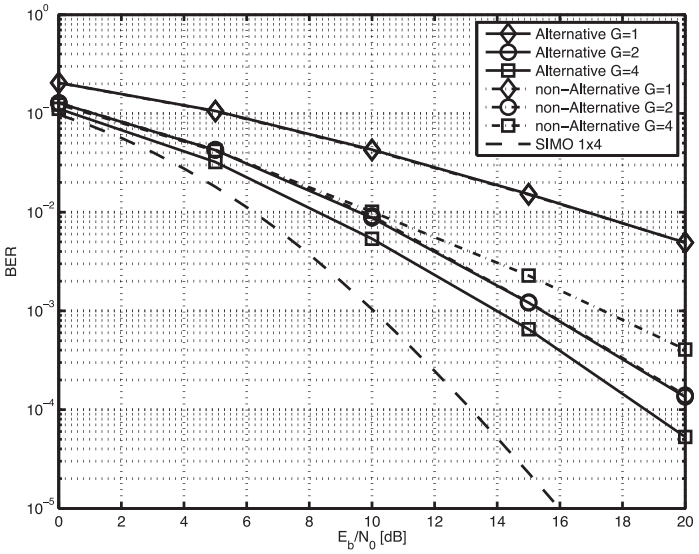

Figure 4.6: BER performance vs. E_b/N_0 on the 16 path Rayleigh fading channel with the uniform delay profile (number of subcarriers: 1024, S_f=2).

Table 4.2: Spreading code.

1st low	1	1	1	1	1	1	1	1	1	1	1	1	1	1	1	1
2nd low	1	-1	1	-1	1	-1	1	-1	1	-1	1	-1	1	-1	1	-1
3rd low	1	1	-1	-1	1	1	-1	-1	1	1	-1	-1	1	1	-1	-1
5th low	1	1	1	1	-1	-1	-1	-1	1	1	1	1	-1	-1	-1	-1
9th low	1	1	1	1	1	1	1	1	-1	-1	-1	-1	-1	-1	-1	-1

BER with the alternative spreading code decreases when $G = 4$. This is due to the effect of frequency diversity. In contrast, when $G = 4$, the BER with the non-alternative spreading code is deteriorated as the spreading factor increases. The reason behind is the correlated noise given in Eq. (4.8). If the spreading factor, S_f, increases, the variance of the noise also grows with the factor of ${S_f}^2$. As for the results corresponding to the alternative spreading code, the BER is improved as the spreading factor increases. This is because the alternative spreading code can cancel the correlated noise. More diversity gain is obtained with the proposed spreading code in Fig. 4.11. This is due to the assumed channel model. Since the delay spread assumed in the exponential delay model is larger than that in the uniform decay model, the correlation among the channel responses of the subcarriers

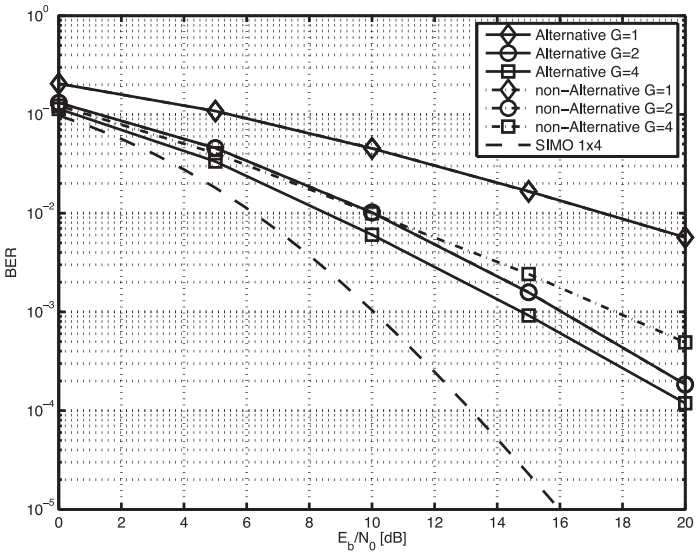

Figure 4.7: BER performance vs. E_b/N_0 on the 24 path Rayleigh fading channel with the exponential delay profile (number of subcarriers: 1024, S_f=2).

is smaller in Fig. 4.11.

4.1.4.5 Spreading Code

In order to show the validity of the alternative spreading code, the relationship between the BER and G for various spreading codes on the two different channel models is presented in Figs. 4.12 and 4.13. Here, E_b/N_0 is set to 15[dB] and the number of subcarriers is 1024. The 1st, 2nd, 3rd, 5th, and 9th rows of the Walsh-Hadamard matrix with the size of 16 are used as the spreading codes [4.2]. Table 4.2 shows the spreading code used in this simulation. The 2nd row corresponds to the proposed alternative spreading code. Both Figs. 4.12 and 4.13 show that BERs with $G = \{1, 2\}$ are almost the same for all spreading codes. Moreover, the figures also show that the alternative spreading code gives the best result when $G = 4$ while the worst result is given by the 1st row (non-alternative spreading code). The results with the other codes (3rd, 5th, 9th) are spread between them. The reason is that the pair of the blocks of "1" and "-1" in the spreading code cancels the correlated noise components if the channel responses corresponding to those blocks are sufficiently close. As the size of the block reduces, the difference between the corresponding channel responses in those blocks decreases and the

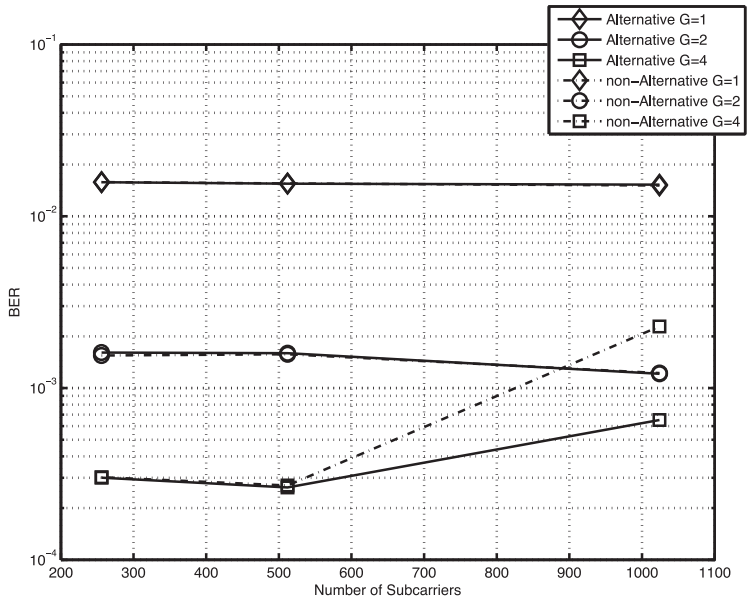

Figure 4.8: BER performance vs. number of subcarriers on the 16 path Rayleigh fading channel with the uniform delay profile ($S_f = 2$, $E_b/N_0 = 15$[dB]).

residual of the correlated noise components diminishes.

4.1.5 Conclusions

The FS OFCDM system with the alternative spreading code has been investigated in this section. In the FS OFCDM system, the correlation between the noise components may deteriorate the BER performance at the receiver with the increase of the number of subcarriers and oversampling ratio. The proposed spreading code mitigates the effect of the correlated noise components and improves the BER performance, especially when the oversampling rate is 4. It has also been shown that the FS OFCDM system with the alternative spreading code can obtain frequency diversity effect.

4.2 Effect of Pulse Shaping Filters on a Fractional Sampling OFDM System with Subcarrier-Based Maximal Ratio Combining

In this section, the effect of the impulse response of pulse shaping filters on a FS OFDM system is investigated. FS achieves path diversity with a single antenna

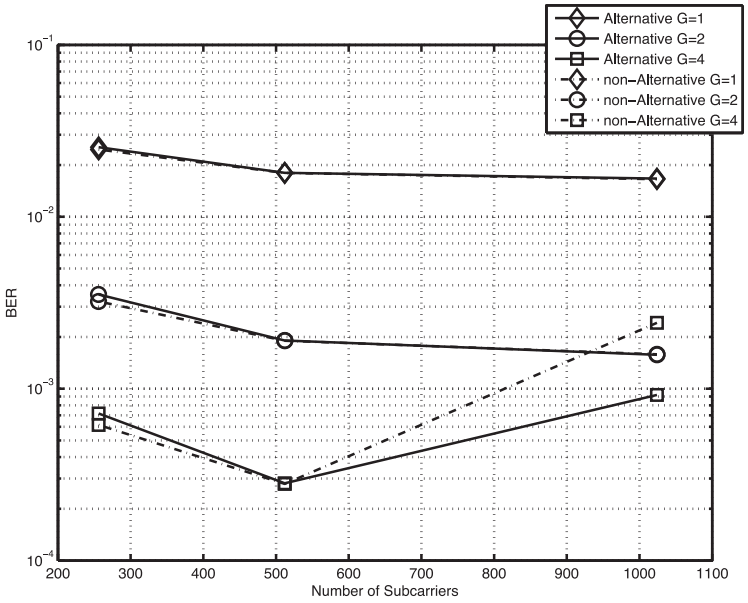

Figure 4.9: BER performance vs. number of subcarriers on the 24 path Rayleigh fading channel with the exponential delay profile ($S_f = 2$, $E_b/N_0 = 15$[dB]).

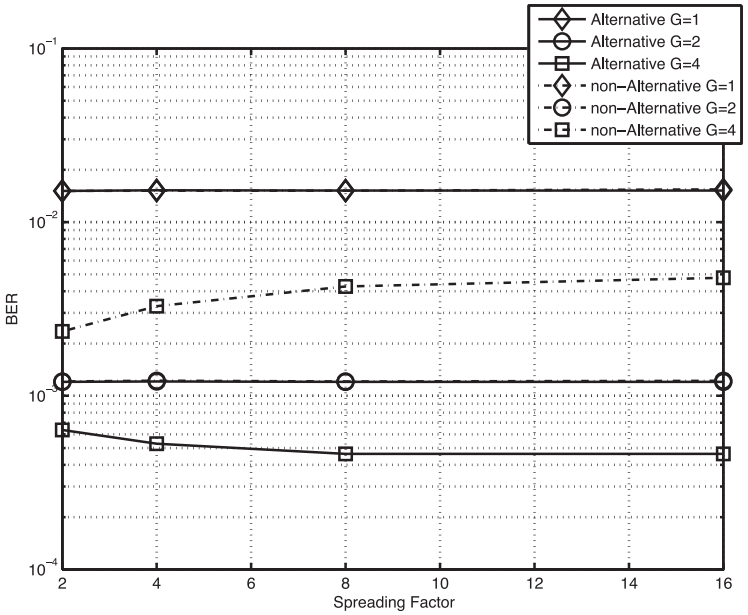

Figure 4.10: BER performance vs. spreading factor S_f on the 16 path Rayleigh fading channel with the uniform delay profile (number of subcarriers:1024, $E_b/N_0 = 15$[dB]).

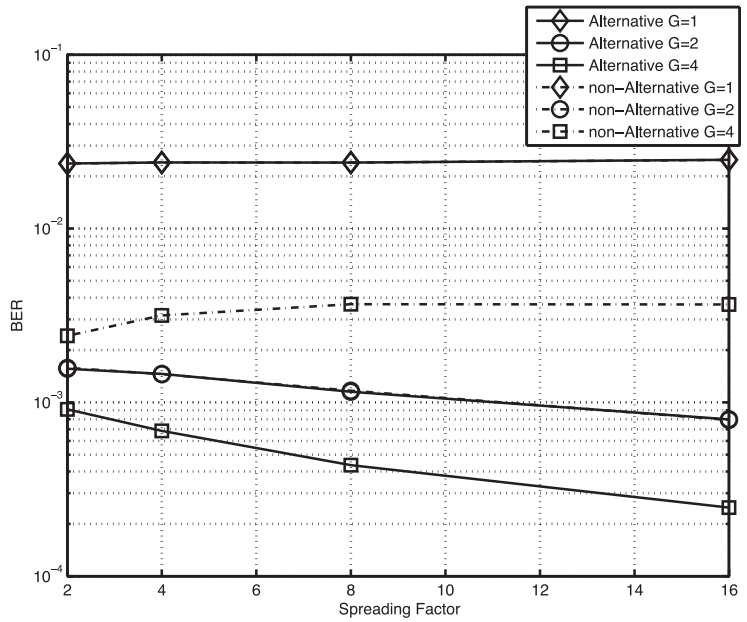

Figure 4.11: BER performance vs. spreading factor S_f on the 24 path Rayleigh fading channel with the exponential delay profile (number of subcarriers:1024, $E_b/N_0 = 15$[dB]).

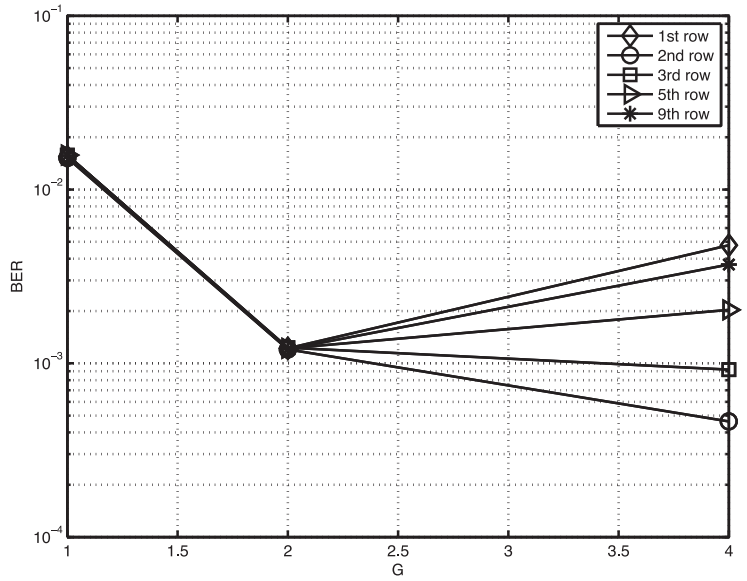

Figure 4.12: BER performance vs. G with different spreading codes on the 16 path Rayleigh fading channel with the uniform delay profile (number of subcarriers:1024, $E_b/N_0 = 15$[dB]).

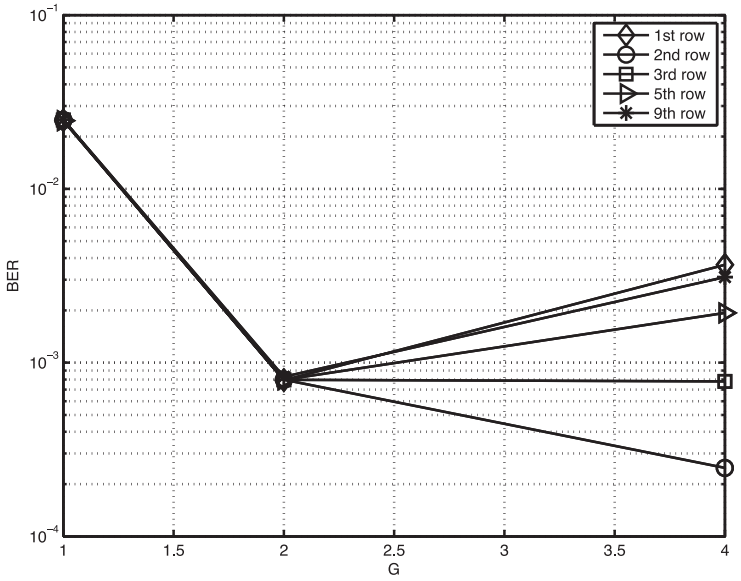

Figure 4.13: BER performance vs. G with different spreading codes on the 24 path Rayleigh fading channel with the exponential delay profile (number of subcarriers:1024, $E_b/N_0 = 15$[dB]).

through oversampling and subcarrier-based MRC. Though the oversampling increases diversity order, correlation among noise components may deteriorate BER performance. To clarify the relationship between the impulse response of the pulse shaping filter and the BER performance, five different pulse shaping filters are evaluated in the FS OFDM system. The metric adjustment based on the Frobenius norm is also evaluated in the coded FS OFDM system.

4.2.1 Introduction

As mentioned in Chapter 1, though the oversampling increases diversity order, correlation among noise components in FS OFDM system may deteriorate BER performance. In order to solve this problem, the frequency spreading scheme for OFCDM has been proposed in section 4.1 [4.9]. This scheme cancels the correlated noise components among adjacent subcarriers and improves the BER performance. However, the proposed scheme reduces the number of available spreading codes. Moreover, this scheme is not applicable to OFDM systems. Since the noise passes through the pulse shaping filter (baseband filter) in the receiver, the impulse response of the filter determines the correlation among the noise components. In order to prevent the BER degradation due to the correlated noise components without spreading codes, impulse responses of the pulse shaping filter are evalu-

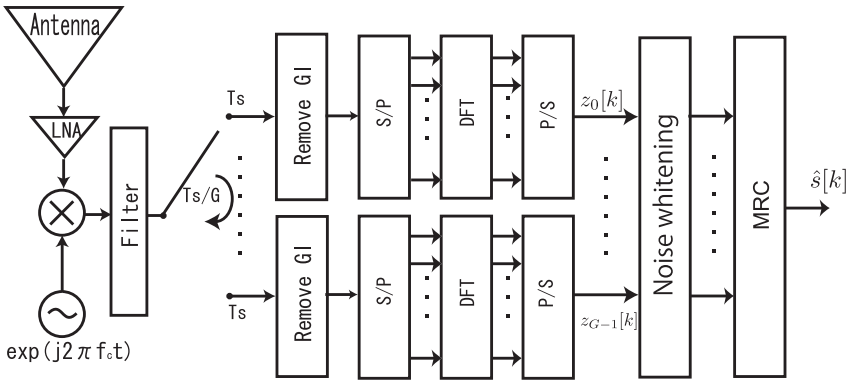

Figure 4.14: Block diagram of a receiver.

ated for the FS OFDM system in this section. The effect of the impulse response of the filter on the BER performance is then clarified.

This section is organized as follows. Firstly, a system model is described briefly in subsection 4.2.2. The correlation among the noise components is then discussed in subsection 4.2.3. Numerical results are shown in subsection 4.2.4. Finally, conclusions are presented in subsection 4.2.5.

4.2.2 Receiver Structure with Fractional Sampling

At the receiver side, FS and MRC are used to achieve diversity over a multipath channel [4.6]. The block diagram of an OFDM receiver with FS is shown in Fig. 4.14.

4.2.3 Noise Correlation among Samples

As mentioned in Chapter 1, the second term of the right side of Eq. (1.42) gives the correlation between the noise components after subcarrier based noise whitening. These components may deteriorate the BER performance of the receiver. The correlation among the noise components is determined by the impulse response of the filter because the noise passes through the pulse shaping filter. An example of the correlation among the noise components, $\mathbf{R}_w^{\frac{1}{2}}$, over the subcarriers and oversampling indexes ($k_1G + g_1 \leq 100$, $k_2G + g_2 \leq 100$) is shown in Fig. 4.15. A sinc pulse is assume as the impulse response of the pulse shaping filter. From Eq. (1.36), this is the function of the impulse response of the pulse shaping filter in the receiver. In order to improve the BER performance, the Frobenius norm of $\mathbf{R}_n[k_1, k_2]$ should be kept small. Here, the Frobenius norm of a matrix $\mathbf{A}$ is given

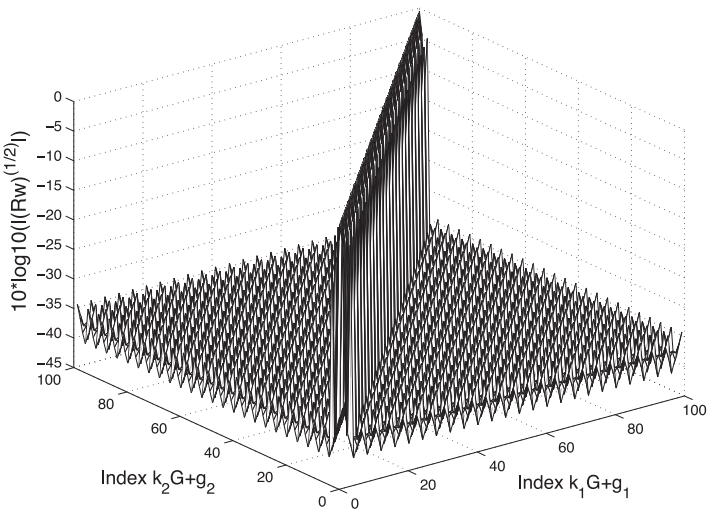

Figure 4.15: Correlation of the noise components (logarithm representation of absolute value).

as

$$||\mathrm{A}||_F = \sqrt{\sum_{g_1=0}^{G-1}\sum_{g_2=0}^{G-1}([\mathbf{A}]_{g_1,g_2})^2} \tag{4.12}$$

where $||\cdot||_F$ denotes the Frobenius norm [4.10].

From Eq. (1.41), $\mathbf{R}_n[k_1,k_2]$ is given as follows.

$$\mathbf{R}_n[k_1,k_2] = \mathbf{R}_w^{-\frac{1}{2}}[k_1]\mathbf{R}_w^{\frac{1}{2}}[k_1,k_2], \tag{4.13}$$

where $\mathbf{R}_w^{\frac{1}{2}}[k_1,k_2]$ is the (k_1,k_2)-th subblock of $\mathbf{R}_w^{\frac{1}{2}}$. The distribution of the eigenvalues for particular types of matrices has been investigated, especially for MIMO transmission [4.11][4.12]. However, the distribution is not given for general matricies. Since $\mathbf{R}_w^{\frac{1}{2}}[k_1,k_2]$ does not have a specific matrix structure, the eigenvalues of $\mathbf{R}_w^{\frac{1}{2}}[k_1,k_2]$ are not able to be analysed. On the other hand, since $\mathbf{R}_w^{\frac{1}{2}}[k_1]$ is a Hermitian matrix and positive semidefinite, the Frobenius norm of the whitening matrix, $\mathbf{R}_w^{-\frac{1}{2}}[k_1]$, is given by

$$||\mathbf{R}_w^{-\frac{1}{2}}[k_1]||_F^2 = \sum_{g=0}^{G-1}(1/\lambda_g[k_1])^2, \tag{4.14}$$

where $\lambda_g[k_1]$ is the g-th eigenvalue of $\mathbf{R}_w^{\frac{1}{2}}[k_1]$ [4.10]. Also, $||\mathbf{R}_w[k_1]||_F^2 = \sum_{g=0}^{G-1}(\lambda_g[k_1])^4$.

Table 4.3: Simulation conditions

Bandwidth	80MHz
Number of data subcarriers	48/768
Guard interval	0.2/3.2[μsec]
Subcarrier spacing Δf	1250/78.1 [kHz]
Number of IDFT points	64/1024
DFT sampling speed T_s	12.5 [nsec]
Data modulation	QPSK, 16QAM, 64QAM/OFDM
Channel estimation	Ideal
Fractional sampling ratio G	1,2,4
Channel model	Rayleigh fading (16path uniform/24path exponential) GSM Typical urban model
Channel coding	Convolutional code ($R = 1/2$, $K = 7$)
Channel decoding	Soft decision Viterbi decoder

From Eq. (1.36), the (g_1, g_2)-th element of $\mathbf{R}_w[k_1]$ is given as

$$\begin{aligned} & [\mathbf{R}_w[k_1]]_{g_1,g_2} \\ = \; & \sigma_v^2 \frac{1}{N} \sum_{n_d=-N+1}^{N-1} (N - |n_d|) p_2((n_d + (g_2 - g_1)/G)T_s) \\ \times \; & e^{-j\frac{2\pi k n_d}{N}}. \end{aligned} \tag{4.15}$$

From Eqs. (4.12), (4.14) and (4.15), the inverse of the Frobenius norm of $\mathbf{R}_w^{-\frac{1}{2}}[k_1]$ is related to the specturm of the composite response, $p_2(t)$, because of the term, $p_2((n_d + (g_2 - g_1)/G)T_s)e^{-j\frac{2\pi k n_d}{N}}$, which is the same as the one in the discrete Fourier transform. Therefore, in this section, the Frobenius norm of the whitening matrix for five different impulse responses of the pulse shaping filter is investigated through computer simulation.

4.2.4 Numerical Results

4.2.4.1 Simulation Conditions

Simulation conditions are shown in Table 4.3, which assumes the 4G system. The data is modulated with QPSK, 16QAM, and 64QAM, and multiplexed with OFDM. The bandwidth of the OFDM system is 80MHz. The DFT size is 64 and 1024 while the number of data subcarriers is 48 and 768. The received signal is

Table 4.4: 6-ray GSM Typical Urban model parameters.

Tap number	Relative time (μs)	Average relative power (dB)	Delay in samples
1	0.0	-3.0	0
2	0.2	0.0	3
3	0.5	-2.0	8
4	1.6	-6.0	25
5	2.3	-8.0	35
6	5.0	-10.0	77

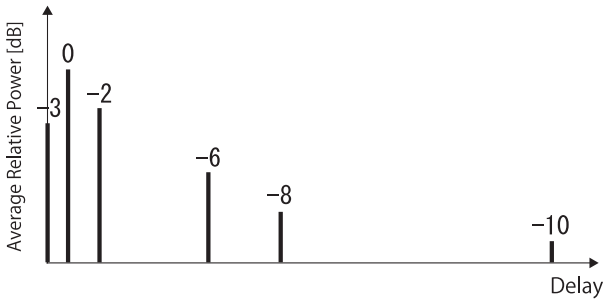

Figure 4.16: 6-ray GSM Typical Urban model.

sampled at the rates of $1/T_s$, $2/T_s$, and $4/T_s$ ($G = 1, 2, 4$). As channel coding, a convolutional code with a coding rate of $1/2$ is used. Soft decision Viterbi decoding is employed in the receiver.

4.2.4.2 Channel Models

In this section, three channel models are assumed in the simulation. One is 6-ray GSM Typical Urban model. The 6-ray GSM Typical Urban model is one of the propagation models that are mentioned in the main body of 3GPP TS 45.005. The parameters of the 6-ray GSM Typical Urban model is defined in Table 4.4. Fig. 4.16 shows the delay profile of 6-ray GSM Typical Urban model. The amplitude of the path follows Rayleigh distribution. The others are Rayleigh fading channel models. A 16 path Rayleigh fading model with an uniformed delay profile is shown in Fig. 4.17(a) [4.6]. The interval between the path delays in this model is $T_s/4$. A 24 path Rayleigh fading model with an exponential delay profile is shown in Fig. 4.17(b) [4.2]. The interval between the path delays is $5T_s$. The channel response is assumed to be constant during one OFDM symbol interval. The GSM model

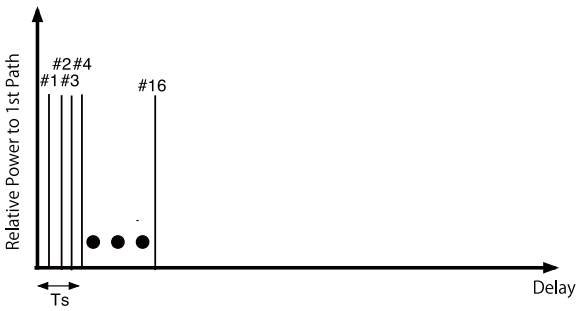

(a) 16 path Rayleigh fading model with uniform delay spread.

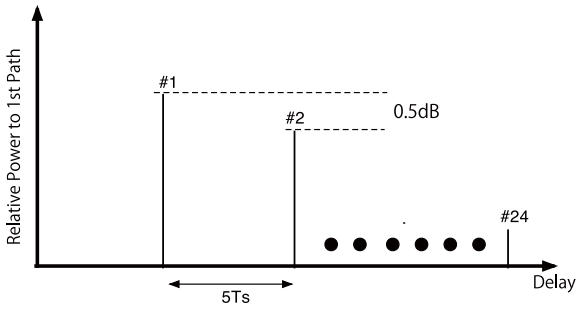

(b) 24 path Rayleigh fading model with exponential delay spread.

Figure 4.17: Multipath Rayleigh fading channel models.

and 24 path Rayleigh fading model are applied to the OFDM system with 1024 subcarriers.

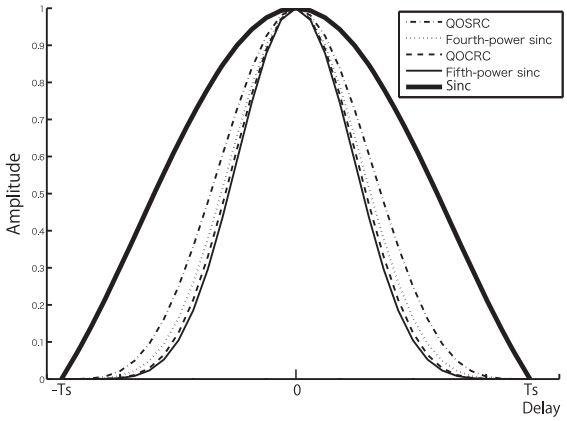

(a) Impulse responses of the pulse shaping filter.

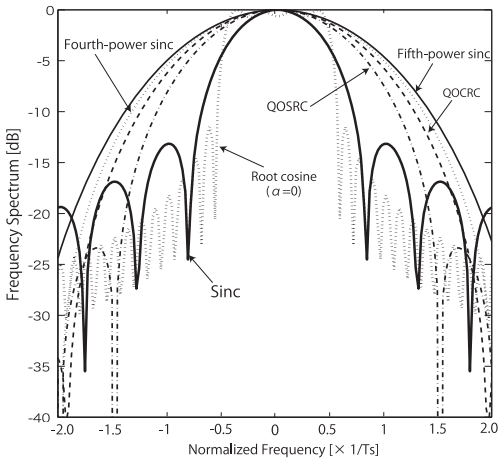

(b) Frequency spectrums of the pulse shaping filter.

Figure 4.18: Graphical illustration of the pulse shaping filters.

4.2.4.3 Pulse Shaping Filters

To clarify the effect of the spectrum of the filter on the BER performance, the pulse shaping filter with the following 5 different impulse responses are employed both at the transmitter and the receiver [4.6][4.13]. These impulse responses have different bandwidths and are classified into two different types of sinc-based and cosine-based pulse shaping filters [4.14].

Sinc-based pulse shaping filter

1. Sinc pulse truncated to $[-T_s,T_s]$, ξ=0.64 is given by

$$p(t) = \text{sinc}(\frac{t}{T_s})\text{rect}(\frac{t}{2T_s}). \tag{4.16}$$

2. Fourth-power sinc pulse over $[-T_s,T_s]$, $\xi = 0.164$ is given by

$$p(t) = \text{sinc}^4(\frac{t}{T_s})\text{rect}(\frac{t}{2T_s}). \tag{4.17}$$

3. Fifth-power sinc pulse truncated to $[-T_s,T_s]$, $\xi = 0.1046$ is given by

$$p(t) = \text{sinc}^5(\frac{t}{T_s})\text{rect}(\frac{t}{2T_s}). \tag{4.18}$$

Cosine-based pulse shaping filter

1. Quadrature overlapped cubed raised cosine (QOCRC) pulse truncated to $[-T_s,T_s]$, $\xi = 0.125$ is given by

$$p(t) = \cos^4(\frac{\pi t}{2T_s})\text{rect}(\frac{t}{2T_s}). \tag{4.19}$$

2. Quadrature overlapped squared raised cosine (QOSRC) pulse truncated to $[-T_s,T_s]$, ξ=0.25 is given by

$$p(t) = \cos^6(\frac{\pi t}{2T_s})\text{rect}(\frac{\pi t}{2T_s}). \tag{4.20}$$

Here, ξ represents the scaling effect on the received signal samples due to the pulse shape at the offset sampling instants of $\pm T_s/2$. The impulse responses and the frequency responses of the pulse shaping filter are shown in Figs. 4.18(a) and 4.18(b). As a reference, a root cosine roll-off filter (roll-off factor $a = 0$) with the duration of $\pm 4T_s$ is shown in Fig. 4.18(b). In this case, as suggested in [4.6], no diversity gain is obtained because of the sharp frequency response of the filter.

4.2.4.4 Frequency Spectrum of the Filter and Frobenius Norm of the Whitening Matrix

Figures 4.19 and 4.20 show the Frobenius norm of the whitening matrix, $\mathbf{R}_w^{-\frac{1}{2}}[k_1]$, with different impulse responses of the pulse shaping filter. Here, the number of subcarriers is 64 and the oversampling ratio is set to $G = \{2, 4\}$. As it is suggested with Eq. (4.15), there is a relationahip between the spectrum of the filter and the Frobenius norm (though it is not exactly the same as the spectrum of the

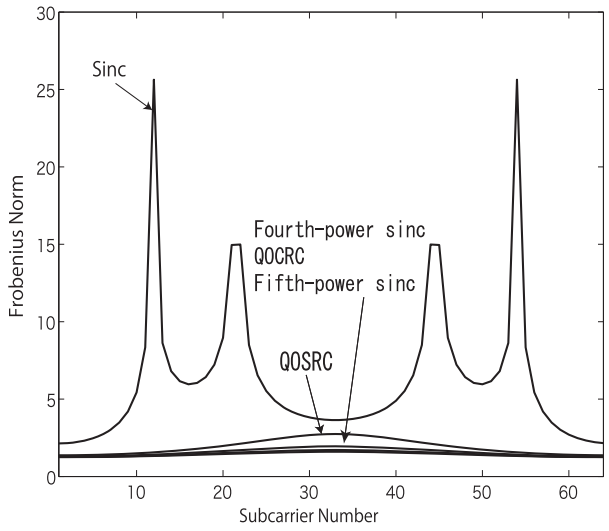

Figure 4.19: Frobenius norm of the whitening filter for different impulse responses (Number of subcarriers=64, $G = 2$).

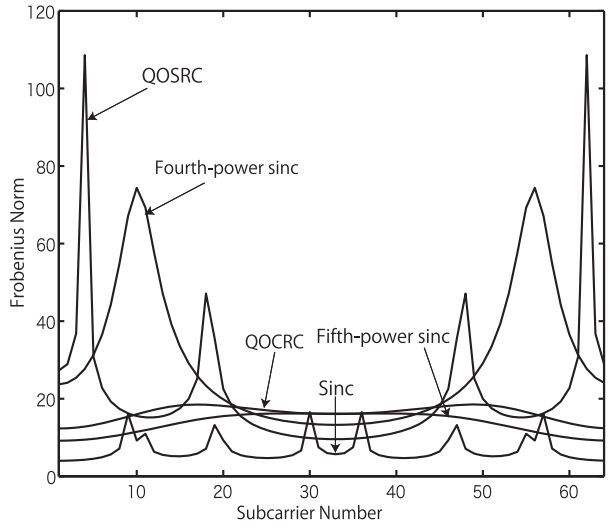

Figure 4.20: Frobenius norm of the whitening filter for different impulse responses (Number of subcarriers=64, $G = 4$).

filter due to the weighting term $(N - |n_d|)$). The number of dip points in the spectrum is proportional to the number of peak points in the Frobenius norm.

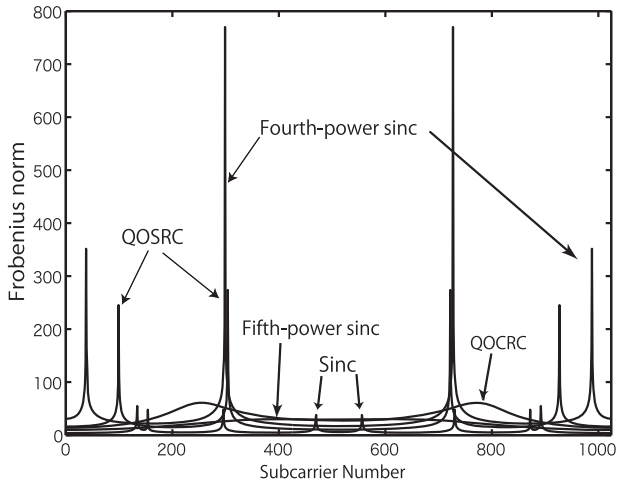

Figure 4.21: Frobenius norm of the whitening filter for different impulse responses (Number of subcarriers=1024, $G = 4$).

If the oversampling ratio increases, the interval of the samples, T_s/G, reduces in Eq. (4.15). Thus, Eq. (4.15) covers a larger spectrum. Both the number of dip points in the spectrum and the number of peak points in the Frobenius norm then increase. If the number of subcarriers increases, the resolution of the spectrum in Eq. (4.15) improves, the depth of the dip points in the spectrum becomes larger, and the peak value of the Frobenius norm grows.

4.2.4.5 Uncoded FS OFDM

Effect of Pulse Shaping Filter with 64 Subcarriers

In Figs. 4.22, 4.23 and 4.24, the BER curves with different pulse shaping filters for $G = \{1, 2, 4\}$ on the 16 path Rayleigh fading channel are presented. From Fig. 4.22, when $G = 1$, all of the BERs except the one with the sinc pulse filter are almost the same. The reason is that the bandwidth of the sinc pulse filter is smaller than those of other filters. Thus, the SNR of the subcarriers in the band edges are smaller and more bit errors are observed. When $G = 2$, the whitening matrix for the sinc pulse filter shows the large amount of the norm on the specific subcarriers in Fig. 4.19. These subcarriers generate more bit errors due to the correlated noise. As a result, the BER with the sinc pulse filter is larger than those with other filters. The norm of the whitening matrix with the QOSRC pulse filter is slightly larger than the rest of filters except the sinc pulse filter. Therefore,

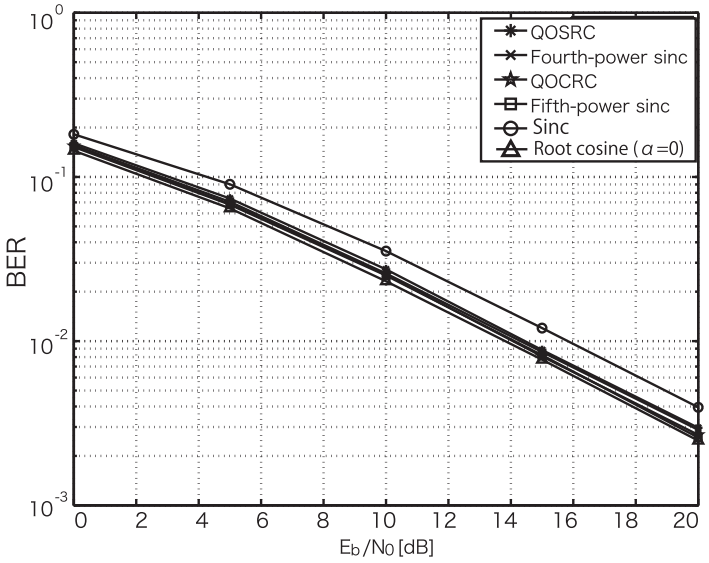

Figure 4.22: BER performance vs. E_b/N_0 on the 16 path Rayleigh fading channel with the uniform delay profile (QPSK, Number of subcarriers=64, $G = 1$).

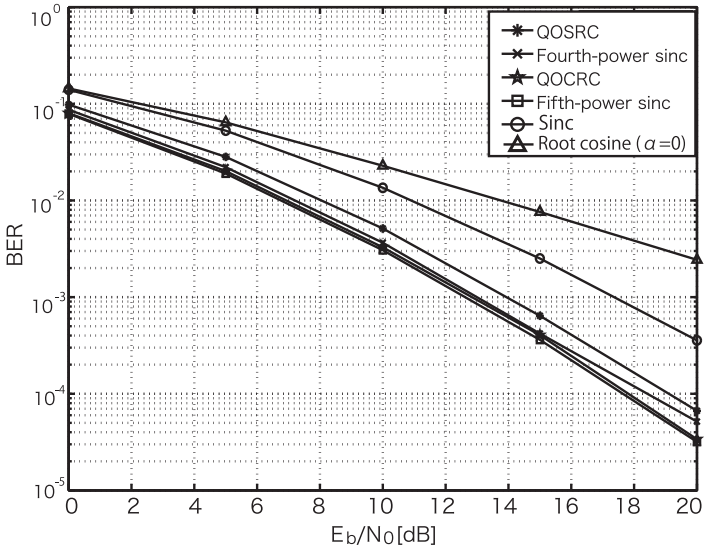

Figure 4.23: BER performance vs. E_b/N_0 on the 16 path Rayleigh fading channel with the uniform delay profile (QPSK, Number of subcarriers=64, $G = 2$).

the BER performance is also slightly worse.

When $G = 4$, BER performances of QOSRC pulse filter and the fourth-power sinc pulse filter are deteriorated. From Fig. 4.20, the norm with the QOSRC pulse

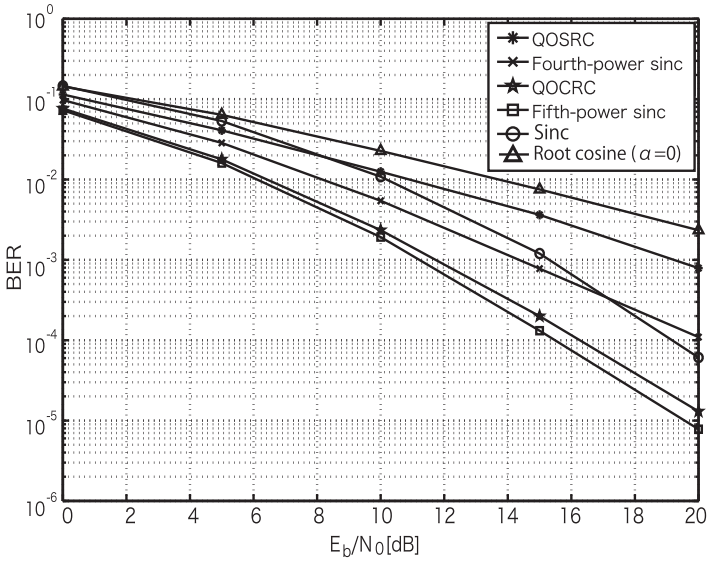

Figure 4.24: BER performance vs. E_b/N_0 on the 16 path Rayleigh fading channel with the uniform delay profile (QPSK, Number of subcarriers=64, $G = 4$).

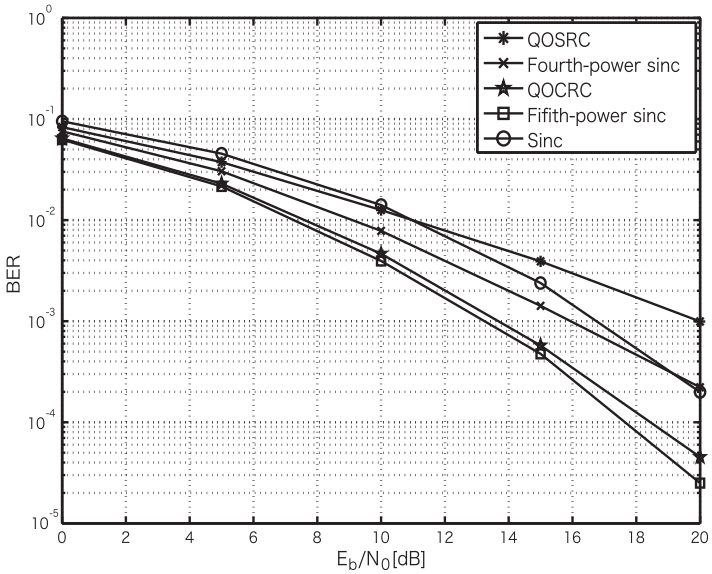

Figure 4.25: BER performance vs. E_b/N_0 on the 16 path Rayleigh fading channel with the uniform delay profile (16QAM, Number of subcarriers=64, $G = 4$).

filter shows the largest and the fourth-power sinc pulse filter shows the second largest on the specific subcarriers. On those subcarriers more bit errors are pro-

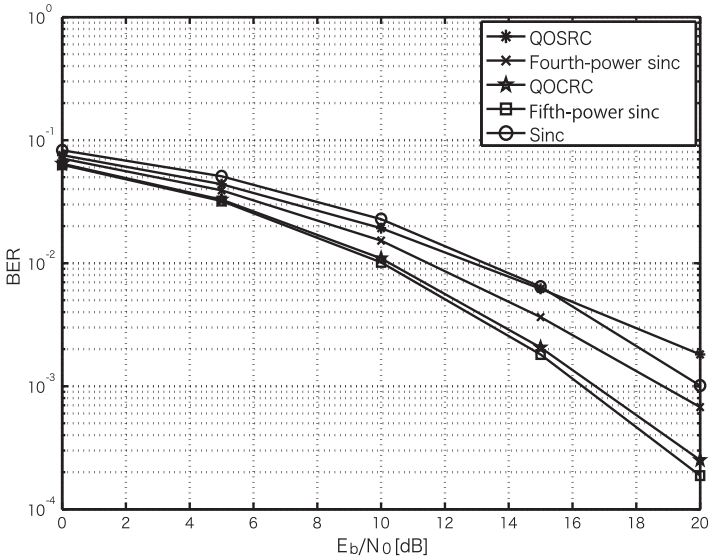

Figure 4.26: BER performance vs. E_b/N_0 on the 16 path Rayleigh fading channel with the uniform delay profile (64QAM, Number of subcarriers=64, $G = 4$).

duced. Even though E_b/N_0 increases, the BER does not reduce as those with the QOCRC pulse filter or the fifth-power sinc pulse filter. Therefore, the BER curves for those pulse filters in Fig. 4.24 are worse than those with the other filters except the sinc pulse filter. For the case of the sinc pulse filter, the bandwidth of the filter is smaller than the others as shown in Fig. 4.19. It is suggested in [4.6] that the excess bandwidth of the filter allows diversity gain in FS. The BER with the sinc pulse filter is then larger than those with the QOCRC pulse filter or fifth-power sinc pulse filter that has larger bandwidth.

Through Figs. 4.22-4.24, no diversity gain can be obtained with the root cosine roll-off filter. It has been suggested in [4.6] that the excessive bandwidth of the filter gives diversity gain with FS. Thus, the sharp frequency response of the root cosine filter limits diversity gain.

Figures 4.25 and 4.26 show the BER curves with different pulse shaping filters for $G = 4$ when 16QAM or 64QAM modulation is employed. In those figures, the same tendency on the BER performance can be observed as the case with QPSK modulation for $G = 4$. As far as we have investigated, when $G = \{1, 2\}$, the BER performance with 16QAM or 64QAM also shows the same tendency as the case with QPSK.

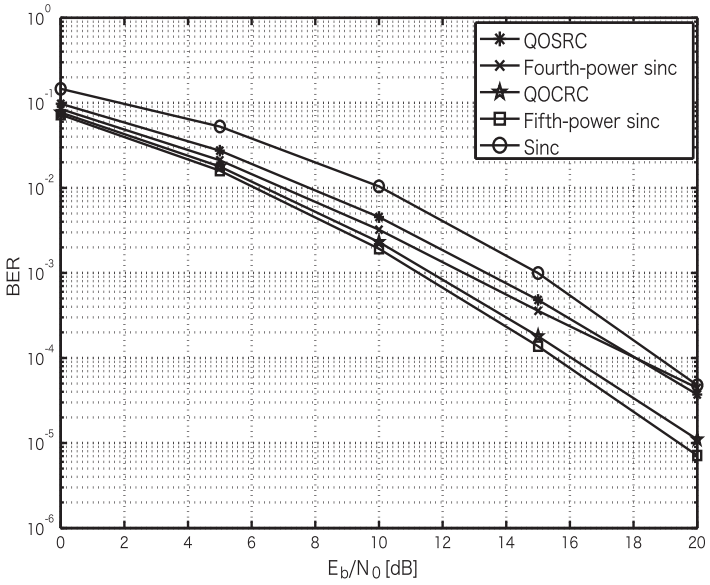

Figure 4.27: BER performance vs. E_b/N_0 on the 16 path Rayleigh fading channel with the uniform delay profile (QPSK, Number of subcarriers=1024, $G = 4$).

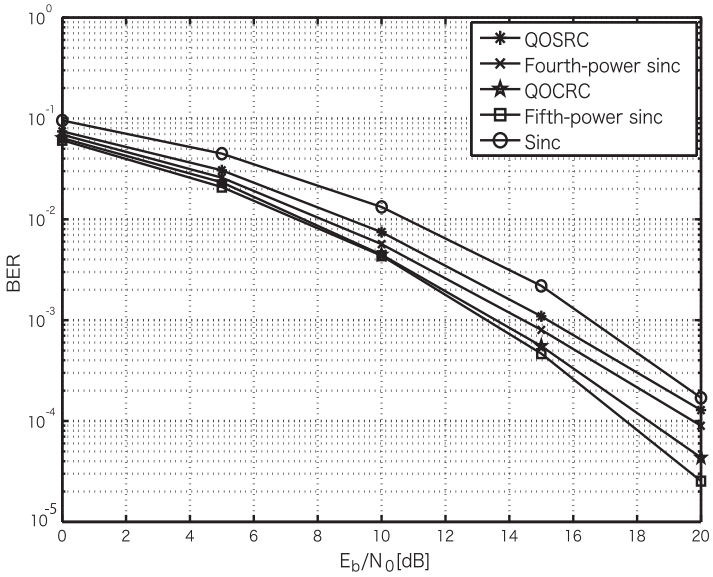

Figure 4.28: BER performance vs. E_b/N_0 on the 16 path Rayleigh fading channel with the uniform delay profile (16QAM, Number of subcarriers=1024, $G = 4$).

Effect of Pulse Shaping Filter with 1024 Subcarriers

The effect of the pulse shaping filters with larger numbers of subcarriers are also investigated. In Fig. 4.27, the BER curves with different pulse shaping filters for

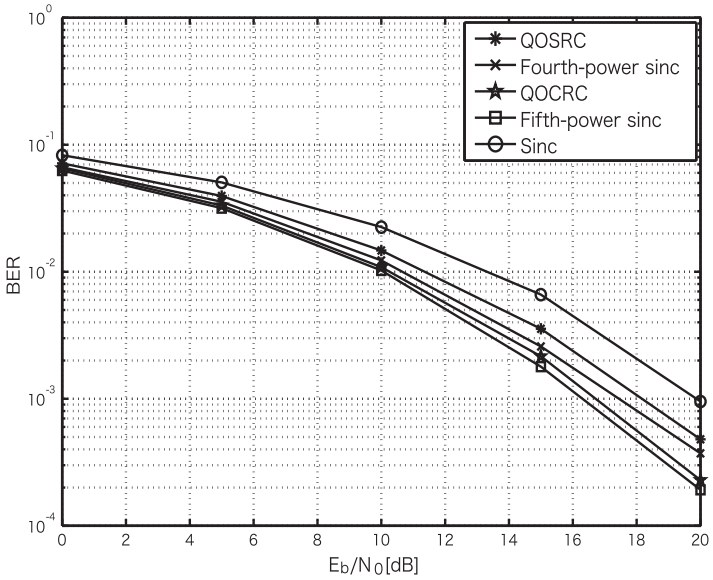

Figure 4.29: BER performance vs. E_b/N_0 on the 16 path Rayleigh fading channel with the uniform delay profile (64QAM, Number of subcarriers=1024, $G = 4$).

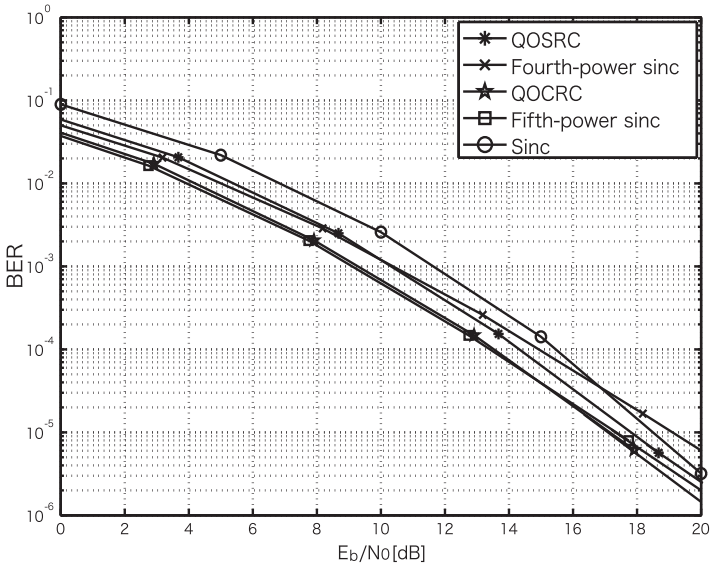

Figure 4.30: BER performance vs. E_b/N_0 on the 24 path Rayleigh fading channel with the exponential delay profile (QPSK, Number of subcarriers=1024, $G = 4$).

$G = 4$ are presented. The channel model we assume here is 16 path Rayleigh fading with a uniform delay profile. When $G = 4$, the curves of the Frobenius

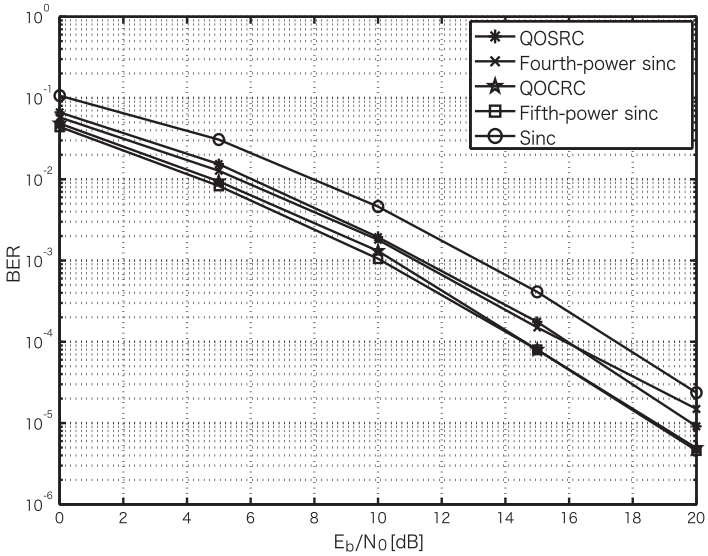

Figure 4.31: BER performance vs. E_b/N_0 on the GSM Typical Urban model (QPSK, Number of subcarriers=1024,$G = 4$).

norm of the whitening filters shown in Fig. 4.21 are different as compared to those in Fig. 4.20. In this case, the norm with the fourth-power sinc pulse filter shows the largest and the one with QOSRC pulse filter shows the second largest on the specific subcarriers. On those subcarriers more bit errors are produced. However, the BERs do not increase significantly in Fig. 4.27 as compared to those in Fig. 4.24. For the cases of the fourth-power sinc pulse filter and the QOSRC pulse filter, though the bit error rates on some particular subcarriers are larger, it is averaged over the BERs of the large number of subcarriers. On the other hand, the BER with the sinc filter is larger than those with other filters because of the smaller bandwidth and limited diversity gain. When $G = \{1, 2\}$, the same tendency on the BER performance can be observed as the cases with 64 subcarriers.

Figures 4.28 and 4.29 show the BER curves with different pulse shaping filters on the 16 path Rayleigh fading channel model when 16QAM or 64QAM modulation is applied. In those figures, the same tendency on the BER performance can be observed as the case with QPSK modulation for $G = 4$.

Figures 4.30 and 4.31 show the BER performance for QPSK modulation with different pulse shaping filters on the 24 path Rayleigh fading channel model and the GSM Typical Urban model. In those figures, the same as the case with the 16 path Rayleigh fading channel model, the BER degradation due to the different pulse shaping filters is smaller than that of the OFDM system with 64 subcarriers.

Since the number of multipath is smaller for the GSM model than the Rayleigh fading channel model, diversity gain through FS is smaller in Fig. 4.31. Thus, the BER curves for all the impulse responses of the filter are a little worse than those in Fig. 4.30.

4.2.4.6 Coded FS OFDM

Figure 4.32 shows the BER curves of the coded FS OFDM with different impulse responses of the pulse shaping filter. The number of subcarriers is 64 and the oversampling ratio is set to $G = 4$, here. A rate 1/2 convolutional code with its generating matrix $\mathbf{G} = [133_8, 171_8]$ and interleaving specified in the IEEE 802.11a standard are employed [4.15]. Soft decision Viterbi decoding is performed in the receiver. As compared to Fig. 4.24, the improvement of the BER curves for the QOSRC and fourth-power sinc pulse filters are limited. This is because the effect of the large Frobenius norm is spread over the subcarriers due to the channel coding and the interleaving. To reduce the effect of the large Frobenius norm, the metric in the Viterbi decoder is adjusted according to the Frobenius norm on each subcarrier. Figure 4.33 shows the BER curves of the coded FS OFDM with the adjusted metric. In this figure, the BER curves with the QOSRC and fourth-power sinc pulse filters are improved as compared to those in Fig. 4.32. The metric adjustment can mitigates the effect of the large Frobenius norm.

Figure 4.34 shows the BER curves of the coded FS OFDM with different impulse responses of the pulse shaping filter when the number of subcarriers is 1024. Figure 4.35 shows the BER curves of the coded FS OFDM with the adjusted metric according to the Frobenius norm. A rate 1/2 convolutional code with its generating matrix $\mathbf{G} = [133_8, 171_8]$ and interleaving specified in the IEEE 802.16 standard are employed [4.16]. In those figures, the same as the coded system, the BER is averaged over the large number of subcarriers and the difference due to the pulse shaping filters is smaller than that of the system with 64 subcarriers.

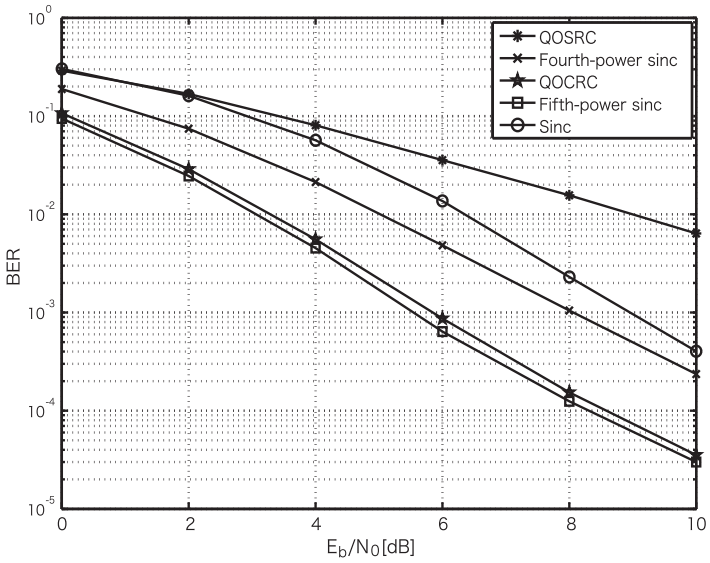

Figure 4.32: BER performance vs. E_b/N_0 of coded OFDM (QPSK, Number of subcarriers=64, $G = 4$).

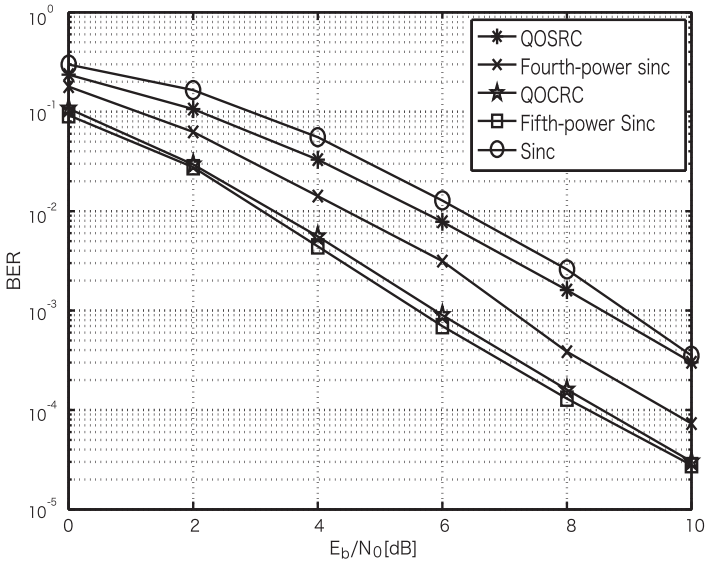

Figure 4.33: BER performance vs. E_b/N_0 of coded OFDM with Adjusted Metric (QPSK, Number of subcarriers=64, $G = 4$).

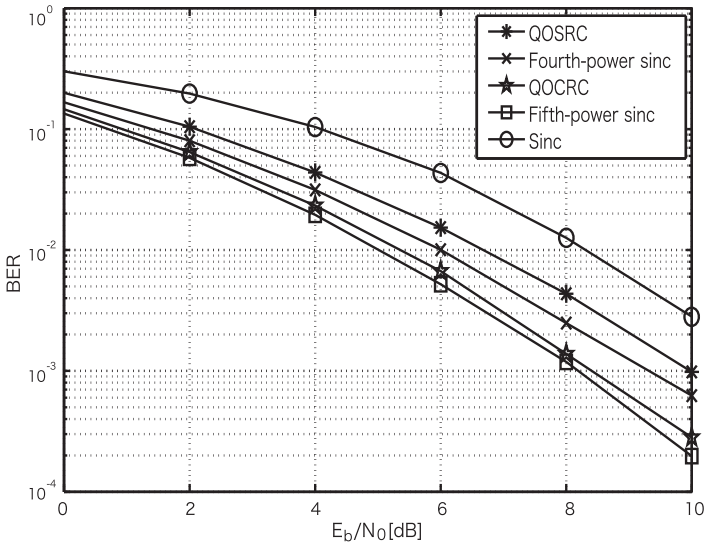

Figure 4.34: BER performance vs. E_b/N_0 of coded OFDM (QPSK, Number of subcarriers=1024, $G = 4$).

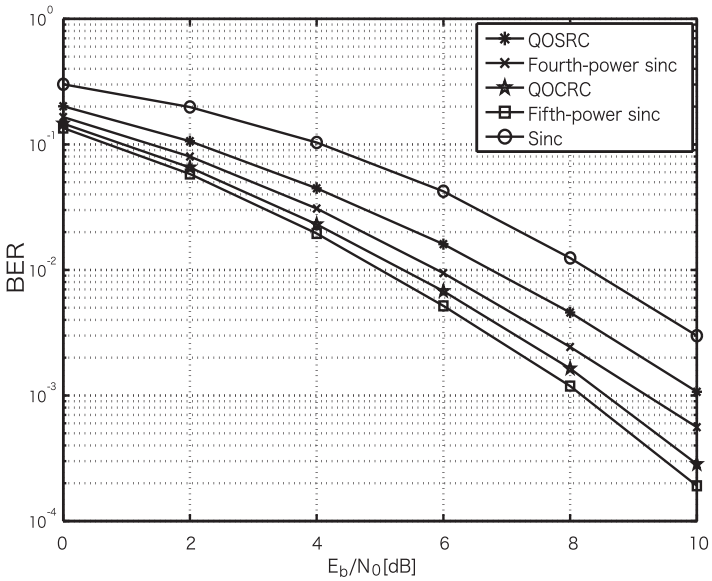

Figure 4.35: BER performance vs. E_b/N_0 of coded OFDM with Adjusted Metric (QPSK, Number of subcarriers=1024, $G = 4$).

4.2.5 Conclusions

In this section, the effect of the pulse shaping filters on the FS OFDM system with subcarrier-based MRC has been investigated. The Frobenius norm of the whitening filter closely corresponds to the frequency spectrum of the pulse shaping filter. It has been shown that the Frobenius norm of the whitening matrix has significant effect on the BER performance irrespective of modulation schemes and channel models. If the Frobenius norm is large, the power of the correlated noise components increases and the BER on the corresponding subcarrier is deteriorated. If the number of subcarriers is 64, the average BER also increases. When the number of subcarriers is 1024, the large amount of the Frobenius norm is concentrated on the specific subcarriers. Although the higher number of bit errors can be observed on those subcarriers, it is less significant to the average BER if the number of subcarriers is large.

When the channel coding is employed, the large Frobenius norm deteriorates the total BER performance of the system with 64 subcarriers. It has also been shown that the Viterbi decoder with the adjusted metric according to the Frobenius norm improves the BER performance.

As a conclusion, it is required to design the pulse shaping filters in order to reduce the amount of the correlated noise caused by the Frobenius norm and to obtain diversity gain. The Frobenius norm can be calculated at the stage of designing the pulse shaping filters. Moreover, when the number of subcarrier is small and the pulse shaping filter introduces the large amount of the Frobeinus norm on the specific subcarriers, the adjusted metric based on the Frobenius norm can mitigate the effect of the correlated noise components in the coded FS OFDM system.

4.3 Conclusions of Chapter 4

In Chapter 4, the correlated noise cancellation schemes in the FS OFDM system have been investigated. Despreading with the ASC cancels most of the correlated noise components in the FS OFCDM system. The performance of FS OFDM receiver can be improved by designing the parameters such as the bandwidth, the Frobenius norm of the whitening matrix corresponding to the impulse response of the pulse shaping filter, and the number of subcarriers. Moreover, the Viterbi decoder with the adjusted metric according to the Frobenius norm improves the BER performance of the coded FS OFDM system. It has been also shown that the effect of correlated noise can be reduced both in FS OFCDM and FS OFDM

systems.

4.4 References

[4.1] H. Atarashi and M. Sawahashi, "Investigation of Inter-Carrier Interference due to Doppler Spread in OFCDM Broadband Packet Wireless Access", IEICE Trans. on Commun., vol.E85-B, no.12, pp.2684-2693, Dec. 2002.

[4.2] H. Atarashi, S. Abeta, and M. Sawahashi, "Variable Spreading Factor-Othogonal Frequency and Code division Multiplexing (VSF-OFCDM) for Broadband Packet Wireless Access", IEICE Trans. on Commun., vol.E86-B, no.1, pp.291-299, Dec. 2003.

[4.3] Y. Kishiyama, N. Maeda, K. Higuchi, H. Atarashi, and M. Sawahashi, "Field Experiments on Throughput Performance above 100 Mbps in Forward Link for VSF-OFCDM Broadband Wireless Access", IEICE Trans. on Commun., vol.E88-B, no.2, pp.604-614, Feb. 2005.

[4.4] N. Maeda, H. Atarashi, S. Abeta, and M. Sawahashi, "Antenna Diversity Reception Appropriate for MMSE Combining in Frequency Domain for Forward Link OFCDM Packet Wireless Access", IEICE Trans. on Commun., vol.E85-B, no.10, pp.1966-1977, Oct. 2002.

[4.5] N. Miki, H. Atarashi, and M. Sawahashi, "Effect of Time Diversity in Hybrid ARQ Considering Space and Path Diversity for VSF-OFCDM Downlink Broadband Wireless Access", Proc. of the 15th IEEE Symposium on Personal Indoor and Mobile Radio Communications 2004, pp.604-608 vol.1, Sep. 2004.

[4.6] C. Tepedelenlioglu and R. Challagulla, "Low-Complexity Multipath Diversity Through Fractional Sampling in OFDM," IEEE Trans., on Signal Processing, vol.52, no.11, pp.3104- 3116, Nov. 2004.

[4.7] Y. Kato, M. Inamori, and Y. Sanada, "Multipath Diversity through Fractional Sampling in MB-OFDM," Proc. of the 5th IEEE VTS Asia Pacific Wireless Communications Symposium, Aug. 2008.

[4.8] K. Suto and T. Otsuki, "Space-Time-Frequency Block Codes over Frequency Selective Fading Channels," IEICE Trans. on Commun., vol.E86-B, no.7, pp.1939-1945, July 2004.

[4.9] M. Inamori, H. Nishimura, Y. Sanada, and M. Ghavami, "Fractional Sampling OFCDM with Alternative Spreading Code," Proc. of the 11th IEEE International Conference on Communications Systems, pp.1394-1398, Nov. 2008.

[4.10] G. Golub and C. V. Loan, "Matrix Computations," 3rd Edition, Johns Hopkins University Press, 1996.

[4.11] S. L. Loyka, "Channel Capacity of MIMO Architecture using the Exponential Correlation Matrix," IEEE Communications Letters, vol.5, no.9, pp.369-371, Sept. 2001.

[4.12] M. Chiani, M. Z. Win, and A. Zanella, "On the Capacity of Spatially Correlated MIMO Rayleigh-fading Channels," IEEE Trans. on Information Theory, vol.49, no.10, pp.2363-2371, Oct. 2003.

[4.13] K. Zhang, Y. L. Guan, and B. C. Ng, "Full-Rate Orthogonal Space Time Block Code With Pulse-Shaped Offset QAM for Four Transmit Antennas," IEEE Trans. on Wireless Communications, vol.6, no.4, pp.1551-1559, April 2007.

[4.14] I. Sasase, R. Nagayama, and S. Mori, "Bandwidth Efficient Quadrature Overlapped Squared Raised-Cosine Modulation," IEEE Trans. on Wireless Communications, vol.33, pp.101-103, Jan. 1985.

[4.15] Part 11: Wireless LAN Medium Access Control (MAC) and Physical Layer (PHY) Specifications; Highspeed Physical Layer in the 5GHz Band, 1999, IEEE.802.11a.

[4.16] Part 16: Air Interface for Fixed Broadband Wireless Access Systems, 2004, IEEE Std. 802.16.

Chapter 5

Overall Conclusions

OFDM system has been employed in many wireless standards to achieve high data rate transmission. In OFDM receivers, the received signal suffers from distortions due to RF components, timing jitter, or baseband filters. To implement a low cost and low power consumption receiver, the compensation of the signal distortion in a digital domain is necessary. In this dissertation, the digital compensation schemes for the signal distortion in OFDM receivers were investigated.

5.1 Signal Compensation Schemes in OFDM Direct Conversion Receivers

Digital compensation schemes for the signal distortion due to RF components in direct conversion receiver are presented in Chapter 2. The OFDM direct conversion receivers suffer from the frequency and DC offsets. In Section 2.1, the frequency offset estimation in the presence of time-varying DC offset for OFDM direct conversion receivers has been presented. The frequency offset is estimated based on the preamble symbols in the IEEE 802.11a burst structure. In the proposed scheme, the differential filter is employed to remove the dynamic DC offset. It has been shown that the residual DC offset is eliminated with the differential filter by setting the optimum threshold level. The frequency offset can be then estimated accurately with simple calculation. The proposed compensation scheme has offered the superior frequency offset estimation as compared with the conventional scheme with high pass filter.

The OFDM direct conversion receiver also suffers from the IQ imbalance as well. The IQ imbalance deteriorates the performance of the frequency offset estimation scheme with the differential filter. In Section 2.2, the frequency offset estimation

with the differential filter in the presence of IQ imbalance has been analyzed. The numerical results obtained through computer simulation have shown that the derived analysis provides close approximation to the performance of the frequency offset estimation scheme. It has also clarified the dependency of the MSE on the waveform of the preamble symbols, which is caused by the IQ imbalance.

In Section 2.3, the IQ imbalance estimation in the presence of the frequency and DC offsets for the OFDM direct conversion receiver has been discussed. The same differential filter has been employed to remove the time-varying DC offset as in Section 2.1 and Section 2.2. The IQ imbalance is estimated using a simple equation without the impulse response of the channel. The numerical results obtained through computer simulations has shown that the BER performance using the proposed IQ imbalance estimation scheme is satisfactory when E_b/N_0 is higher than 20[dB], in which 64QAM is used for the 1st modulation. However, the accuracy of the IQ imbalance estimation with the proposed scheme is deteriorated when the frequency offset is small. To overcome this problem, the new IQ imbalance estimation scheme in frequency domain is proposed in Section 2.4. The IQ imbalance is estimated with pilot subcarriers in data period. Numerical results obtained through computer simulation show that the estimation accuracy and the BER performance can be improved even if the frequency offset is small. Thus, the combination of two low-complexity IQ imbalance estimation schemes is suitable for low-cost and low-power-comsumption direct conversion receivers.

In Chapter 2, it is shown that the frequency offset and IQ imbalance are estimated well by the simple calculation with the differential filter. These signal compensation schemes enable the low-cost and low-power-comsumption direct conversion receivers.

5.2 Signal Compensation Schemes in RF-sampling Receivers

In contrast to the front end of the direct conversion receiver, the RF-sampling receiver is greatly simplified with digital RF processing. However, the RF-sampling receiver suffers from the timing jitter generated from the phase noise in PLL. In Chapter 3, the effect of timing jitter on quadrature charge sampling has been discussed. The distributions of timing jitter based on the structure of two major noise sources, which are VCO and TCXO in the PLL. The SINR of the downconverted signal has been evaluated with different data rates and modulation schemes. It has been shown that timing jitter deteriorates the SINR of the demodulated signal due to the crosstalk between the I-phase and Q-phase components of the received

signal. The BER performances with both single carrier QAM and OFDM modulation schemes has shown the error floor with higher data rates. Therefore, in the wideband system, the timing jitter in quadrature charge sampling may limit the performance of the receiver.

5.3 Signal Compensation Schemes in FS OFDM Receivers

One of the important factors of the receiver architecture is the better BER performance. The OFDM receiver can improve the performance with diversity. The antenna diversity has been receiving large attention, which is standardized in the physical layer of IEEE 802.11n. However, it is hard to implement multiple antennas in small devices. As the diversity scheme with a single antenna, FS OFDM system has been investigated. However, as the number of subcarriers and the oversampling ratio increase, the correlation among the noise components over different subcarriers deteriorates the BER performance. Chapter 4 discusses the correlated noise cancelation schemes in FS OFDM receivers. In Section 4.1, the correlated noise cancellation scheme in FS OFCDM system has been discussed. To reduce the correlated noise, ASC, which has positive and negative components alternatively, is used in the FS OFCDM system. Despreading with the ASC cancels most of the correlated noise components. Numerical results obtained through computer simulation show that the proposed scheme can improve the performance of the receiver with the large oversampling ratio and the number of subcarriers.

In Section 4.2, the effect of the correlation among the noise components in the FS OFDM system has been investigated. The impulse response of the filter determines the correlation among the noise components because the noise passes through the pulse shaping filter in the receiver. To evaluate the effect of correlation among the noise components, five pulse shaping filters are applied to both the FS OFDM and coded FS OFDM systems. Numerical results obtained through computer simulations has shown that the Frobenius norm of a whitening matrix corresponding to the pulse shaping filter has significant effect on the BER performance especially with a small numbers of subcarriers. It has also been shown that the Viterbi decoder with the adjusted metric according to the Frobenius norm improves the BER performance of the coded FS OFDM system. The BER performance depends on two facts, which are diversity gain and the Frobenius norm. The Frobenius norm can be calculated at the stage of designing the pulse shaping filters. The high-performance FS OFDM receiver can be realized by designing the parameters such as the bandwidth, the Frobenius norm of the whitening matrix

corresponding to the impulse response of the pulse shaping filter, and the number of subcarriers.

Acknowledgements

This dissertation has been a long journey. I have endured and completed this journey with the help and support from numerous people around me.

This dissertation would not have been possible if not for the stimulating suggestions and encouragement given to me by my supervisor Prof. Yukitoshi Sanada. I am indebted to his diligence and patience in constantly guiding me towards the completion of this dissertation and beyond. If not for his careful supervision, this dissertation could not boast the number of contributions it has achieved.

Furthermore, I would also like to express my gratitude for the referees who examined this dissertation, Prof. Sasase, Prof. Nakagawa, Prof. Ishikuro and Prof. Ghavami. Their critical review and constructive suggestions added an extra layer of polish to this dissertation.

I would like to thank my co-researchers Mr. M. Abe, Mr. K. Saijo, Mr. H. Yokoshima and Mr. Y. Kondo from Sony Corporation for their suggestions and discussions. Our joint research started when I was just a bachelor course student and it has been a great experience to have worked with them for so many years.

As a member of Sanada Laboratory, I would also like to take advantage of this opportunity to express my thanks towards my other colleagues for their support and encouragement. Particularly, I would like to thank my doctoral colleague, Caglar, for his encouragements in overcoming the challenges associated with the degree. I was able to enjoy my doctorate studies because of the warmth and family-like atmosphere in the lab. I would also like to express my appreciation my fellow Research Assistants (RAs) in the GCOE program, Mr. K. Adachi, Maduranga, Mr. S. Iwamura, Mr. K. Kyochi, Alex, Parn and Safda, for the stimulating research discussions that helped give my research some perspective.

However, life is not all work and no play. There are other external elements that have supported me as well throughout this journey. I would like to thank Ken for taking time out to proofread certain parts of this dissertation. I would also like to thank my good friend Mari for her support.

Last but not least, I wish to express my heartfelt thanks to my family who have

always been a great source of support and and encouragement for me.

List of Achievements

Journal Publications

1. M. Inamori, A. M. Bostamam, and Y. Sanada, "Influence of Timing Jitter on Quadorature Charge Sampling," IET Communications, Vol.1, No.4, pp.705-710, Aug. 2007.

2. M. Inamori, A. M. Bostamam, Y. Sanada, and H. Minami, "Frequency Offset Estimation Scheme in the Presence of Time-varying DC Offset for OFDM Direct Conversion Receivers," IEICE Trans. on Communications, Vol.E90-B, No.10, pp.2884-2890, Oct. 2007.

3. M. Inamori, T. Kawai, T. Kobayashi, H. Nishimura, and Y. Sanada, "Effect of Pulse Shaping Filters on a Fractional Sampling OFDM System with Subcarrier-Based Maximal Ratio Combining," IEICE Trans. on Communication, vol.E92-B, no.5, pp.1484-1494, May 2009.

4. M. Inamori, A. M. Bostamam, Y. Sanada, and H. Minami, "IQ Imbalance Compensation Scheme in the Presence of Frequency Offset and Dynamic DC Offset for a Direct Conversion Receiver," IEEE Trans. on Wireless Communications, Vol.8, no.5, pp.2214-2220, May 2009.

5. M. Inamori, S. Takayama, and Y. Sanada, "IQ Imbalance Estimation Scheme in the Presence of DC Offset and Frequency Offset in the Frequency Domain," accepted to IEICE Trans. on Fundamentals.

Other Journal Publications

1. Y. Suzuki, A. M. Bostamam, M. Inamori, and Y. Sanada, "Direct-Sequence / Spread-Spectrum Communication System with Sampling Rate Selection Diversity," IEICE Trans. on Communications, Vol.E91-B, No.1, pp.267-273, Jan. 2008.

2. H. Nishimura, M. Inamori, and Y. Sanada, "Sampling Rate Selection for Fractional Sampling in OFDM," IEICE Trans. on Communications, Vol.E91-B, No.9, pp.2876-2882, Sept. 2008.

Conference Publications

1. M. Inamori, A. M. Bostamam, and Y. Sanada, "Influence of Sampling Jitter on Discrete Time Receiver," in Proc. the 16th Annual International Symposium on Personal Indoor and Mobile Radio Communications, Berlin, Germany, Sept. 2005.

2. M. Inamori, A. M. Bostamam, Y. Sanada, and H. Minami, "Frequency Offset Compensation Scheme under DC Offset for OFDM Direct Conversion Receivers," in Proc. the 9th International Symposium on Wireless Personal Multimedia Communications, pp.378-382, San Diego, USA, Sept. 2006.

3. M. Inamori, A. M. Bostamam, Y. Sanada, and H. Minami,"Frequency Offset Estimation Scheme in the Presence of Time-varying DC Offset and IQ Imbalances for OFDM Direct Direct Conversion Receivers," in Proc. the 18th Annual International Symposium on Personal Indoor and Mobile Radio Communications, Athens, Greece, Sept. 2007.

4. M. Inamori, H. Nishimura, Y. Sanada, and M. Ghavami, "Fractional Sampling OFCDM with Alternative Spreading Code," in Proc. the 11th IEEE International Conference on Communications Systems, Guangzhou, China, Nov. 2008.

5. M. Inamori, T. Kawai, T. Kobayashi, H. Nishimura, and Y. Sanada, "Effect of Frobenius Norm of Whitening Matrix on Fractional Sampling OFDM with Subcarrier-Based Maximal Ratio Combining," in Proc. the 2009 RISP International Workshop on Nonlinear Circuits and Signal Processing, Hawaii, U.S.A., March 2009.

6. M. Inamori, A. M. Bostamam, Y. Sanada, and H. Minami, "IQ Imbalance Compensation Scheme in the Presence of Frequency Offset and Dynamic DC Offset for a Direct Conversion Receiver," in Proc. the 69th IEEE Vehicular Technology Conference, Barcelona, Spain, April 2009.

7. M. Inamori, T. Kawai, T. Kobayashi, H. Nishimura, and Y. Sanada, "Metric Weighting Scheme on a Coded Fractional Sampling OFDM System," in Proc.

the the 70th IEEE Vehicular Technology Conference, Anchorage, U.S.A., Sept. 2009. [accepted]

8. M. Inamori, A. M. Bostamam, and Y. Sanada, "Performance of Frequency Offset Estimation in the Presence of IQ Imbalance for OFDM Direct Conversion Receivers," in Proc. 2009 IEEE Pacific Rim Conference on Communications, Computers and Signal Processing, Victoria, Canada, Aug. 2009. [accepted]

9. M. Inamori and Y. Sanada, "Effect of Pulse Shaping Filter on MB-OFDM with Fractional Sampling," in Proc. the 12th International Symposium on Wireless Personal Multimedia Communications, Sendai, Sept. 2009. [accepted]

10. M. Inamori, S. Takayama, and Y. Sanada, "Frequency Domain IQ Imbalance Estimation in the Presence of DC Offset and Frequency Offset," in Proc. the 20th IEEE International Symposium On Personal, Indoor and Mobile Radio Communications, Tokyo, Sept. 2009. [accepted]

Other Conference Publications

1. Y. Suzuki, A. M. Bostamam, M. Inamori, and Y. Sanada, "Sampling Rate Selection Diversity for Direct-Sequence Spread Spectrum," in Proc. SDR Technical Conference 2006, Orlando, USA, Nov. 2006.

2. H. Nishimura, M. Inamori, and Y. Sanada, "Sampling Rate Selection for Fractional Sampling in OFDM," in Proc. the 18th Annual International Symposium on Personal Indoor and Mobile Radio Communications, Athens, Sept. 2007.

3. Y. Kato, M. Inamori, and Y. Sanada, "Multipath Diversity Through Fractional Sampling in MB-OFDM," in Proc. the 5th IEEE VTS Asia Pacific Wireless Communications Symposium, Sendai, Japan, Aug. 2008.

4. Y. Suzuki, A. M. Bostamam, M. Inamori, and Y. Sanada, "Sampling Rate Selection Path Diversity for a RAKE Receiver in DS/SS," in Proc. the 68th IEEE Vehicular Technology Conference, Calgary, Canada, Sept. 2008.

5. H. Nishimura, M. Inamori, and Y. Sanada, "Initial Sampling Point Selection in OFDM Receiver with Fractional Sampling," in Proc. International Workshop on Vision, Communications and Circuits, Xi'an, China, Nov. 2008.

6. T. Shinkai, H. Nishimura, M. Inamori, and Y. Sanada, "Experimental Investigation of Fractional Sampling in IEEE802.11a WLAN System," in Proc. the 11th IEEE International Conference on Communications Systems, Guangzhou, China, Nov. 2008.

7. H. Nishimura, M. Inamori, Y. Sanada, and M. Ghavami, "Non-uniform Sampling Point Selection in OFDM Receiver with Fractional Sampling," in Proc. 2009 IEEE Pacific Rim Conference on Communications, Computers and Signal Processing, Victroia, Aug. 2009. [accepted]

8. A. Suzuki, M. Inamori, and Y. Sanada, "Symbol Weighting Scheme in OFDM Receiver with Sigma-Delta A/D Converter," in Proc. the 12th International Symposium on Wireless Personal Multimedia Communications, Sendai, Sept. 2009. [accepted]

Technical Reports

1. M. Inamori, A. M. Bostamam, Y. Sanada, "Influence of Sampling Jitter on the Discrete Time Receiver, " Technical Reports of IEICE, SR2004-21, March 2005.

2. M. Inamori. M. Bostamam, Y. Sanada, "Influence of Sampling Jitter on the Discrete Time Receiver, " IEICE General Conference, B-17-2, March 2005.

3. M. Inamori, A. M. Bostamam, Y. Sanada, H. Minami, "Frequency Offset Estimation Scheme in the presence of Time-varying DC offset for OFDM Direct Conversion Receivers , " Technical Reports of IEICE, SR2006-50, Nov. 2006.

4. M. Inamori, A. M. Bostamam, Y. Sanada, H. Minami, "Frequency Offset Estimation Scheme in the Presence of Time-varying DC Offset and IQ Imbalance for OFDM Direct Conversion Receivers, " Technical Reports of IEICE,SR2007-15, May 2007.

5. M. Inamori, Y. Sanada, "Study of Pulse Shaping Filter on MB-OFDM with Fractional Sampling," Technical Reports of IEICE,WBS2007-42, Oct. 2007.

6. M. Inamori, A. M. Bostamam, Y. Sanada, H. Minami, "IQ Imbalance Estimation Scheme in the Presence of DC Offset and Frequency Offset for OFDM Direct Conversion Receivers," Technical Reports of IEICE, SR2007-54, Nov. 2007.

7. M. Inamori, A. M. Bostamam, Y. Sanada, H. Minami, "IQ Imbalance Estimation Scheme in the Presence of Time-varying DC offset and Frequency Offset for OFDM Direct Conversion Receivers," Technical Reports of IEICE, SR2007-78, Jan. 2008.

8. M. Inamori, H. Nishimura, Y. Sanada, "Alternative Spreading Code for Fractional Sampling OFCDM, " Technical Reports of IEICE, SR2008-12, May 2008.

9. M. Inamori, T. Kawai, T. Kobayashi, H. Nishimura, Y. Sanada, "Effect of pulse shaping filters on fractional sampling OFDM systems with subcarrier-based maximal ratio combining," Technical Reports of IEICE, SR2008-42, Oct. 2008.

10. M. Inamori, Y. Sanada, "Performance Analysis of Frequency Offset Estimation in the Presence of DC Offset and IQ Imbalance for OFDM Direct Conversion Receivers," Technical Reports of IEICE, SR2008-90, March 2009.

11. M. Inamori, K. Takashi, T. Kobayashi, H. Nishimura, Y. Sanada, "Metric Weighting Scheme on a Fractional Sampling Coded OFDM System with Subcarrier-Based Maximal Ratio Combining," IEICE General Conference, B-17-22, March 2009.

12. M. Inamori, S. Takayama, Y. Sanada, "Frequency Domain IQ Imbalance Estimation Scheme in the Presence of DC Offset and Frequency Offset," Technical Reports of IEICE, SR2009-05, May 2009.

13. M. Inamori, S. Takayama, Y. Sanada, "Frequency Domain IQ Imbalance Estimation Scheme in the Presence of DC Offset and Frequency Offset," IEICE Society Conference, ABS-1-8, Sept. 2009.

Other Technical Reports

1. Y. Suzuki, A. M. Bostamam, M. Inamori, Y. Sanada, "DS/SS Communication System with Sampling Rate Selection Diversity," Technical Reports of IEICE, SR2006-51, Nov. 2006.

2. H. Nishimura, M. Inamori, Y. Sanada, "Sampling Rate Selection for Fractional Sampling in OFDM," Technical Reports of IEICE, SR2007-1, May 2007.

3. H. Nishimura, M. Inamori, Y. Sanada, "Sampling Rate Selection for Fractional Sampling in OFDM," Japan Society for Simulation Technology Conference, 11-1, June 2007.

4. H. Nishimura, M. Inamori, Y. Sanada, "Sampling Point Selection in OFDM Receiver with Fractional Sampling," Technical Reports of IEICE, SR2007-87, March 2008.

5. Y. Suzuki, A. M. Bostamam, M. Inamori, Y. Sanada, "Sampling Rate Selection for a RAKE Receiver in DS/SS," Technical Reports of IEICE, SR2007-88, March 2008.

6. Y. Suzuki, A. M. Bostamam, M. Inamori, Y. Sanada, "Sampling Rate Selection for a RAKE Receiver in DS/SS," IEICE General Conference, BS-1-9, March 2008.

7. H. Nishimura, M. Inamori, Y. Sanada, "Sampling Point Selection in OFDM Receiver with Fractional Sampling," IEICE General Conference, BS-1-10, March 2008.

8. T. Shinkai, H. Nishimura, M. Inamori, Y. Sanada, "Experimental Investigation of Fractional Sampling in IEEE802.11a WLAN System, " Technical Reports of IEICE, SR2008-28, July 2008.

9. H. Nishimura, M. Inamori, Y. Sanada, M.Ghavami, "Non-uniform Sampling Point Selection in OFDM Receiver with Fractional Sampling," Technical Reports of IEICE, SR2008-41, Oct. 2008.

10. H. Nishimura, M. Inamori, Y. Sanada, "Complexity Reduction Scheme for Sampling Point Selection in Fractional Sampling OFDM Receiver," IEICE General Conference, B-17-23, March 2009.

11. A. Suzuki, M. Inamori, Y. Sanada, "Symbol Weighting Scheme in OFDM Receiver with Sigma-Delta A/D Converter," Technical Reports of IEICE, WBS2009-2, June 2009.

12. R. C. Kizilirmak, M. Inamori, and Y. Sanada, "Spatial Fading Correlation for OFDM Antenna Arrays on a per Subcarrier Basis," IEICE Society Conference, ABS-1-8, Sept. 2009.

Awards

1. NCSP 2009 Student Paper Award, March 2009.

2. IEEE VTS Japan 2009 Student Paper Award, April 2009.